5-2001

Bubble growth behavior in supersaturated liquid solutions

David Robert Cyr

BUBBLE GROWTH BEHAVIOR IN SUPERSATURATED LIQUID SOLUTIONS

By

David Robert Cyr

B.S. University of Maine, 1993

M.S. University of Maine, 1998

A THESIS

Submitted in Partial Fulfillment of the

Requirements for the Degree of

Doctor of Philosophy

(in Chemical Engineering)

The Graduate School

The University of Maine

May, 2001

Advisory Committee:

Edward V. Thompson, Professor of Chemical Engineering, Advisor

Francois G. Amar, Professor of Chemistry

Douglas W. Bousfield, Professor of Chemical Engineering

Hemant P. Pendse, Professor of Chemical Engineering

William N. Unertl, Professor of Physics

BUBBLE GROWTH BEHAVIOR IN SUPERSATURATED LIQUID SOLUTIONS

By David Robert Cyr

Thesis Advisor: Dr. Edward V. Thompson

An Abstract of the Thesis Presented
in Partial Fulfillment of the Requirements for the
Degree of Doctor of Philosophy
(in Chemical Engineering)
May, 2001

The growth characteristics of gas bubbles in supersaturated liquid solutions were measured in preliminary experiments involving glass bottles followed by more controlled and systematic investigations using a custom designed experimental apparatus. It was proven that the presence of pre-existing gas was responsible for the bubble formation observed. Bubble growth occurred in very regular cyclical patterns at specific locations containing trapped gases.

In the custom designed apparatus, liquids could be saturated with gases and supersaturated solutions made by depressurizing the system. Artificial capillaries, pre-seeded with air bubbles, behaved in a similar manner to naturally occurring sites containing pre-existing gases.

The apparent gap in time between the detachment of one bubble and the first observable appearance of the next bubble, denoted by earlier researchers as a "nucleation" lapse time, was identified as a misnomer. Further analysis focused on measuring bubble growth times, or the time between consecutive detachments.

The long term behavior of a series of air bubbles in supersaturated water, growing from artificial capillaries positioned inside the apparatus, revealed that bubble detachment diameter changes very little from bubble to bubble, but that the bubble growth times tend to increase as the dissolved gas concentration decreases. In further experiments, the bubble growth characteristics of the first full bubble only were analyzed. Air in water experiments involving three capillary sizes, an altered saturation routine, and a partial depressurization were conducted along with experiments using carbon dioxide in water and helium in water.

Neither the bubble growth model proposed by Manley (1960), which assumed a diffusion-only type solution, nor the theory of Scriven (1959), which accounted for both diffusion and convection, accurately predicts the bubble growth times observed, particularly at higher supersaturation ratios (> 25). Manley predictions are as much as 1500% too high while Scriven predictions are as much as 400% too high at the higher supersaturation ratios. A new model, based on the Scriven theory, reformulates the bubble surface velocity term and includes an additional restriction on one of the boundary conditions. Bubble growth time predictions from the new model at the higher supersaturations were always within 25% of the experimentally measured value.

Acknowledgements

I would like to express my gratitude to Professor Edward V. Thompson for his guidance as committee chair. I would also like to acknowledge the assistance of my committee members, Dr. Francois G. Amar, Dr. Douglas W. Bousfield, Dr. Hemant P. Pendse, and Dr. William N. Unertl. The committee was especially helpful in identifying the need for a new bubble growth model. Special thanks are extended to Dan Jolicoeur, Keith Hodgins, and Adam Violette of the University of Maine Chemical Engineering Department Staff for their help in designing, constructing, and maintaining the experimental apparatus. Thank you to all the graduate students for their friendship and support.

I would like to recognize the industrial sponsors of the Cooperative Recycled Fibers Studies Program (Beloit Corporation, Champion International Corporation, Fraser Papers Incorporated, Shell Development Company, Sunds Defibrator AB, Thermo Black Clawson Incorporated, Weyerhaeuser Paper Company, and Xerox Corporation), which provided the majority of the financial support for this work. I would also like to express my appreciation to the University of Maine Pulp and Paper Foundation in addition to the Department of Chemical Engineering at the University of Maine for their additional financial support.

Table of Contents

List of Tables

List of Figures

1. Background

1.1 Introduction

A supersaturated liquid solution is defined as a solution that contains a higher amount of dissolved gas than a solution in equilibrium at the same conditions of pressure and temperature. Supersaturated solutions can be created during chemical reactions [Rubin and Noyes (1987)], but the most common technique involves dissolving a gas into the liquid at high pressure and then suddenly reducing the pressure. The fact that all supersaturated solutions do not instantaneously produce bubbles has been attributed to the fact that there are two types of supersaturated solutions: metastable and unstable [Zettlemoyer (1969)]. Metastable supersaturated solutions remain unchanged for a very long period of time while unstable supersaturated solutions undergo phase changes immediately.

The fundamental events for gas bubbles in supersaturated solutions are identified by Lubetkin (1995). They are: formation, growth, detachment, rise, and bursting. The most critical events are the formation and growth stages. Without the formation and subsequent growth of bubbles in supersaturated liquid solutions, the later stages cannot occur.

The formation and growth of gas bubbles in supersaturated liquid solutions is important in both industrial processes and everyday situations. Supersaturation ratios less than 100 are most commonly encountered. The supersaturation ratio is defined as the ratio of the actual amount of dissolved gas in solution compared to the amount of dissolved gas predicted by equilibrium at the same conditions of temperature and pressure. When clarifying dissolved air flotation waste streams or decontaminating

radioactive liquids through repeated depressurizations, it is desirable that many bubbles form and grow. Unstable supersaturated solutions are favored for these cases. However, when deep sea diving, applying coatings or paints, or enjoying a carbonated beverage, it is not desirable that bubbles form and continue to grow. Metastable supersaturated solutions are preferred for these examples.

1.2 Objective

The objective of this dissertation was to identify the mechanism(s) by which bubble formation in supersaturated liquid solutions occurred and to further investigate the subsequent bubble growth characteristics. First, naturally occurring bubble producing sites from the walls of clear glass soda bottles were analyzed. A custom made experimental apparatus was then designed and constructed so that more controlled and systematic experiments could be performed. Artificial bubble producing sites, similar to the naturally occurring ones identified in the soda bottle experiments, were fabricated from capillaries for use in the experimental apparatus. Air in water experiments involving three capillary sizes, an altered saturation routine, and a partial depressurization were conducted along with experiments of carbon dioxide in water and helium in water. Finally, experimentally measured bubble growth times were compared to two previous theoretical predictions and a new model presented as part of this dissertation.

2. Literature Review

Numerous researchers have studied the formation and growth of bubbles from gas-supersaturated liquid solutions since the days of Leonardo da Vinci's investigations in the 16th century [Liger-Belair *et al.* (2000)]. In the last century, two theories on the formation of bubbles from supersaturated liquid solutions have come to the forefront. Early work that led to the development of the two theories will first be presented in **92.1.** Works related to the Classical Nucleation Theory (CNT), which assumes that bubbles form from an initial bubble size of zero, will be presented in $2.2 followed by research that assumes that bubbles form from Harvey Nuclei, or locations containing some pre-existing gas trapped on a surface in contact with the supersaturated liquid solution, in $2.3. Some confusion exists in the literature of the 20th century because researchers were not always confident about which of these theories was applicable. Finally, $2.4 chronicles previous work done in the area of bubble growth from supersaturated liquid solutions.

2.1 Early Work of the 20th Century on Bubble Formation From Supersaturated Liquid Solutions

The classic studies of Kenrick *et al.* (1924) focused on describing the onset conditions for bubble formation in supersaturated liquid solutions. By using ultra-pure water and clean, smooth glass-walled containers, bubbles did not form in the bulk solution for supersaturation ratios above 100 and they did not begin to form on the walls until supersaturation ratios started to approach 100. Shalung water with either oxygen or CO_2 under pressure was performed to create the supersaturated solutions. The reported supersaturation levels may in fact be lower since 100% saturation efficiency was assumed.

The extreme supersaturation ratios that water can withstand without forming bubbles was first contrasted to the ease of forming bubbles by vibration or the turbulent flow of supersaturated liquid solutions by Dean (1944). For supersaturated liquid solutions at rest, random movements of gas molecules in the solution were thought to be insufficient to cause much bubble formation to occur. Free vortices induced by mechanical disturbances were observed to provide sufficient tension to rupture the liquid and thus form large quantities of bubbles.

Harvey *et al.* (1944a & 1944b) was the first researcher to recognize the importance of pre-existing gas and its effect on bubble formation from gas-supersaturated liquid solutions. The theory that Harvey Nuclei, containing small quantities of pre-existing gas, are preferred sites for bubble formation was named after this author. Harvey initially studied bubble formation in animals and animal cells and identified the parts of

the body that typically formed bubbles upon decompression. It was postulated that the bubbles that did form originated from minute gas nuclei trapped on the surface of cells in contact with bodily fluids. Harvey also conducted laboratory experiments to determine the speed at which glass rods both with and without gas nuclei could be drawn through a slightly supersaturated solution before bubbles formed [Harvey *et al.* (1947)]. With gas nuclei present, a velocity less than 3 m/s resulted in bubble formation. Velocities above 37 m/s were required to form bubbles on the rods when the gas nuclei had been removed.

Pease and Blinks (1947) clearly presented techniques for removing gas nuclei. Gas nuclei present in the liquid or on the test container walls were removed by applying hydrostatic pressures up to 200 atm, partially evacuating the liquid, or heating the liquid to just below the boiling point. After saturation the container was struck with a hammer under different conditions to observe whether or not bubbles would form.

Bernath (1952) was a proponent of Classical Nucleation Theory (CNT), which assumes that bubbles form from an initial size of zero. The author credited Max Volmer, a German scientist of the 1930's, with developing the fundamentals for this theory. Bernath calculated the pressures that would be required to cause the liquids to "fracture" and thus allow bubbles to form. The effect of pre-existing nuclei was not considered in this study.

The growth and solubility of air bubbles in water was initially investigated by Liebermann (1957). Experiments showed that 1 μm air bubbles on hydrophobic particles are not soluble and can exist indefinitely.

2.2 Classical Nucleation Theory (CNT)

2.2.1 Description of CNT

Classical Nucleation Theory (CNT) involves the formation of bubbles from supersaturated liquid solutions starting with an initial bubble size of zero. Random statistical fluctuations are responsible for the formation of a gas nucleus that shrinks if it is smaller than a critical size and grows spontaneously if it is larger than this critical size. The most complete derivation of CNT expressions in existence is presented in Appendix C. This derivation was developed by compiling the works of Zettlemoyer (1969), Ward *et al.* (1970), Blander and Katz (1975), and Wilt (1986) while including more intermediate steps. In this section, the essential features of the theory will be described.

Figure 2-1 shows a plot of the free energy change for a bubble freely suspended in a liquid phase as a function of the bubble radius. This plot is generated from Equation C-11 in Appendix C. Random statistical fluctuations cause gas molecules to collide. Bubbles less than the critical radius (R_C) shrink, while bubbles larger than R_C continue to grow spontaneously. At R_C, the free energy change is at a maximum known as the critical free energy change (ΔF_C). This critical free energy change can be interpreted as the energy barrier that must be exceeded in order for bubble formation to spontaneously occur through homogenous nucleation. The critical free energy change can be used to determine nucleation rates as shown in Appendix C. In this sense, CNT is actually a combination of thermodynamics and kinetics since a thermodynamic term, the critical free energy change, is used to determine the kinetics of nucleation frequency.

Homogeneous nucleation occurs more readily at higher supersaturation ratios. If we assume that saturation efficiency is very high, then pressure ratios are essentially

equivalent to supersaturation ratios. Using Equations C-5 and C-7 from Appendix C and assuming a temperature of 20ºC, critical radius values and the number of gas molecules that correspond to these critical radius sizes are calculated for 5 supersaturation ratios in Table 2-1. It does not seem plausible that more than 24 million gas molecules would readily come together through random statistical fluctuations when the supersaturation ratio was only 5, but it does seem plausible that 78 gas molecules might collide to form a stable bubble that would continue to grow spontaneously when the supersaturation ratio is 2000.

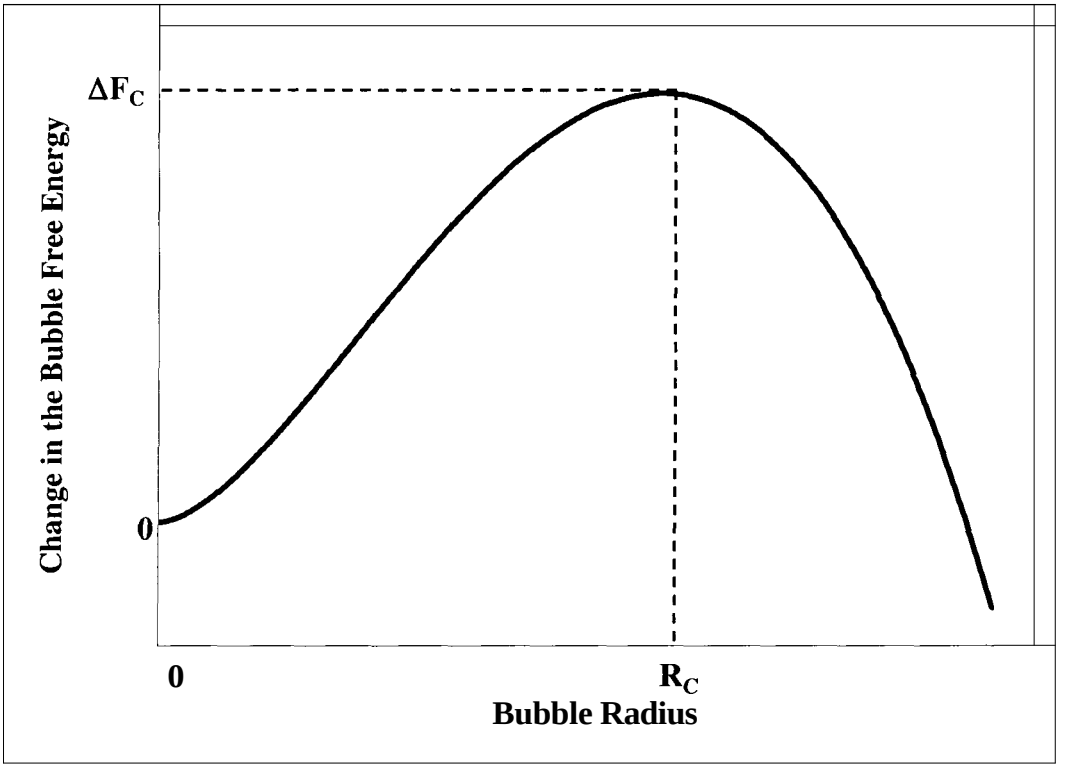

Figure 2-1. Free energy change for a gas bubble as a function of the bubble radius for homogeneous nucleation.

Table 2-1. Calculated critical radius size and number of gas molecules for a number of

Supersaturation Ratio	Critical Radius	# of Gas Molecules
5	3.6×10^{-7} m	24,229,046
10	1.6×10^{-7} m	4,254,208
100	1.5×10^{-8} m	31,962
1000	1.4×10^{-9} m	311
2000	7.2×10^{-10} m	78

In addition to the number of gas molecules in a critically sized bubble decreasing with increased supersaturation ratio, the ratio of solvent to solute molecules also decreases with increased supersaturation ratio. For example, with air dissolved in water at a supersaturation ratio of 5, there would be 17,764 water molecules for every air molecule. With air dissolved in water at a supersaturation ratio of 2000, there would be only 36 water molecules for every air molecule in the solution. Also, for CO_2 dissolved in water at a supersaturation ratio of 5, there would be 414 water molecules for every CO_2 molecule. At a supersaturation ratio of 2000 for CO_2 in water, there would be 1 water molecule for every 1 CO_2 molecule.

The concepts of homogeneous nucleation can be extended to three special cases involving heterogeneous nucleation [Wilt (1986)]. Figure 2-2 illustrates homogenous nucleation along with the three special cases. The appropriate nucleation rate expressions for all of the situations shown in Figure 2-2 are listed in Appendix C. For the same supersaturation ratio and conditions of temperature and pressure the critical radius of curvature for all of the bubbles appearing in Figure 2-2 would be the same. For example, with a 100% saturation efficiency, a supersaturation ratio of 10, a temperature of 20°C, and a final discharge pressure of 1 atm, the critical radius of curvature would be 1.6×10^{-7} m. The number of gas molecules inside the bubbles shown in Figure 2-2 will

vary based on the bubble volume. For homogeneous nucleation and heterogeneous nucleation at a smooth planar interface with a contact angle (θ) of 0", 4,254,208 gas molecules would be inside the critically sized bubble. It does not seem reasonable that this number of gas molecules would combine by a random statistical fluctuation. For heterogeneous nucleation at a smooth planar interface with a contact angle of 100°, 1,578,019 gas molecules would be inside a critically sized bubble. For heterogeneous nucleation at a conical projection with a contact angle of 100" and a cone semi-vertex angle (ω) of 11", the critically sized bubble would contain 3,987,092 gas molecules. Finally, for heterogeneous nucleation at a conical cavity with the same contact angle and cone-semi vertex angle, the critically sized bubble would contain only 29 gas molecules.

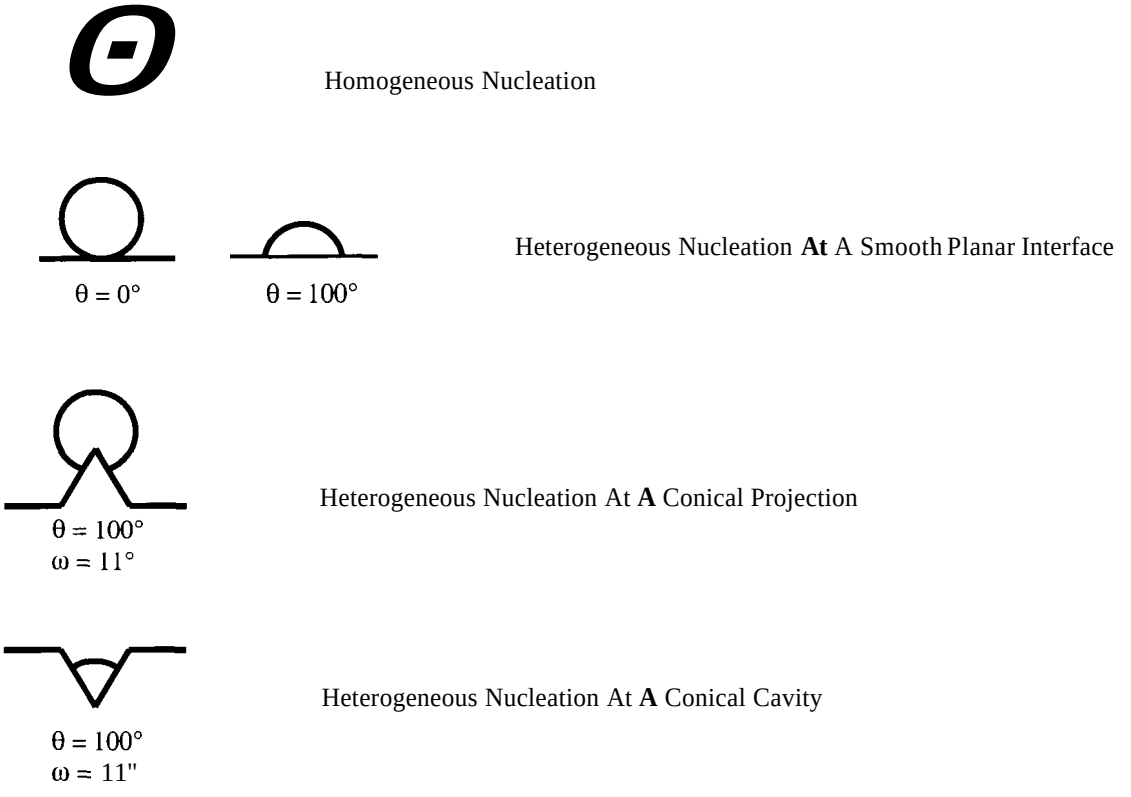

Figure 2-2. An illustration of homogeneous nucleation compared to three special cases of heterogeneous nucleation.

Clearly, heterogeneous nucleation at a conical cavity is highly favored because only 29 gas molecules would be required to combine to form a stable gas nucleus. Figure 2-3 confirms the relative likelihood for bubble formation from an initial bubble size of zero for all of the cases in Figure ***2-2***. In Figure 2-3, the free energy change for homogenous nucleation, heterogeneous nucleation a smooth planar interface ($\theta = 100^{o}$), heterogeneous nucleation at a conical projection, and heterogeneous nucleation at a conical cavity are all plotted as a function the bubble radius of curvature. The plot shows that the energy barrier is highest for homogeneous nucleation and very small for heterogeneous nucleation at a conical cavity.

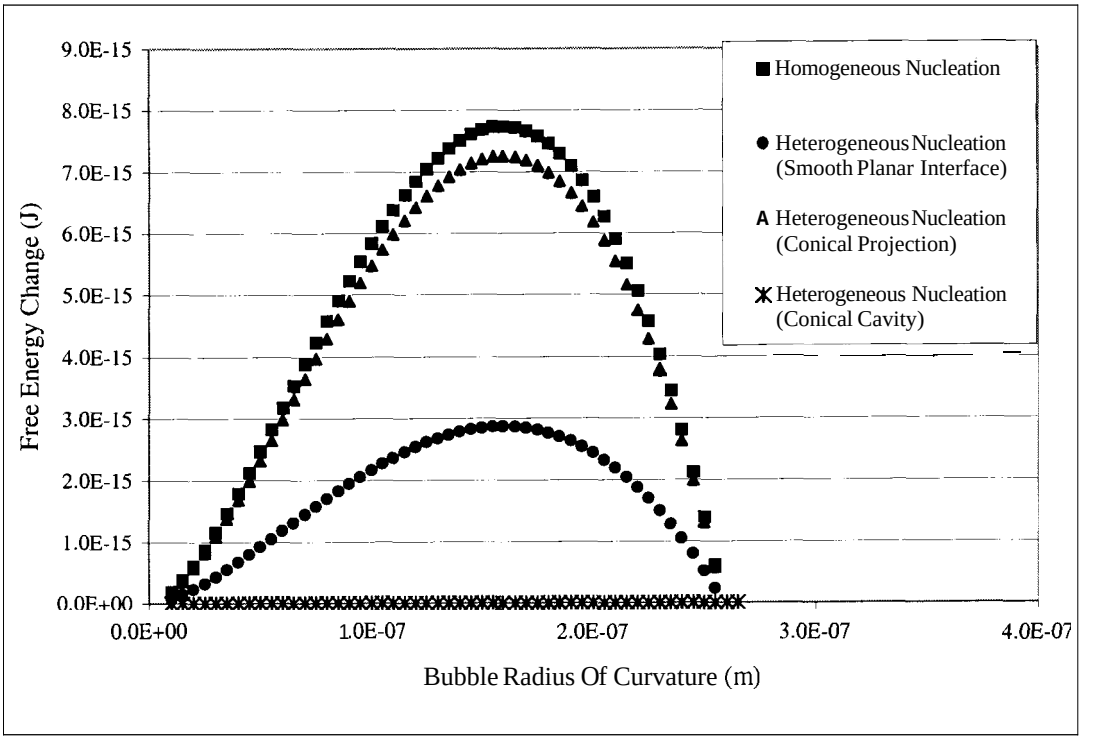

Figure 2-3. Free energy change as a function of the bubble radius of curvature for four cases of bubble nucleation.

2.2.2 Literature Contributions Involving CNT

The addition of an added entropy term to the free energy change was proposed by Lothe and Pound (1962) as well as McDonald (1962 & 1963). These works were primarily theoretical in nature, but some experiments involving the condensation of water droplets from vapor were described. These authors believed that similar expressions would apply to the nucleation of gas bubbles from supersaturated liquids. Blander and Katz (1975) later refined these entropy considerations.

Hill (1963 & 1964) noted that the use of the ideal gas law in CNT for extremely small bubbles is not completely valid. The number of gas molecules in very small bubbles computed using the ideal gas law would only be accurate to within one order of magnitude.

Work performed on nucleation of water in the atmosphere showed that very small supersaturation ratios (1.001-1.005) are all that is required for the formation of rain, snow, fog, or hail [Byers (1965)]. CNT expressions were used to calculate energy barriers that needed to be exceeded in order for water to nucleate in the atmosphere, but the effect of pre-existing water droplets or tiny ice crystals in the atmosphere was not reconciled with the use of CNT expressions involving an initial bubble size of zero.

A new technique for calculating the critical size of a bubble is presented by Weatherford (1970). The effect of solute-solvent interactions is taken into account when determining the critical bubble radius.

Some of the original development of CNT by the German, Max Volmer, was corrected by Hirth *et al.* (1970). Errors in previous theoretical treatments were corrected and new nucleation rate expressions were developed.

Significant experimental research verifying the critical state of bubbles in liquid-gas solutions was performed by Tucker and Ward (1975). By using pressures as low as 150 mm Hg, critical bubble sizes for oxygen bubbles in water were manipulated in the range of 25 to 150 μm. The authors were able to show experimentally that bubbles smaller than the critical size predicted by the Laplace Equation (see Equation C-7 in Appendix C) would shrink, while bubbles larger than the critical size would continue to grow spontaneously. This work is important because it supports the use of Laplace expressions in CNT.

Hemmingsen (1975) conducted experiments to determine the maximum supersaturation levels that supersaturated liquid solutions could endure before the formation of bubbles on smooth glass capillary walls with no gas nuclei could be observed. The supersaturation threshold was 100 for O_2 and Ar in water, 190 for N_2 in water, and 300 for He in water. Bubble formation occurred primarily at the water-glass interface. Bubble nucleation would occur at a smooth interface before occurring homogenously throughout the bulk solution. All of these supersaturation thresholds were significantly reduced by the introduction of crystalline precipitates to the water [Gerth and Hemmingsen (1980)].

Experimental work conducted by Yount and Strauss (1976) was useful in studying the formation of bubbles upon decompression of transparent gelatin. The advantage of using transparent gelatin is that the bubbles formed are stationary and can be easily counted and measured. The pre-application of static pressures successfully removed gas nuclei and resulted in fewer bubbles formed upon successive

depressurizations. An analogy was made to deep-sea divers who become acclimatized to decompression sickness.

Eddington and Kenning (1979) investigated the effect of contact angle on bubble nucleation. Increased contact angles did result in higher nucleation site densities, as would be expected from heterogeneous nucleation theory at a smooth planar interface. It was not clear whether the bubble formation was due to true heterogeneous nucleation or if it originated from pre-existing gas nuclei.

CNT was used to describe bubble formation in dissolved air flotation by Takahashi *et al.* (1979). Flow effects through a depressurization valve were not considered in this study. The turbulence through a depressurizing valve causes much more bubble formation than would be expected through the simple decompression of the liquid in a static environment. More advanced theoretical treatments incorporated CNT for flowing pressure-drop situations. Riznic and Ishii (1989) assumed that most bubbles initially formed due to heterogeneous nucleation at the walls of a depressurization valve while Blinkov *et al.* (1993) assumed that bubble formation occurred uniformly throughout the bulk solution. The flow visualization experiments of Domnick and Durst (1995) indicated that the interpretation offered by Riznic and Ishii was more appropriate.

Wilt (1986) lists the nucleation rate expressions for all of the cases described in Figure ***2-2***. For a supersaturation ratio of approximately 5, these expressions predict that homogenous nucleation and heterogeneous nucleation at a smooth planar interface will not readily occur. The expressions do predict that heterogeneous nucleation will occur in conical cavities for contact angles in the range of 94 – 130". Spherical cavities were later

shown to not be favorable for heterogeneous nucleation under similar conditions [Ciholas and Wilt (1988)].

Rubin and Noyes (1987) created supersaturated solutions through chemical reactions instead of saturation with gas under pressure. The authors claimed to be measuring the thresholds for homogenous nucleation of bubbles, however the thresholds measured were very similar to the heterogeneous nucleation thresholds measured by Hemmingsen. Perhaps incomplete chemical reactions left impurities suspended throughout the bulk water phase that only made it appear as if homogeneous nucleation was observed.

A novel acoustic technique for measuring the nucleation rate of bubbles in supersaturated solutions was developed by Lubetkin and Blackwell (1988). By neglecting the effects of coalescence, estimates on heterogeneous nucleation rates could be obtained and compared to the predictions of classical nucleation theory. The authors reported a favorable comparison.

Kendoush (1989) identified a delay time immediately after depressurization before bubble formation occurred. The delay time, on the order of milli-seconds, was found to decrease as the initial saturation pressure increased. CNT does not predict the presence of a delay time.

Both homogeneous and heterogeneous nucleation rates were measured by Strey *et al*. (1994). Light scattering was used to measure actual nucleation rates as opposed to merely finding the threshold supersaturations at which bubble formation was first observed. The applicability of CNT was verified for critically sized bubbles containing at least 40 gas molecules.

The accelerated bubble formation rates due to turbulence and friction was revisted by Jackson (1994). The experimental research demonstrated that the presence of impurities in addition to turbulence and friction greatly lowers the supersaturations that must be achieved to cause bubble formation.

Bowers *et al.* (1995) rearranged the nucleation rate expressions shown in Appendix C to solve for the nucleation concentration at which bubble formation would begin to occur. In this form, the expressions were used to verify the onset conditions for nucleation. In a following paper, Bowers *et al.* (1996) attempted to account for some discrepancies that were noted upon predicting the onset conditions. In particular, homogenous nucleation was observed to occur at supersaturations far below that predicted by the rearranged CNT expressions. Supersaturations on the order of 1500 – 2000 were theoretically predicted as the thresholds for homogeneous nucleation while the highest threshold supersaturation observed was only 277.

Finally, a recent review article by Jones *et al.* (1999a) helps clarify the applicability of CNT expressions. This article clarifies much of the confusion that exists in the literature on bubble formation from supersaturated liquid solutions. Some investigators did not recognize that CNT expressions could only be used when dealing with an initial bubble size of zero. For those researchers who did realize that no pre-existing gas nuclei should be present in order to accurately measure threshold conditions or nucleation rates, they were not always confident if all of the impurities and pre-existing gas nuclei had been removed. Perhaps the discrepancies, which show larger theoretical supersaturation thresholds for homogeneous nucleation than the experimental observed thresholds, can be explained by the fact that true homogenous nucleation is very

difficult to obtain because the presence of impurities in trace amounts cannot be completely eliminated.

2.3 Harvey Nuclei

2.3.1 Description of Harvey Nuclei

Harvey Nuclei are defined as locations in contact with supersaturated liquid solutions that contain a pre-existing trapped gas and become preferred bubble formation sites [Harvey *et al.* (1944a & 1944b)]. Heterogeneous nucleation situations have been confused by the presence of these nuclei [Ward ***et*** *al.* (1983)]. Naturally occurring Harvey Nuclei have not been previously identified, but they are believed to be as small as 1 μm in size.

2.3.2 Literature Contributions Involving Harvey Nuclei

Bankoff (1958) calculated the conditions for incomplete displacement of gas in groves that had advancing liquid-drop fronts. These conditions are important for determining whether or not a surface defect will be partially wetted and serve as a Harvey Nuclei when subsequently in contact with a supersaturated liquid solution. This work contributes to the confusion in the literature by categorizing the bubble formation from sites that are partially wetted as bubble nucleation. Since these bubbles form from a non-zero initial bubble size, this is not bubble nucleation.

The first artificial bubble producing site for gas-supersaturated solutions, modeled after a Harvey Nuclei, was developed by Buehl and Westwater (1966). Figure 2-4 contains a schematic of the authors' artificial site, which was machined from a copper block. Experiments were conducted using CO_2 in water at supersaturation ratios less than 5 with the surface near the site opening coated with various non-wetting agents to study the effect of contact angle on bubble growth rates. Some pre-existing gas in the cavity

grew, forming a bubble at the site opening, and detaching after growing to a larger size. After a lapse in time, another bubble formed at the site and continued the cycle of bubble production. No effect of contact angle on the growth rate could be detected. Buehl and Westwater erroneously referred to their site as a bubble nucleation site, but this does not invalidate their results, which focused on the observable bubble growth from the site. A bubble radius and contact angle *vs.* time plot for seven consecutive bubbles forming from the Buehl and Westwater site appears in Figure *2-5*. Results from Figure 2-5 were analyzed to determine the first observable bubble size, bubble size at detachment, "nucleation" lapse time (the time interval between the detachment of one bubble and the first observance of the next bubble), and the bubble growth time. The results appear in Appendix B for comparison with the soda bottle experiments described in Chapter **3.**

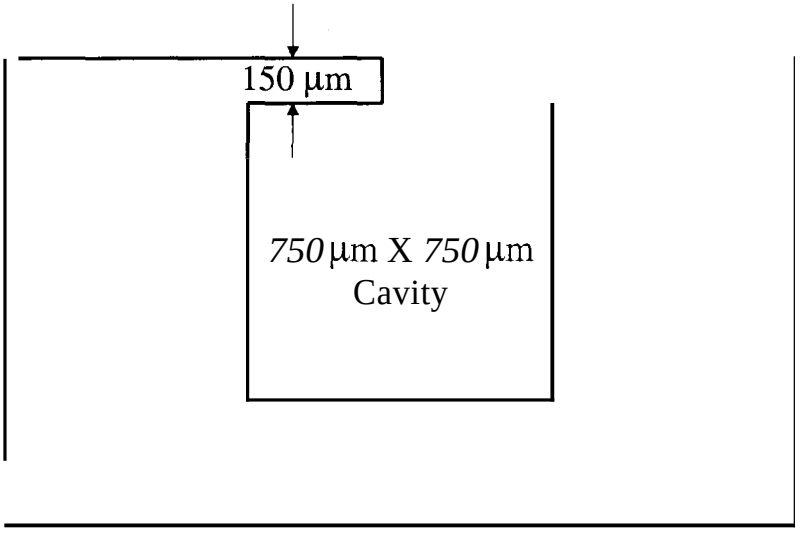

Figure 2-4. Artificial bubble producing site used by Buehl and Westwater (1966).

The importance of contact angles in surface science studies was noted by several researchers, including Ginn *et al.* (1968), Hamilton (1972), Good (1973), Neumann *et al.* (1976), and Finch and Smith (1979). It was agreed that hydrophobic surfaces would be more likely to have sites that would behave as Harvey Nuclei. **A** site is more likely to trap gases if it is at least partially hydrophobic.

Apfel (1970) extended the concept of Harvey Nuclei to free floating impurities in supersaturated liquids. Impurities less than 10 μm in size are controlled more by Brownian motion than gravitational forces and tend to remain suspended in liquids for prolonged periods of time. Small amounts of trapped gases in these suspended impurities are responsible for bubble formation in the same way that Harvey Nuclei on the surfaces of container walls can be responsible for bubble formation.

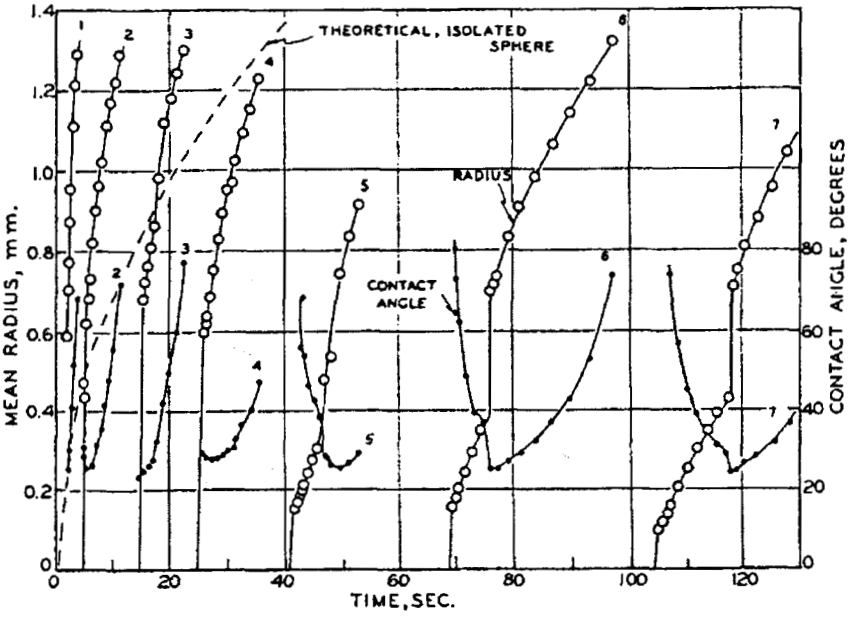

Figure 2-5. Radius and contact angle measurements for seven consecutive bubbles of carbon dioxide forming at the bubble producing site of Buehl and Westwater.

A scattered light technique for measuring the spectrum of bubble nuclei suspended in a water sample was developed by Keller (1972). This work confirmed that pre-existing bubble nuclei can remain stabilized and suspended in a liquid solution.

The deactivation of Harvey Nuclei was discussed by Winterton (1977). By applying high static pressures to water samples, Harvey Nuclei containing small amounts of gas may be deactivated if the pressure is high enough to cause liquid to completely wet all surface cavities. **A** rigorous Thermodynamic analysis of the stability of bubble nuclei was prepared by Ward and Levart (1984).

The works of Ryan (1991) and Ryan and Hemmingsen (1993) detail the formation of bubbles in water at smooth hydrophobic surfaces. Smooth hydrophobic surfaces formed relatively few bubbles with supersaturation ratios ranging from 5 to 50. This work suggested that the surface defects and irregularities were more important to the formation of bubbles than the hydrophilic/hydrophobic nature of the surfaces.

Bisperink and Prins (1994) also created an artificial bubble producing site to study the growth of bubbles from carbonated liquids. Figure 2-6 shows the artificial Harvey Nuclei that the authors created. The tip of a smooth glass capillary tube was melted down to a smaller size and plugged with glue. **A** small amount of gas is trapped in this cavity thus making it a preferred site for bubble formation when suspended in a supersaturated liquid solution.

Zhou ***et*** *al.* (1998) showed experimentally that contact angles on hydrophobic particles do not have to exceed 90" in order to produce bubbles. The authors claimed that this disproves CNT, which requires a contact angle greater than 90" in order for any form of heterogeneous nucleation to occur. Once again, the authors confused the fact that in

their experiments pre-existing gas nuclei were present and in CNT situations, all surfaces and impurities are completely wetted.

The recent work of Jones *et al*. (1998 & 1999b) examines the entire cycle of bubble production at a Harvey Nuclei site. Bubbles formed at the site opening, grew in such a pattern that a bubble diameter squared versus time plot yielded a straight line, detached, and formed a new bubble after a lapse time interval. The authors called this lapse time interval a "nucleation" lapse time, even though they believed that the detaching bubble left part of itself behind to eventually form the next observable bubble. They realized that the use of the term "nucleation" to describe this event was a misnomer. The authors also postulated that larger detaching bubbles would have longer "nucleation" lapse times due to the presence of a larger depleted dissolved gas zone surrounding the site opening.

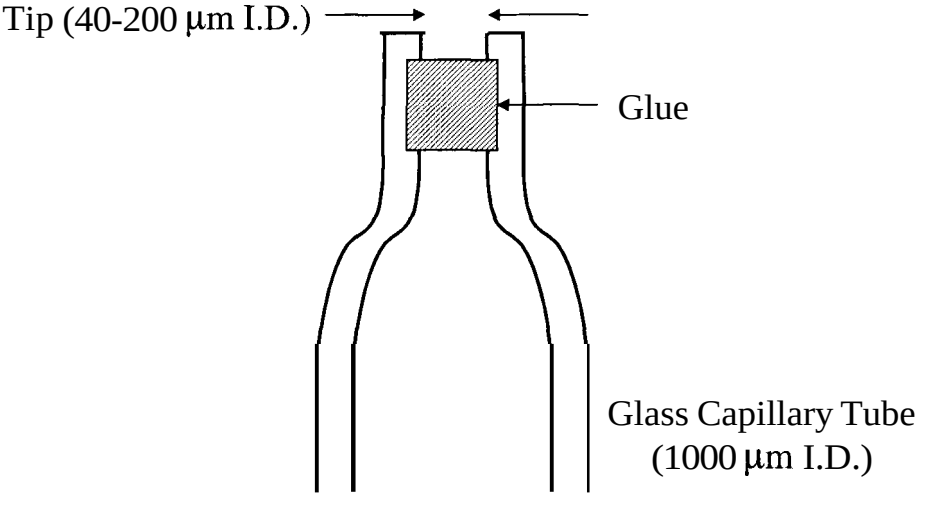

Figure 2-6. Artificial bubble producing site used by Bisperink and Prins (1994).

2.4 Bubble Growth from Supersaturated Liquid Solutions

Regardless of whether bubbles form in supersaturated liquid solutions because of CNT or because of Harvey Nuclei, it has been observed that they will continue to grow if the surrounding liquid remains supersaturated. Research on the bubble growth event will now be reviewed.

Epstein and Plesset (1950) developed a model for describing the growth or dissolution rate of gas bubbles in supersaturated or undersaturated liquid solutions. An approximate diffusion-only solution, neglecting the convective effects from the translational motion of the bubble, was introduced. Manley (1960) more clearly presented this approximate diffusion-only solution by extending the earlier work of Epstein and Plesset. Details of Manley's bubble growth model will be presented in §7.1.1.

Scriven (1959) was able to produce a model that incorporated both diffusive and convective effects. This model described the phenomena of spherically symmetric phase growth in an infinite medium controlled by either heat or mass transfer. Details of the Scriven model will be presented in §7.1.2.

Barlow and Langlois (1962) reported the earliest computer solution to the bubble growth problem. This model considered the growth of a gas bubble within a volume of isothermal viscous liquid containing dissolved gas that is distributed uniformly. The authors neglected convective effects, considering a diffusion-only solution.

Work on the growth of bubbles during electrolysis was presented by Glas and Westwater (1964). Bubble growth by electrolysis was shown to be mathematically

analogous to bubble growth by either heat or mass transfer, It was noted that the square of the bubble diameter *vs.* time measurements was linear, suggesting that the bubble growth was dependent on the area available for mass transfer. Bubble growth rates were not influenced by the contact angles of the bubbles on the electrode surfaces.

Bankoff (1966) also postulated a diffusion-controlled bubble growth theory, in which convective effects were neglected. The author argued that convective effects would only be important during the early stages of growth. Pressures inside the bubble were calculated using the Laplace equation (see Equation C-6 in Appendix C).

Theoretical work on bubble growth in constant and time-dependent pressure fields was formulated by Theofanous *et al*. (1969). Bubble growth in time-dependent pressure fields was studied to better understand the effect that two-phase flow can have on bubble growth rates. Time-dependent pressure fields were shown to affect bubble growth rates by changing the quantity of dissolved gases in solution available for mass transfer. Work on bubble growth in variable pressure fields was later continued by Jones and Zuber (1978).

Bubbles located in sound fields with sufficient pressure amplitudes can also be caused to grow by the mechanism of rectified diffusion [Eller (1969)]. In fact, bubbles that would ordinarily dissolve in a liquid may be seen not to dissolve, but to grow, when located in a sound field of sufficient strength. The calculated and experimentally observed thresholds for significant bubble growth by rectified diffusion limits its importance to situations involving turbulent cavitating flows. This work was later continued by Fyrillas and Szeri (1994).

Tao (1978) presented a new exact series solution to the problem of bubble growth. Isothermal growth or dissolution of gas bubbles was assumed to be influenced by diffusion without convection. The series solution breaks down for bubble growth at higher dissolved gas concentrations, but can always be found for bubbles in undersaturated solutions.

Another numerical analysis of bubble growth in supersaturated liquid solutions appears in Cha and Henry (1981). Numerical results were found to compare favorably to the original Epstein and Plesset (1950) model for constant pressure fields. The behavior of gas bubbles in variable pressure fields is also presented as a special case.

Shaffer (1981) attempted to model the growth of gas bubbles by diffusion in clay coatings. The non-Newtonian nature of the clay coatings was not considered, but the effects of liquid density, surface tension, liquid viscosity, diffusivity, concentration of the dissolved gas, and initial bubble size were all considered. Changes in the initial bubble size influenced the progression of bubble radius throughout time.

The experiments of Toda and Kitamura (1983) proved that convective effects during bubble growth can be large and that they should not be neglected. The growth of bubbles activated by laser beams was studied to help quantify the convective effects. Previous diffusion-only solutions were argued to be invalid for all but the lowest supersaturation ratios, thus increasing the popularity of the Scriven (1959) model, which included both diffusive and convective effects.

The work of Li and Yortsos (1995) is an example of research that adopted aspects of the Scriven solution. Li and Yortsos studied the growth of a complicated network of bubbles in a porous media. Scriven's solution, describing the growth of a single bubble

in an infinite medium due to either heat or mass transfer, was applied to the entire network of bubbles.

The model described by Venerus and Yala (1997) was also patterned after the Scriven theory. This model extends the Scriven theory so that transport problems involving high viscosity polymers can be solved.

Finally, Jones *et al*. (1999b) showed that bubble diameter squared is a linear function of time for bubbles growing from dissolved gases. This is the same relation exhibited by bubbles that grow in the presence of electrolytic fields. It seems that both modes of bubble growth depend on the area available for mass transfer. The Scriven growth model was also used by Jones *et al*. in evaluating the growth cycle of bubbles originating from a Harvey Nuclei.

3. Soda Bottle Experiments

Preliminary experimental studies were conducted using carbonated beverages in glass and PETE soda bottles. Glass bottles with 296 mL of Schweppes® Tonic Water were used in most of the experiments along with a few PETE soda bottles with 591 mL of Sprite@for comparative purposes. About 20-30 bubbles initially appeared on the container walls and throughout the bulk upon opening both the glass and PETE soda bottles. After one minute, it was not uncommon for the glass container to produce no further bubbles, while large quantities of bubbles were always observed to form on the inside surfaces of the PETE soda bottle. Figure 3-1 shows some ESEM images of the inside surfaces of both **a** glass and a PETE soda bottle. Despite the fact that both of these surfaces appeared to be smooth, no bubbles were produced at the surface of (a), while several were produced at the surface of (b). This can be attributed to the fact that the glass surface is hydrophilic, so it does not readily trap gases on its surface while the PETE is hydrophobic and does readily trap gases on its surface.

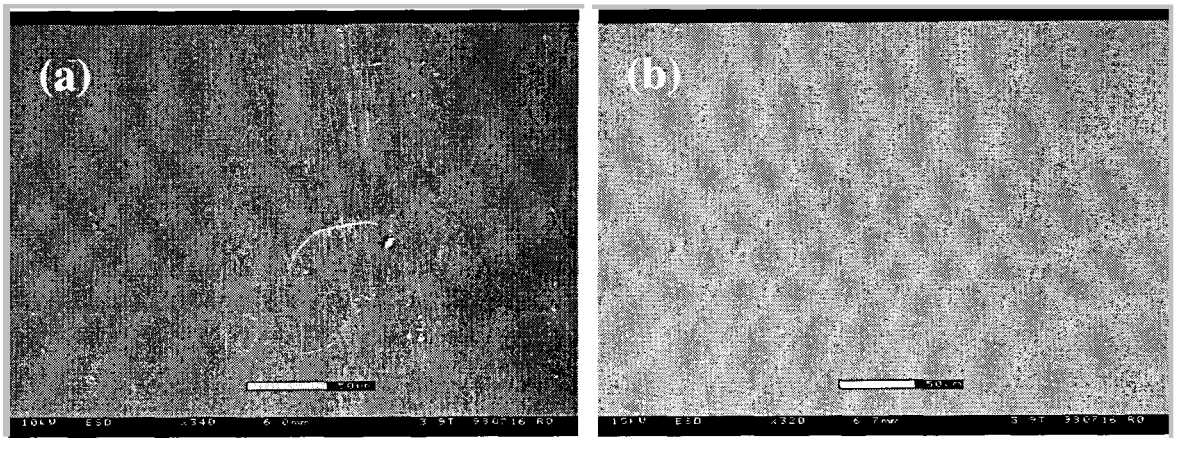

Figure 3-1. ESEM pictures of the inside surface of (a) glass soda bottle and (b) PETE soda bottle. Both white reference bars represent 50 μm.

3.1 Bubble Growth Patterns From Sites In Glass Soda Bottles

The results of a more systematic investigation of the behavior of bubbles forming on the inside surface of glass soda bottles appear in Table 3-1. Ten bottles were opened at t = 0 and the number of sites producing bubbles were tracked as a function of time over a period of four days. Bubbles formed in a very consistent cyclical pattern at these sites. Six of the ten bottles had no sites producing bubbles while the remaining four bottles had one to four sites. Only two of the bottles continued to produce bubbles after 30 minutes. Sites tended to deactivate with time, but bottle #2 and bottle #6 actually experienced some reactivation at the 72 hrs and 48 hrs times, respectively.

Table 3-1. Number of bubble producing sites observed in ten glass soda bottles as a function of time.

Bottle#	1 min	30 min	24 hrs	48 hrs	72 hrs	96 hrs
1						
2	4	2	1	1	2	2
3						
4						
5						
6	1	1		1	1	1
7	3					
8						
9	1					
10						

The rate at which bubbles formed was also determined for some of the glass bottle sites that repeatedly produced bubbles from the same locations at the container wall. Figure 3-2 reports the rates from two sites in a glass soda bottle as a function of time. The bubble formation rate in bubbles per minute was determined by visually counting the

number of bubbles that appeared in a 30 second time interval. Bubble formation rates remained at 100-130 bubbles per minute at both sites for the first 40 minutes. During the first 40 minutes, the bubble formation rate at each site appeared to occur at a very regular and consistent pattern from bubble to bubble. Site #2 became deactivated just after the 50 minute mark while site #1 continued to produce bubbles even after 300 minutes.

To further investigate the regularity of these bubble growth patterns, an Encore MAC™ High-speed Video Camera (Olympus America Inc., Melville, NY) was used to record the behavior of individual bubbles originating from the same site. This high-speed camera was used in conjunction with a Makro-Kilar Zoomar lens (Zoomar, Munich, Germany) and a Series 180 Fiber-Lite System with gooseneck attachments (Dolan-Jenner Industries, Lawrence, **MA)** to provide frontal lighting.

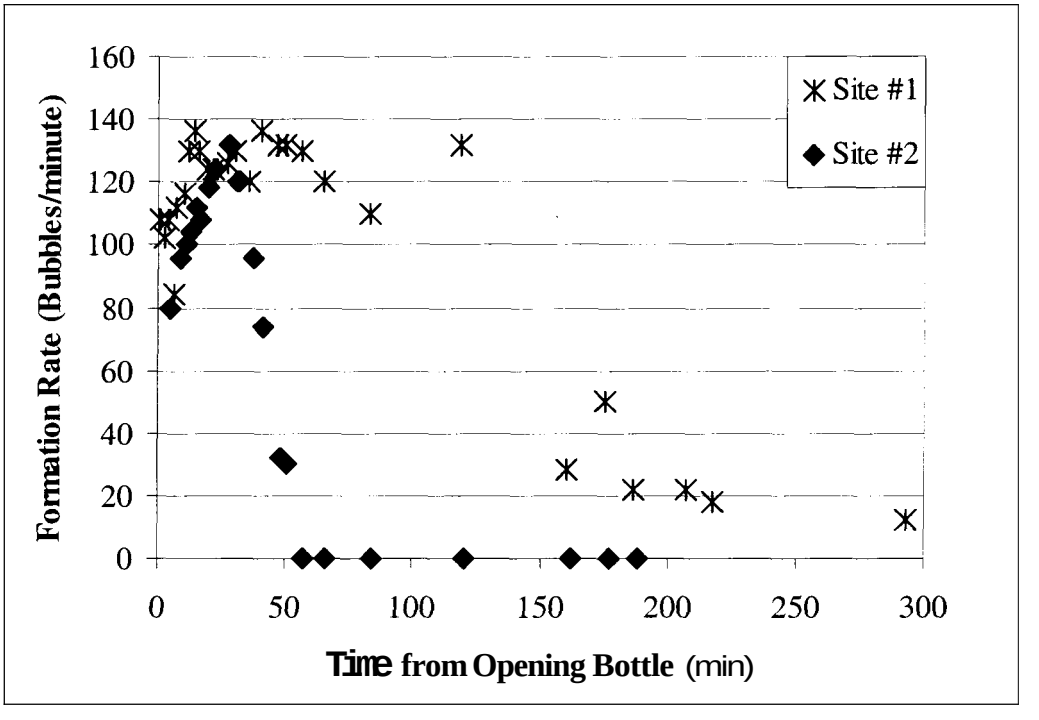

Figure 3-2. Bubble formation rates from two sites in a glass soda bottle.

Figure 3-3 shows a typical high-speed video sequence of a bubble growing at a bubble producing site. After its first appearance, the bubble grows to a point at which detachment occurs and then after a lapse time interval the cycle repeats itself. After analyzing these high-speed video sequences, bubble diameter versus time plots were created. An example of one of these plots appears in Figure 3-4.

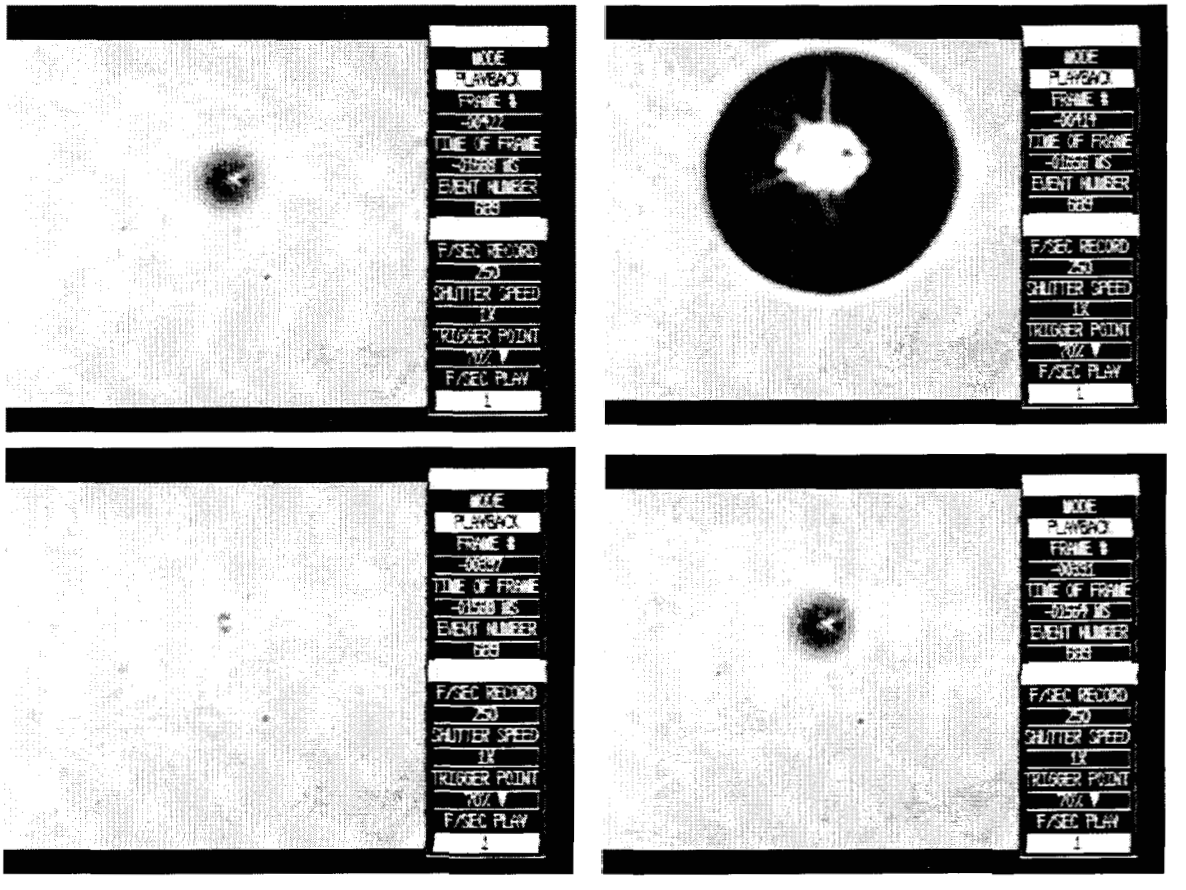

Figure 3-3. High-speed video sequence of bubble growth: (a) first appearance of bubble, (b) 32 ms later the bubble has grown to a significantly larger size, (c) 68 ms later the bubble has detached and the two dark defects located one above the other near the center appear to be the actual bubble formation site on the wall of the glass bottle, and (d) 24 ms later the bubble reappears and begins the cycle once again. The bubbles appearing in (a) and (d) are approximately 25-30 μm in diameter.

The plot in Figure 3-4 illustrates the regularity at which bubbles form at a bubble producing site in the container wall of a glass soda bottle. The six curves represent six consecutive bubbles forming at the same site. All six bubbles have very similar first observable bubble sizes, bubble sizes at detachment, lapse times between the detachment of one bubble and the first observance of the next bubble (what some other researchers have referred to as a "nucleation" lapse time), and bubble growth times.

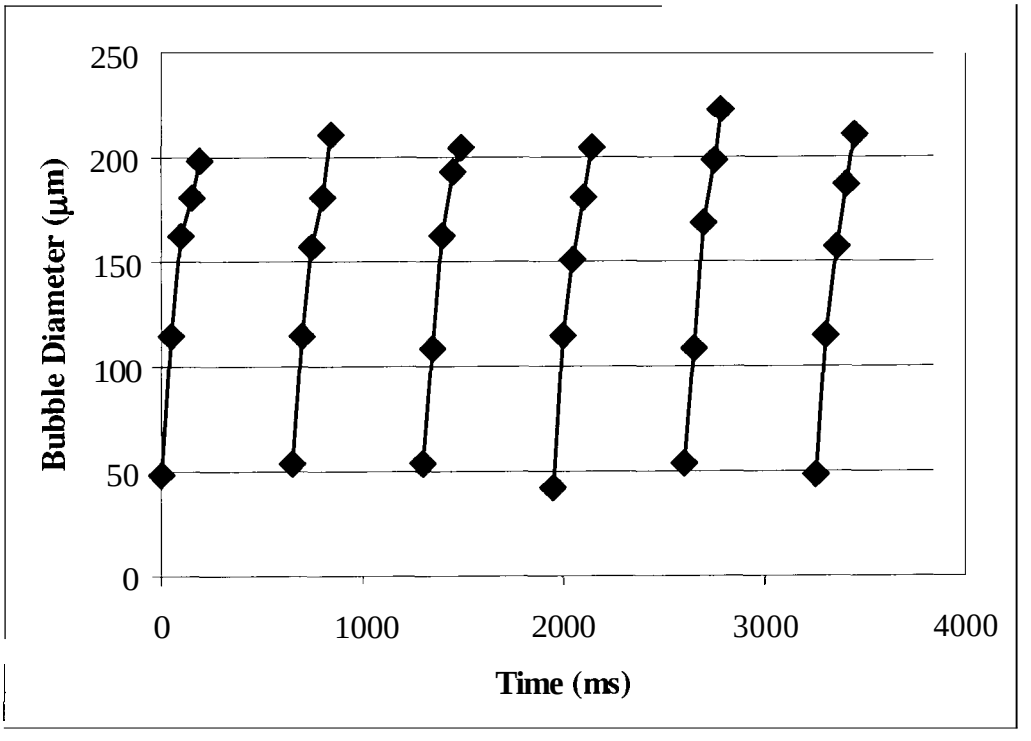

Figure 3-4. Bubble diameter versus time for six consecutive bubbles at a bubble producing site in a glass soda bottle soon after depressurization.

In Appendix B, raw data from several soda bottle trials measuring first observable bubble size, bubble size at detachment, "nucleation" lapse time, and bubble growth time are reported. Averages and ± 95% confidence intervals for the data presented in Figure 3-4 (same as Trial #1 in Appendix B) are: first observable bubble size = 50.2 ± 3.9 pm, bubble size at detachment = 208.8 ± 6.6 pm, "nucleation" lapse time = 461.2 ± 1.6 ms, and bubble growth time = 195.7 ± 1.2 ms. The small size of the confidence intervals compared to the averages shows the incredible regularity observed at these sites. Similar regularity was observed in all of the other soda bottle trial results reported in Appendix B. There was more variability in the measurements of Buehl and Westwater (1966), but these measurements were taken on bubbles that grew to significantly larger sizes.

The regularity of the nucleation lapse time data, in particular, from these soda bottle measurements disproves the applicability of Classical Nucleation Theory (CNT). If CNT did explain the nucleation lapse time behavior, it would not be expected that these lapse times would be so regular, since the nucleation process involves random statistical fluctuations to produce a stable gas nucleus in a gas-supersaturated liquid solution. Lapse times that are 461.2 ± 1.6 ms are not likely to occur if the gas nucleus has to form from a zero initial size every time (as it theoretically would if CNT applied). The regularity of the lapse times suggests that part of the bubble is being left behind at detachment and it continues to grow, thus forming the next bubble. The observation of a lapse time is due to the fact that there is a period of time when the bubble is not visible. To call this lapse time a "nucleation" lapse time as has often been done in the literature is a misnomer.

If bubble diameter versus time curves for bubbles growing in gas-supersaturated liquid solutions are re-plotted as bubble diameter squared versus time plots, straight line

fits can be obtained. Figure 3-5 displays an example of one of these straight line fits taken from the second curve in Figure 3-4. The R-squared values for all six of the resulting bubble diameter squared versus time straight line fits for the data shown in Figure 3-4 are 0.9843, 0.9943, 0.9863, 0.9990, 0.9929, and 0.9994. These six R-squared values, all close to 1.0000, verify that a bubble diameter squared versus time plot does yield a straight line. The fact that bubble diameter squared versus time plots yield straight lines suggests that bubble growth depends on the area available for mass transfer.

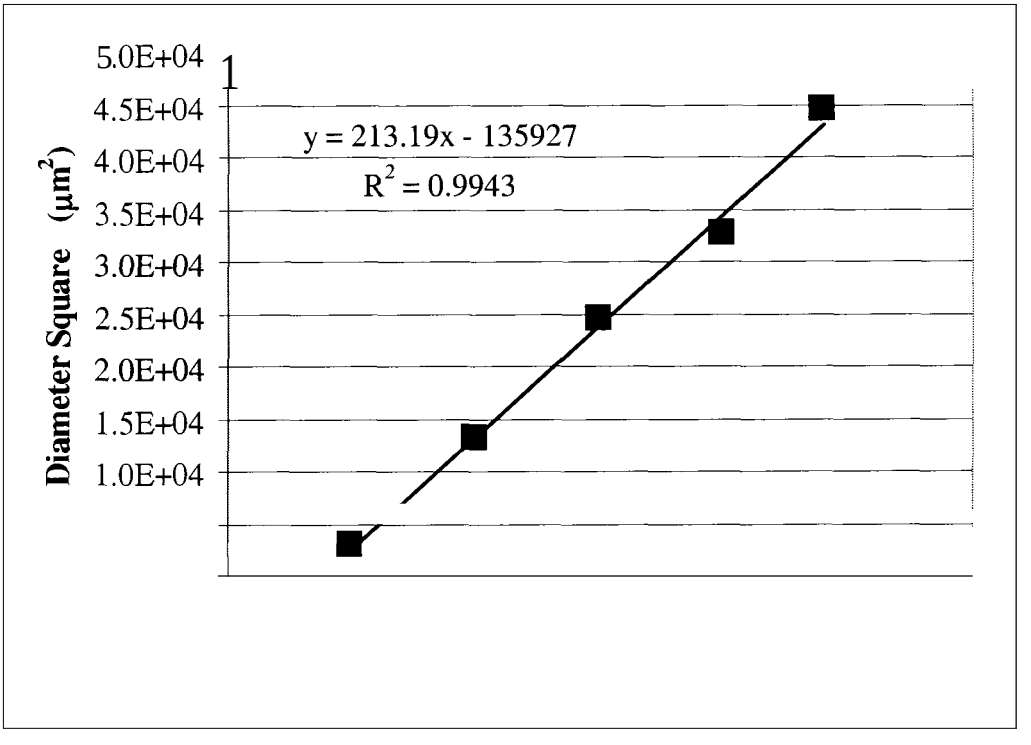

Figure 3-5. Sample of regression analysis performed on a diameter squared versus time plot (from the second bubble curve in Figure 3-4).

3.2 Bubble Producing Site Identification

The fact that some glass bottles produce no bubbles, while others cause some bubbles to form at one or a few sites, suggests that there must be something special about the site itself that makes bubble formation at that location more favorable. A number of techniques are available for characterizing these sites, including stylus profilometry, atomic force microscopy (AFM), environmental scanning electron microscopy (ESEM), and video microscopy. The primary difficulty with all of these techniques lies in finding the location of the site, itself. This is why most previous investigations of nucleation involve artificial nucleation sites of some known geometry.

Initial attempts were made to analyze cut-out samples of glass bottles that contained a bubble producing site using the stylus profilometry and ESEM techniques. Scans were made with an Alpha-Step 200 Stylus Profilometer (Tencor Instruments, Mountain View, CA), but these scans tended to show the curvature of the bottle surface itself and little else. An AFM would have provided superior surface scans since the probe tip is much smaller, but with the exact site location unknown, it would have taken a very long time to identify it using an AFM. Pictures of features near the bubble production site from an Electro Scan ESEM (Philips Electron Optics, Hillsboro, OR), in hindsight, appear to be pictures of dust or other debris contaminating the surface.

Video microscopy techniques were re-visited in an attempt to identify the bubble producing sites. A conventional XC-75 CCD camera (Sony, San Diego, CA) was used instead of the high-speed camera. Also, lighting was improved by switching from front to back lighting. This change in lighting resulted in higher quality images that allowed

for site identification. One of these higher quality images is reproduced in Figure 3-6. The large image in Figure 3-6 clearly shows a bubble attached to a "nucleation" site. It is believed that this is the first photograph in the literature of a naturally occurring bubble producing site. The attached bubble is being pulled upward by buoyancy forces, explaining why the site appears in the lower part of the see-through center region of the bubble. The four smaller images in Figure 3-6 show views of the site itself after it was cut away from the glass bottle and examined using a microscope. These four smaller images are at four different focus depths and show that there is a hole in the wall of the soda bottle that is responsible for trapping the gases that initiate the cyclical pattern of bubble production.

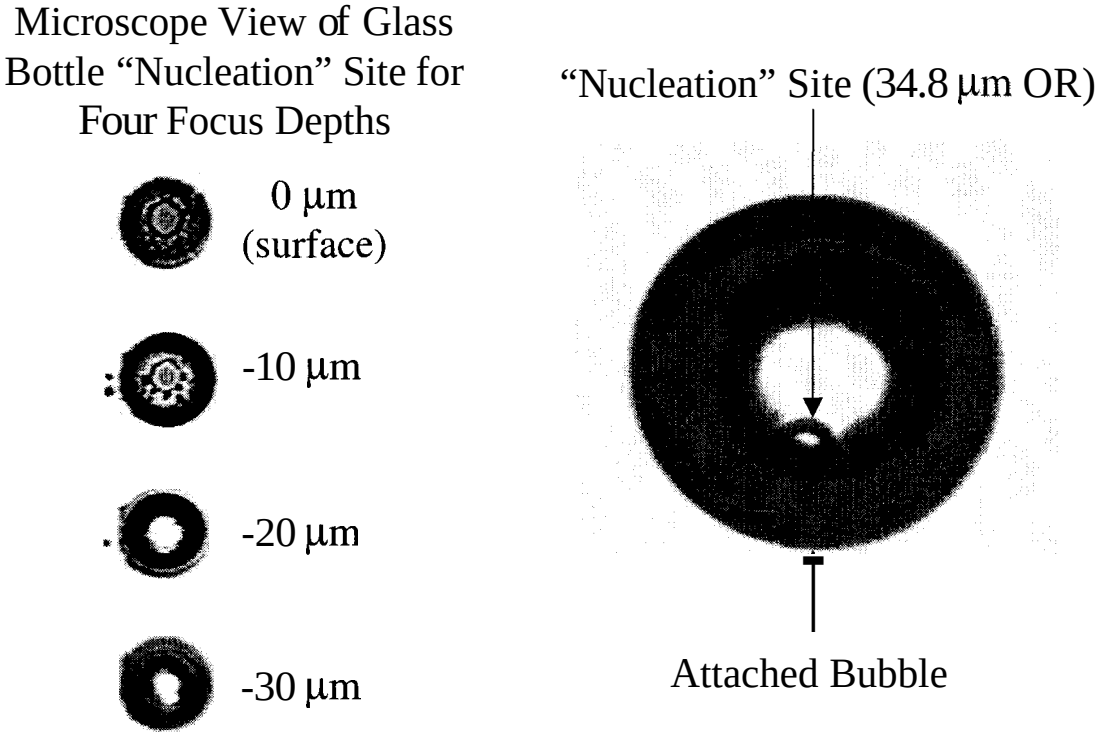

Figure 3-6. View of attached bubble growing at a "nucleation" site with microscope pictures at four different focus depths.

Using this improved lighting technique with the video equipment, a similar shaped defect in the glass was found for all future bubble production sites examined. All of the defects were circular with outside diameters ranging from 25.6 to 37.8 pm. The inside diameter of the defects was usually more irregular in shape with diameters ranging from 6.7 to 12.9 pm. The circular nature of the bubble formation sites suggest that they were formed by air bubbles in the molten glass that formed a defect in the glass upon cooling. Defects that were close enough to the inside wall of the soda bottle could trap gases and be responsible for a series of bubbles forming at that location.

3.3 Observed Relationship Between Detachment Diameter and "Nucleation" Lapse Time Data From Soda Bottle Experiments

Jones et al. (1998) speculated that there should be a direct correlation between the bubble detachment diameter and the "nucleation" lapse time. The authors believed that a bubble with a larger detachment diameter would have a longer "nucleation" lapse time between successive bubbles. To see if such a correlation exists, all of the soda bottle measurements for bubble detachment diameter and "nucleation" lapse time taken 15 minutes after depressurization in Appendix B were plotted in Figure 3-7. This plot of bubble detachment diameter (D_{max}) versus lapse time resulted in no correlation. Variability in the depth and opening size of the bubble producing sites in the soda bottle inside walls could be responsible for the absence of a correlation here.

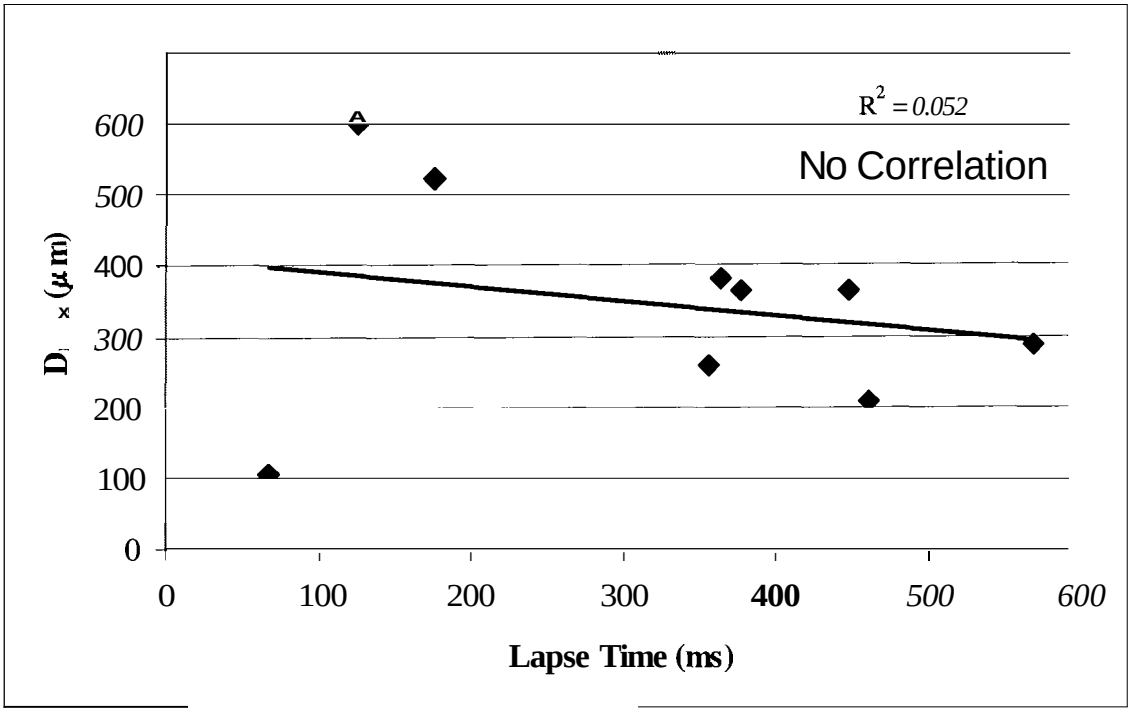

Figure 3-7. Bubble detachment diameter (D_{max}) versus lapse time for nine distinct bubble producing sites (all measurements taken approximately 15 minutes after depressurization).

3.4 Soda Bottle Time Study

For Trial #9 in Appendix B, measurements on the bubble growth behavior were taken over a 96 hour period following depressurization. The results of this study appear in Figure 3.8. Throughout this study, bubble detachment diameters were virtually unchanged, as was expected. Both the lapse time and bubble growth times tended to increase with time. This can be explained by the fact that the dissolved gas concentration would also be decreasing with time. Bubble growth would be slower at lower dissolved gas concentrations.

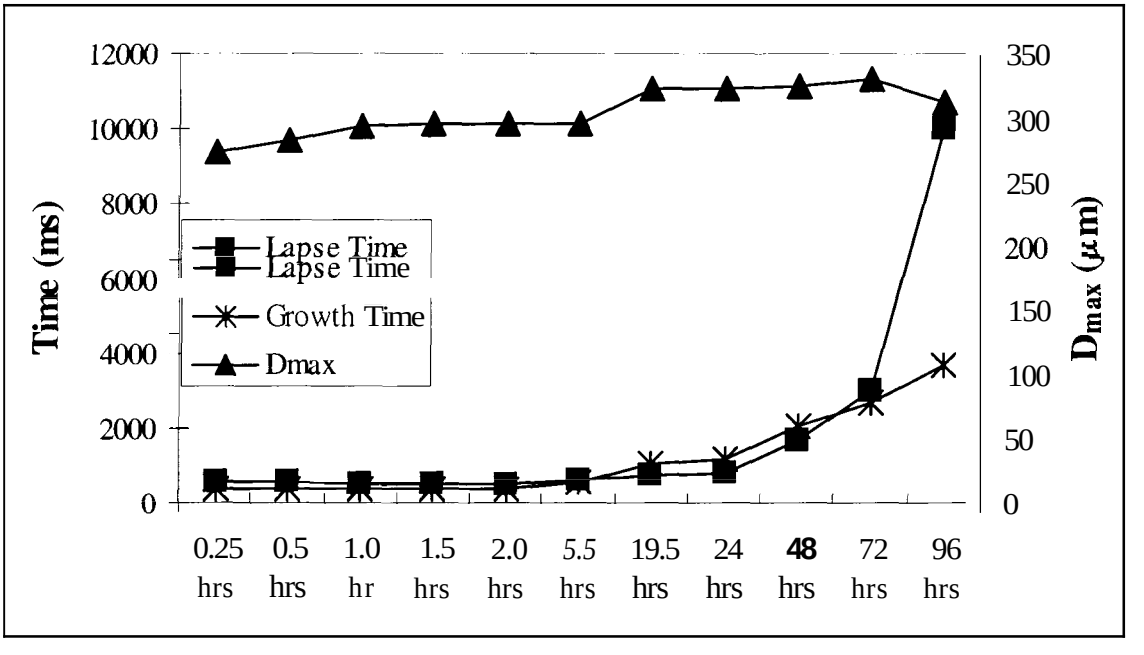

Figure 3-8. Time study of a single bubble formation site over a 96 hour period.

3.5 Deactivation and Reactivation of Bubble Producing Sites

As shown earlier, bubble producing sites tended to deactivate over time, but methods were also developed that led to more immediate deactivation and even reactivation of the sites. It was first observed that if the carbonated liquid in a soda bottle is removed and then poured back into the bottle, sites that were active before continued to remain active. It was believed that the bubble producing site remained partially wetted, even after removing the carbonated water. This would leave some gas remained trapped behind in the bubble producing sites. Upon refilling the bottle with carbonated liquid again, the site would resume a cyclical pattern of bubble production.

The key to deactivating one of these sites is to completely wet the bubble producing site. After pouring out the carbonated liquid from a soda bottle, a 200 proof ethanol solution was used to rinse out the bottle. Ethanol was chosen because it easily wets glass surfaces. After the ethanol rinse and refilling of the bottle with carbonated liquid the site did indeed remain inactive.

If sites can be deactivated by removing gases trapped in surface defects, it seems reasonable that sites could be reactivated by trapping additional gases in these defects. After deactivating a bottle with an ethanol rinse, the empty bottle was put at the end of a compressed air line, which had a discharge pressure of 25 psig. **A** stream of air from the compressed air line was allowed to flow to the inside of the bottle for about a minute while the bottle was slowly rotated. The re-addition of carbonated liquid to the bottle resulted in not only the reactivation of the original bubble producing site, but also about

10-15 additional sites inside the bottle. These additional sites required the direct application of a gas to ensure that the sites would produce bubbles in a cyclical pattern.

Both Trial #7 and #8 in Appendix B involved the reactivation of a bubble producing site ten days after the bottle was initially opened. Figure 3-9 shows the behavior of the bubble producing site in Trial #8 about 15 minutes after depressurization. This can be compared to Figure 3-10, which displays the bubble growth characteristics at the very same site that was reactivated by allowing air to flow into the empty bottle 10 days later. After reactivation of the site, fresh carbonated liquid was poured back into the bottle and the bubble growth characteristics were re-observed. For the data in Trial #8, both the "nucleation" lapse times and bubble growth times were longer after reactivation. This could be attributed to the fact that pouring carbonated liquid back into the bottle naturally lowers the supersaturation level, resulting in a lower dissolved gas content. Lower dissolved gas contents would lead to longer "nucleation" lapse times and bubble growth times. Bubble detachment diameter increased from $259.4 \pm 1.6 \mu m$ to 340.8 ± 3.3 pm. Perhaps the application of the compressed air increased the opening of the site, thus causing an increase in the bubble detachment diameter. Trial #7 showed a similar increase in the "nucleation" lapse times and bubble growth times upon reactivation. Bubble detachment diameters were very similar; however, with $660.6 \pm 6.5 \mu m$ about 15 minutes after depressurization and 607.5 ± 0.0 pm after reactivation 10 days later.

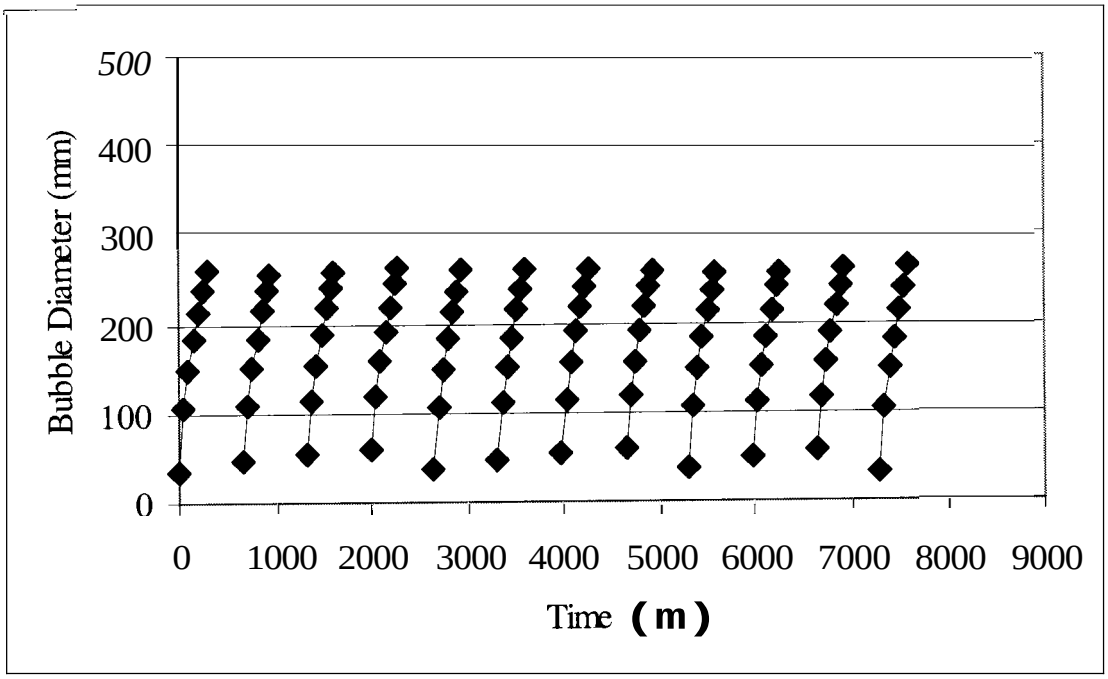

Figure 3-9. Bubble diameter versus time plot for Trial #8 in Appendix B (15 minutes after depressurization).

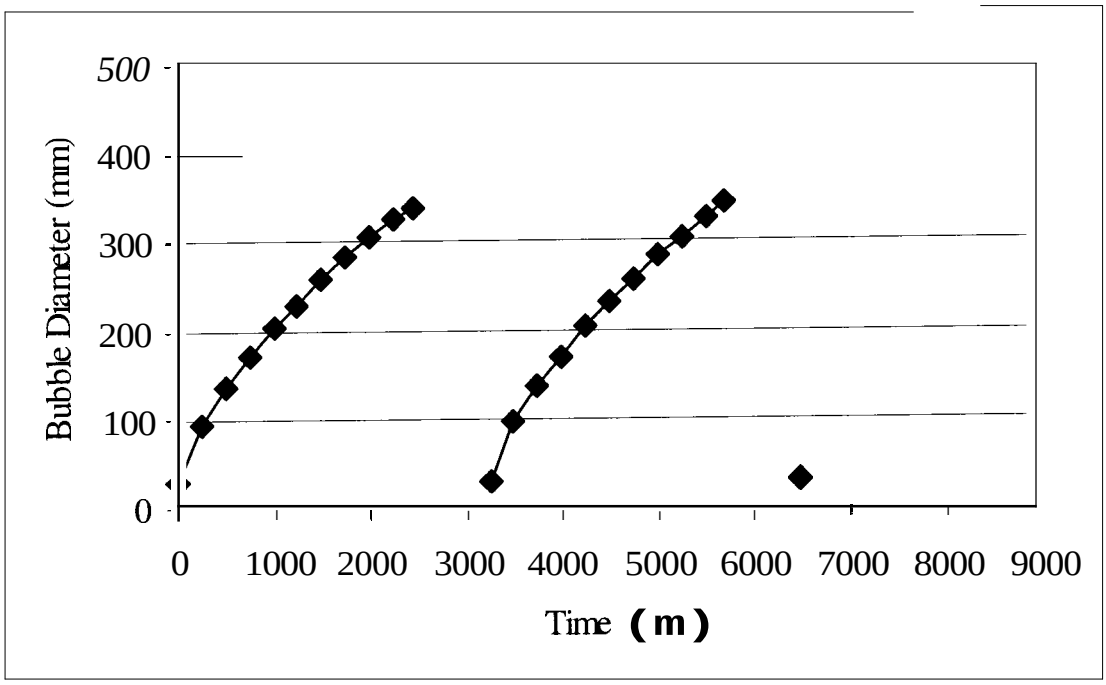

Figure 3-10. Bubble diameter versus time plot for Trial #8 in Appendix B (reactivated 10 days later).

4. Design and Construction of the Experimental Apparatus

4.1 Design Constraints

In order to conduct experiments involving bubbles in supersaturated solutions in a more systematic and controlled fashion, without relying on commercially available carbonated beverages, a new experimental device had to be designed and constructed. **A** custom designed apparatus should be re-useable, have a flat viewing window, produce bubbles only at one known location, allow for a greater range of achievable supersaturation levels, and provide accurate pressure readings. These features would make a custom designed apparatus advantageous for experimental work.

It was desired to have a 316 L stainless steel pressure vessel that could withstand pressures as high as 1500 psig. The inside surfaces of the vessel would need to be smooth, so as to limit the formation of interfering bubbles on the inside surfaces of the cell. **A** smooth flat viewing window would have to be fit into the side of the pressure vessel, allowing the contents of the cell to be viewed from the outside. The window size needed to be sufficient to permit viewing with both a Makro-Kilar Zoomar lens (Zoomar, Munich, Germany) and an UltraZoom 6000 II variable scope (Navitar, Inc., Rochester, NY) with a 10X Mitutoyo objective lens supplied by Navitar. The ability to use both of these lenses would provide a useful range for magnification and lighting requirements.

4.2 Required Equipment Items

Equipment items required for the construction of the experimental apparatus were acquired. A list of the major items needed follows:

(1) 1 stainless steel block
(2) 2 sapphire windows
(3) 2 pressure regulators
(4) 1 magnetic stirrer with stir bar
(5) 1 safety rupture disc
(6) 1 stainless steel base plate
(7) 2 gas collection tubes
(8) 5-gallon pail
(9) **SS** and flexible hose tubing
(10) high pressure fittings and valves

A 316 L stainless steel block measuring 7.6 cm x 11.4 cm x 22.9 cm was obtained from Alliant Metals, Inc. (Hempstead, NH). **A** pressure vessel with a removable lid and space for 1-2 windows was to be machined from this block.

Two sapphire windows, easily the most expensive of the aforementioned equipment items, were purchased from Saphikon (Milford, NH). Sapphire is capable of withstanding very high pressures without having to be excessively thick. In order to accommodate the 10X Mitutoyo objective lens, a circular window with a 40 mm diameter view would be required. The sapphire windows obtained were circular disks 70 mm in diameter and 6.35 mm thick. This size window would safely withstand pressures as high as 2000 psi with only a 0.0005" defection at the center of the window. Both faces were polished and the edges ground by the manufacturer

Two interchangeable pressure regulators were obtained. The regulators would need to be able to control the addition of compressed gases from storage cylinders to pressurize the contents of the test cell. Both regulators were suitable for supply pressures

of 2200 psig. A high-pressure air regulator (Matheson Gas Products, Montgomeryville, PA) was capable of discharging air or inert gases at pressures as high as 1500 psig. A low-pressure CO_2 regulator (N.H. Bragg and Sons, Bangor, **ME)** was also available for discharging CO_2 at pressures as high as 75 psig.

A Magnestir magnetic stirrer (Lab-Line Instruments, Inc., Melrose Park, IL) was adopted for use in the apparatus. The stirrer would be used to rotate a magnetic stir bar placed inside the pressurized test cell, which would rest directly above the stirrer. A glass encased stir bar (Fisher Scientific, Springfield, NJ) 33 mm long and 11 mm in diameter was to be used because it was believed that a smooth glass surface would prohibit bubble formation.

A safety rupture disk (High Pressure Equipment Company, Erie, PA) was ordered to prevent over-pressurization of the cell. If pressures inside the cell were to accidentally exceed 2000 psig, the rupture disk would fracture and depressurize the cell. This prevents the windows from being the weakest structural point in the test cell.

A stainless steel base plate **4** cm x 20 cm **X** 60 cm was available. This plate would serve as a solid support base for the magnetic stir bar and test cell assembly. An x-y-z stage supporting the camera could also be attached to this base plate.

Two gas collection tubes were found to collect the gases evolving from the supersaturated solutions. One tube was made of glass and had 0.1 cm markings. A 1.0 cm height difference on this tube corresponded to a volume of 19.635 mL. The other tube, furbished from a plastic 2-L graduated cylinder had a higher capacity. These tubes were to be used in conjunction with a 5-gallon pail to comprise the gas collection system.

High-pressure tubing (High Pressure Equipment Company, Erie, PA) was obtained for connecting the pressurized gas supply and the gas collection system to the test cell. Stainless steel tubing 1/8" in diameter was employed. Tygon® tubing (Fisher Scientific, Springfield, NJ) 6 mm in diameter was chosen as a flexible hose tubing to send discharged gases to the laboratory fume hood.

All of the necessary fittings and a hand valve for depressurizing the cell were made of stainless steel ordered from the High Pressure Equipment Company (Erie, PA). A separate three-way valve was also ordered from the McMaster Carr Supply Company (New Brunswick, NJ). The fittings and valves were sized for 1/8" stainless steel taper seal tubing.

4.3 Construction

The most challenging aspect of the construction of the intended experimental apparatus was the fabrication of the pressurized test cell. The original stainless steel block was first machined to a slightly smaller size while making the sides parallel to each other. This reduced the dimensions of the block to 7.4 cm x 11.1 cm x 19.3 cm.

Before any more cuts were made in the block, Lamé's equation [Ryffel (1984)] was used to calculate the minimum wall thickness for the pressurized test cell. With a circular view window that was to be 40 mm in diameter, the central core of the test cell was designed to have a slightly larger diameter of 42 mm. Using a stainless steel tensile estimate of 75,000 psi, a safety factor of 4, an inside circular diameter of 42 mm, and a pressure of 2200 psi (the maximum pressure that the test cell could be accidentally pressurized to), Lamé's equation predicts that the wall thickness needs to be at least 2.63 mm. From this analysis, it was decided that a minimum wall thickness of 4 mm would be maintained throughout the design.

A removable lid for the test cell measuring 7.4 cm **x** 11.1 cm x 2.7 cm was then cut away from the block, leaving a main body measuring 7.4 cm x 11.1 cm x 16.6 cm. Standing the main body upright with the longest dimension oriented vertically, a cylindrical hole 42 mm in diameter and 15.2 cm deep was bored through the top center of this main body. Extra care was taken to get a very smooth polish on the walls and bottom of this cut as this was to be the internal cavity of the test cell.

It was decided that only one of the sapphire windows would be installed. **A** frontal lighting technique through this solitary window was considered to be sufficient. The second window would be retained as a spare with the option to later install the other

window on the opposite backside if it was deemed necessary. One of the 11.1 cm x 16.6 cm faces of the main body was chosen to be the side that the window would be installed. A 40 mm diameter bore centered 8.3 cm down from the top of the main body was made through to the central core. A concentric bore of 70 mm diameter was next made for the 70 mm diameter sapphire window to rest in. This bore was made to a depth such that the inside surface of the window would be **4** mm out from the original edge of the central core (recall the **4** mm minimum thickness requirement). **A** separate stainless steel cylinder was found to cut out a holder for the window. A circular support ring with a 10.1 cm diameter and 40 mm central hole was made from this cylinder to hold the window in place. When positioned against the face of the test cell, this circular support ring had a visible thickness of 1.5 cm. Copper foil (MSC Industrial Supply Company, Plainview, NY) was used to line the steel surfaces that would contact and support the sapphire window, helping to form an airtight seal when the circular support ring was fixed into place. The support ring was attached to the face of the test cell with six groups of four Belleville Flange Spring Washers (McMaster Carr Supply Company, New Brunswick, NJ) bolted around the sapphire window.

Additional holes with 1/8" diameter were made in the main body of the test cell through to the central core in order to accommodate a line to allow pressurized gases to flow either into or out of the cell as well as a line containing the safety rupture disc. On the backside opposite the window, a hole for the line of pressurized gases that would flow into or out of the cell was centered 1.6 cm down from the top of the main body. When looking at the face containing the window head-on, the side to the left was chosen as the

location for the safety rupture disc. The line containing the safety rupture disc was centered 3.8 cm down from the top of the main body.

Groves were next machined in both the lid and the top of the main body of the test cell to accommodate a 5.3 cm diameter and 3 mm thick rubber 0-Ring (McMaster Carr Supply Company, New Brunswick, NJ). The 0-Ring would provide an airtight seal when the lid was bolted down with six 4.6 cm long and 0.9 cm thick bolts. **A** Swagelok® fitting (McMaster Carr Supply Company, New Brunswick, NJ) was added to the inside of the lid so that 4 mm diameter glass rods can be suspended from the lid. The glass rods were used to suspend objects under study so that they could be viewed through the sapphire window. The Swagelok® fitting was positioned 5 mm off-center closer to the side of the test cell containing the window. This was done because of the short focus distance of one of the camera lenses to be used with this system.

The Zoomar lens system had **a** focus distance of 14 cm while the Navitar lens system had a focus distance of only 3.3 cm. It was therefore optimum to place the magnetic stirrer 22 cm from one end of the base plate. The main body of the test cell would be attached to the magnetic stirrer. Both camera lens systems could then be attached to the **x-y-z** stage at the opposite end of the base plate and have appropriate focus distances for viewing into the cell. The cameras were hooked up to a 23" Zenith television and the images could be recorded with a 6-Head Toshiba VCR.

The 1/8" stainless steel tubing was then used to connect the pressure regulator, fittings, valves, and gas collection system in various configurations. The final set-up will be described in the following section.

4.4 Final Setup

The final setup for the experimental apparatus appears in Figure **4-1.** With the hand valve closed, the compressed gas could be released into the test cell, pressurizing the contents to levels as high as 100 atm. **A** magnetic stir bar inside the test cell could then be activated to aid in the saturation of the water inside the cell with the gas. After saturating the water for some pre-determined time, the magnetic stir bar was deactivated and the cylinder valve was closed. The system could then be depressurized by opening the hand valve and allowing the pressurized gases in the air space to be discharged from the cell through the three-way valve and into a nearby chemical fume hood. Once the pressure inside the cell reaches **1** atm, the three-way valve is switched so that any further gas released will be captured by the gas collection system. The dissolved gases released during an experiment are continually collected. At the conclusion of an experiment, re-activating the stir bar eliminates all remaining dissolved gases contributing to the supersaturation of the solution.

The gas collection system consisted of one of the gas collection tubes used in conjunction with the 5-gallon pail. Tygon® tubing was used to send gases from the discharge side of the three-way valve to the gas collection system. The gas collection tubes each had a small hole on one end allowing the tubing to be threaded through. The threaded Tygon® tubing was sealed around the hole perimeter with poster putty. The other end of the tube was completely open. Approximately **3-4** gallons of water were next added to the pail. While pinching the Tygon® tubing, water was added to the tube to within **1-2** cm of being completely full. The open end was then covered with a hand, inverted, and submerged below the water level in the pail. The hand was then removed

and the gas collection tube was allowed to rest in a holder over the 5-gallon pail. The gas collection tube would then collect gases by water displacement so that the dissolved gas quantities could be determined. Volume changes in the gas collection tube correspond to the volume of dissolved gas released from the solution.

Pictures of the experimental apparatus appear in Figures 4-2 and 4-3. Figure **4-2** shows the experimental apparatus without the gas collection system. To the right of the magnetic stir bar and test cell assembly is a vertical steel bar that supports the hand valve. Figure **4-3** is a close-up view of the outside of the test cell.

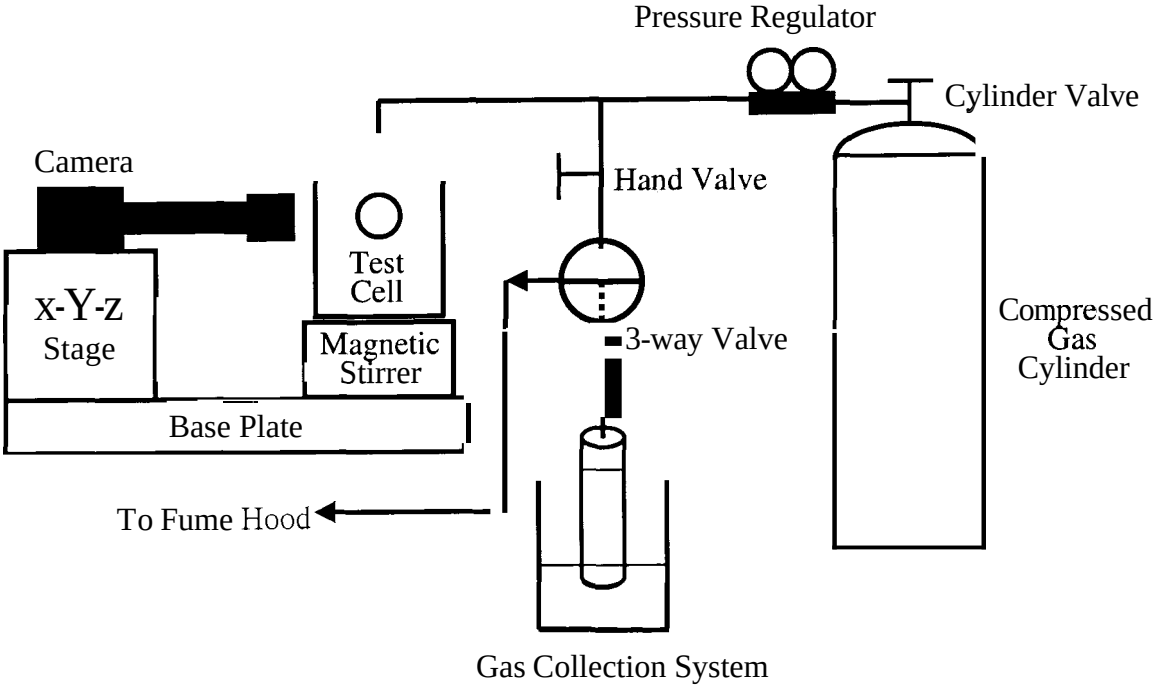

Figure 4-1. Experimental Apparatus (final setup).

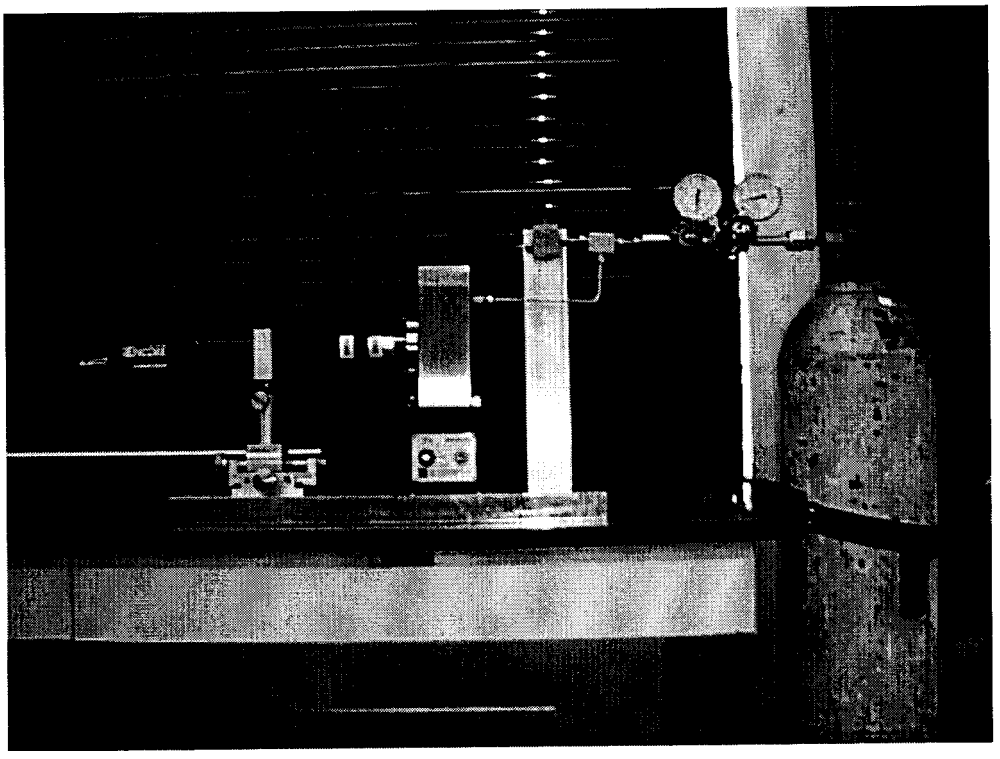

Figure 4-2. Photograph of the experimental apparatus (gas collection system not shown).

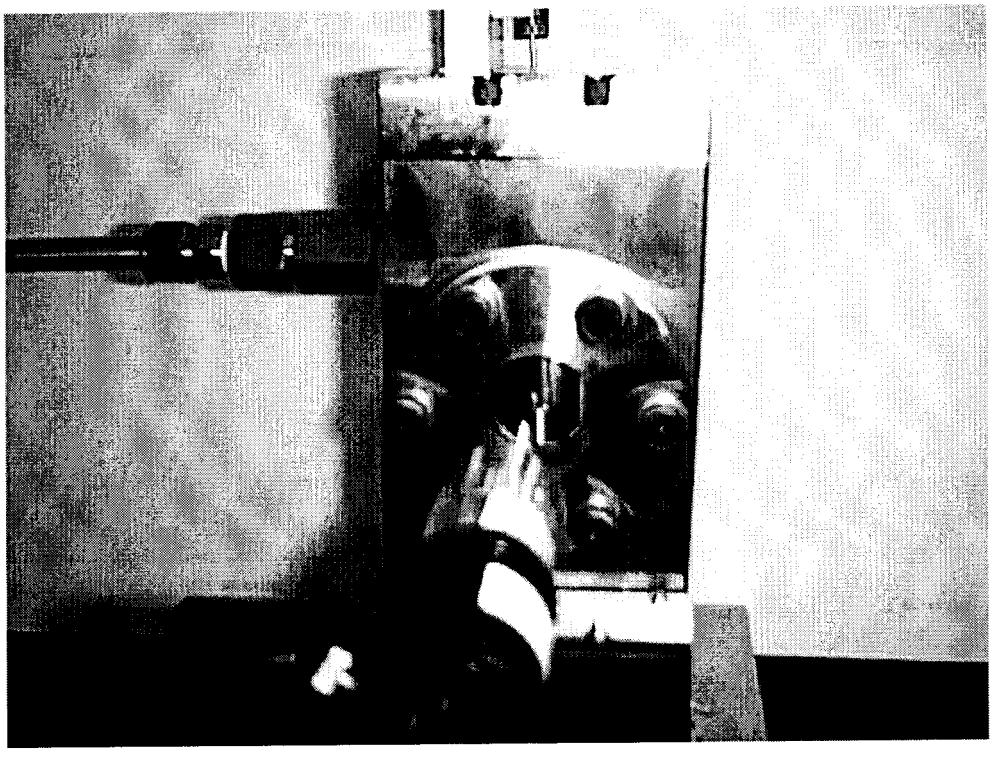

Figure 4-3. Photograph of the test cell facing the side with the sapphire window.

5. Experimental Procedures

5.1 Initial Testing

The initial testing described throughout §5.1 includes both the procedures and results of these first investigations. Both the procedures and the results are described here because they were instrumental in developing some of the later more established procedures.

5.1.1 Nothing Suspended in the Test Cell

The initial tests performed using the experimental apparatus involved the use of distilled water and compressed air [Portland Welding Supply, Portland, **ME]** with no objects suspended from the lid of the test cell. The internal test cell volume was determined to be approximately 200 mL. With the test cell initially dry and clean, 140 mL of distilled water was added to it along with a glass encased magnetic stir bar. Saturation efficiencies would be higher when the test cell was not completely filled with water due to the improved mixing that could be achieved under these conditions. The lid was then bolted into place and the system was pressurized to levels as high as 1400 psig.

Figure 5-1 shows the depressurization characteristics of the device. This plot was created by using an Encore MAC™ High-speed Video Camera (Olympus America Inc., Melville, NY) to record the pressure gauge on the discharge side of the pressure regulator during a depressurization event. Initially, the system was pressurized at 1400 psig. At $t = 0$, the system was depressurized and the final pressure of 0 psig was reached in less than four seconds.

Tests were next performed to test the device's ability to saturate water with air. With the system under 1400 psig pressure, the magnetic stir bar was activated to help air dissolve into the water. The magnetic stirrer had speed settings ranging from 0 to 7. Magnetic stirrer settings above 4.5 often led *to* the stir bar becoming unbalanced, so the speed was kept constant at a setting of 3.5. After five minutes of mixing under pressure, many bubbles would be observed to form throughout the test cell upon depressurization with the stirrer still activated; however, bubbles did not form throughout the test cell upon depressurization when the stir bar was deactivated. Some bubble formation was observed to occur from the bottom of the cell (even when the stir bar was deactivated before depressurization). A circular glass plate, measuring 38 mm in diameter and 3 mm thick, was inserted below the stir bar at the bottom of the test cell to minimize bubble formation.

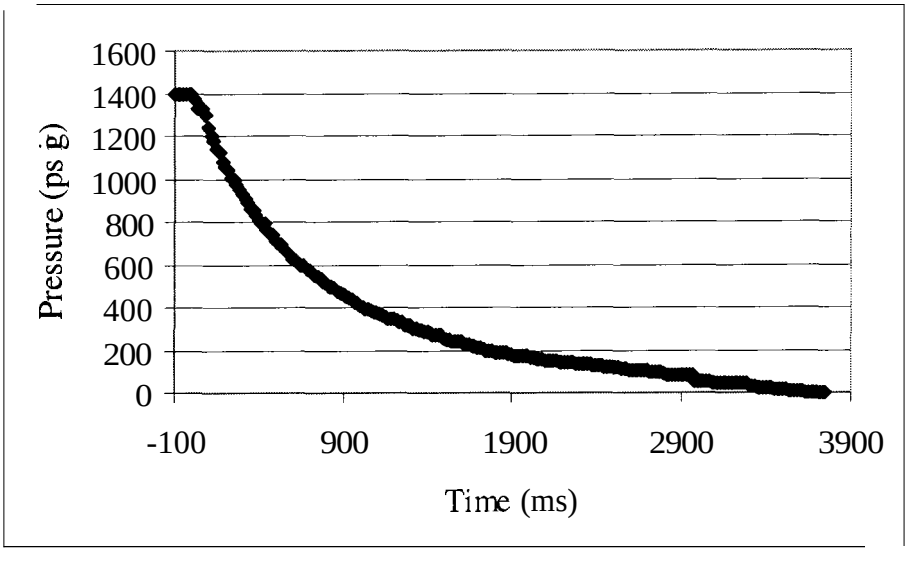

Figure 5-1. Pressure inside the test cell as a function of time following depressurization at t = 0.

Water was next mixed with air at 1400 psig in the test cell for saturation times of 5, 10, 15, 20, 25, and 30 minutes resulting in supersaturation ratios of 16.3, 26.4, 42.2, 57.4, 72.2, and 81.2, respectively. Bubble formation was not observed to occur on the smooth stainless steel walls of the test cell for the first four supersaturation ratios upon depressurization with the stir bar deactivated. The two highest supersaturation ratios resulted in massive bubble formation throughout the entire bulk solution. These results indicated that the test cell would be suitable for experiments with air in water supersaturations less than 57.4.

5.1.2 Smooth Suspended Substrates in Test Cell

Experiments continued with substrates submerged below the water line, attached to smooth glass rods suspended from the lid of the test cell. The first suspended substrates tested included glass, stainless steel, and Teflon. The glass and stainless steel surfaces were hydrophilic while the Teflon provided a hydrophobic sample. Glass rods measuring 4 mm in diameter and cut to a length of 8 cm were used to suspend the various substrates. Substrates were attached to the glass rods using a Conap Easypoxy® Kit (The Smith Group, Inc., Warminster, PA). No bubble formation originated on any of these substrate surfaces for supersaturations less than 50.

The sequence of photographs in Figure 5-2 shows an interesting observation that was made on a Teflon sample. These images were obtained using an XC-75 CCD camera (Sony, San Diego, CA), a Makro-Kilar Zoomar lens (Zoomar, Munich, Germany), and a Series 180 Fiber-Lite System with gooseneck attachments (Dolan-Jenner Industries, Lawrence, MA) for frontal lighting. A strip of Teflon measuring 2 mm

in thickness was suspended in a water sample supersaturated with air at a supersaturation ratio of 15.7. Initially no bubbles formed on the Teflon surface upon depressurization. Approximately one minute later, a bubble originating from the bottom of the test cell rose upwards and swept along the Teflon surface. This bubble deposited parts of itself behind, which in turned grew due to the remaining supersaturation in the surrounding solution. These photographs illustrate the importance of pre-existing gas in allowing bubble formation to occur from surfaces in contact with supersaturated solutions.

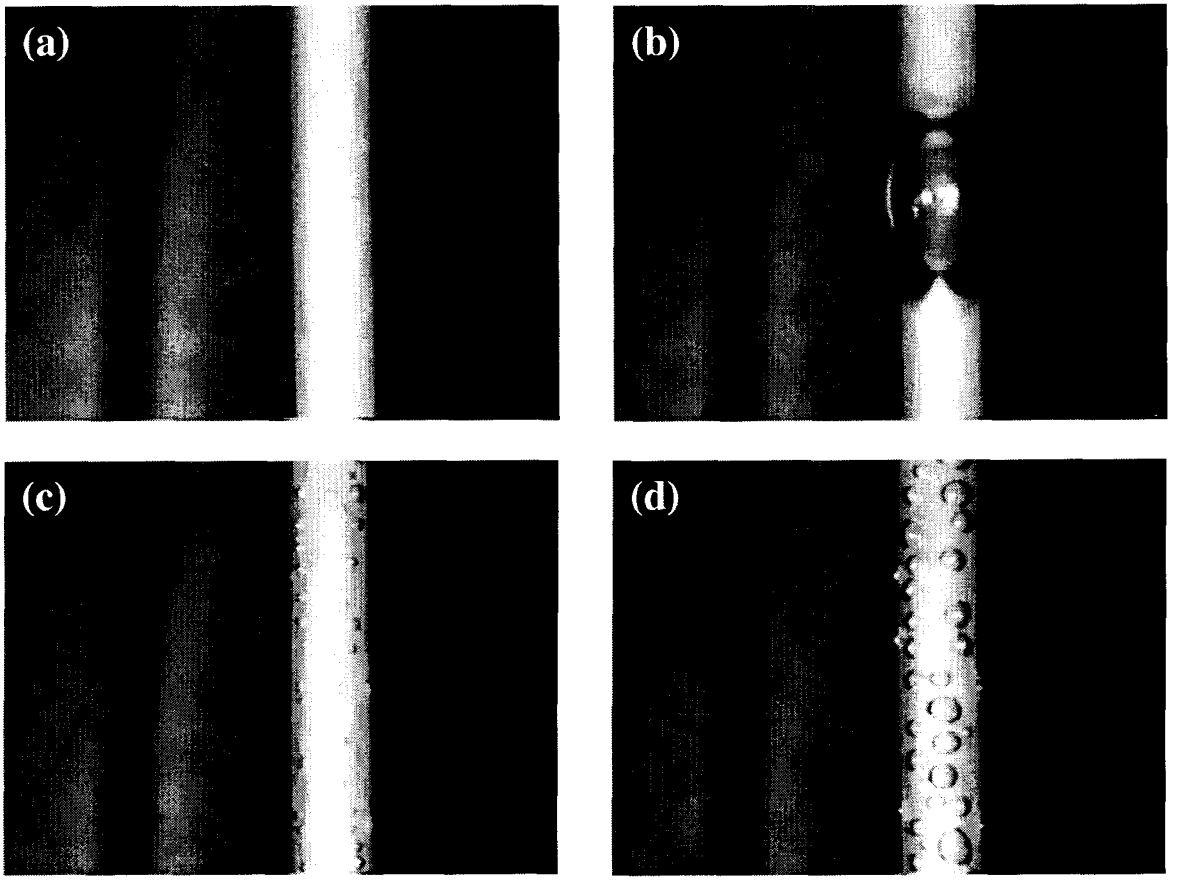

Figure 5-2. Sequence of photographs showing the edge of a Teflon strip suspended in water supersaturated with air at a supersaturation ratio of 15.7: (a) no bubble formation is observed on the Teflon strip immediately after depressurization, (b) one minute later, a bubble rising from the bottom of the test cell sweeps against the Teflon surface, (c) the bubble leaves parts or remnants of itself behind, and (d) these remnants continue to grow in the supersaturated solution.

5.1.3 Wax Substrates Suspended in Test Cell

Paraffin and polyethylene wax samples (Reed Wax, Reading, MA) were next used to further investigate bubble formation on suspended substrates. Bubble formation was observed to occur on these surfaces before massive cavitation occurred throughout the bulk solution. This suggests that the porous and hydrophobic nature of these wax surfaces enabled gases to be trapped. Under sufficient supersaturation levels, bubbles would then appear to form and grow on these surfaces. Larger cavities in the wax surface are less likely to trap gases, but more readily form bubbles when gases are trapped inside [Jones *et al.* (1998)]. Also, smaller cavities would be more likely to trap the gases, but would require higher supersaturation levels to allow the bubbles to form and grow.

Four distinct paraffin wax surfaces were then prepared to determine the threshold supersaturation levels at which bubble formation would be first observed. The four paraffin wax surfaces were: smooth paraffin wax, rough paraffin wax, smooth plasma treated paraffin, and rough plasma treated paraffin. The wax was first completely melted and then poured into a mold where it was allowed to cool. The top surface visually appeared smooth upon cooling (although examination with a microscope indicated that there was still some micro-roughness present). The cooled surface could be made rough by using an X-ACTO™ knife (Hunt Corporation, Boston, MA) to scrape away the top layer of paraffin. Plasma treatments were performed to make the wax more hydrophilic.

Wax was treated with plasma using a Hummer **VI-A** Sputtering System (Anatech Limited, Springfield, VA). Wax samples measuring 1 cm x 1cm x 4 mm were epoxy-bonded to glass rods and exposed to plasma for 20 seconds. Air at an absolute pressure of 160 millitorr was maintained in the treatment chamber. The AC voltage was adjusted

from four to six volts to maintain a current of 35 mA during the 20 second treatment phase. Functional groups containing oxygen and nitrogen atoms from the air become deposited on the wax surface, making it more hydrophilic. Contact angles on the untreated paraffin ranged from 90 to 100º, while plasma treated paraffin samples had contact angles ranging from 15 to 30".

Figure 5-3 displays the results of threshold testing performed on the four distinct paraffin wax surfaces. The wax samples were suspended inside the test cell of the experimental apparatus, pressurized to 1400 psig and saturated for times ranging from 1 minute to 80 minutes to create solutions with different levels of supersaturation. The rough paraffin wax first produced bubbles at the lowest supersaturation ratio, which was 2.1. The bubble formation at such a low supersaturation level indicates the effectiveness that this surface exhibited in trapping gases and then forming bubbles upon depressurization. The rough plasma treated paraffin first produced bubbles at the next highest supersaturation ratio of 15.6. Making a rough surface more hydrophilic does make it somewhat less favorable for trapping gases. The threshold supersaturation for the smooth paraffin wax was **43.8.** At the supersaturation threshold of 77.5 for the smooth plasma treated paraffin, bubble formation was first observed on both the surface of the wax as well as uniformly throughout the bulk solution. These results indicate that surface roughness features are more important than the hydrophilic/hydrophobic nature of the surface in determining whether or not a surface can trap gases and then later release these gases upon depressurization in contact with a supersaturated solution.

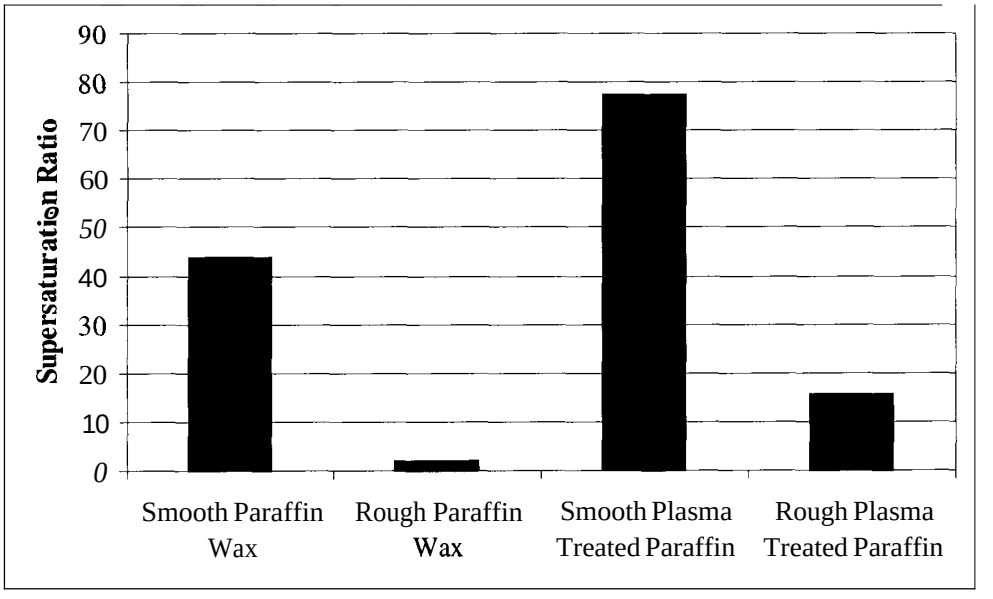

Figure 5-3. Supersaturation ratios at which bubble formation first occurs on the four paraffin wax surfaces suspended in water-air solutions.

5.2 Capillary Preparation

Based on the initial experiments described in §5.1, it was decided that more controlled and systematic experiments could be performed if sites could be prepared that would produce bubbles only at one known location. Artificial Harvey Nuclei, similar to the artificial sites of Buehl and Westwater (1966) and Bisperink and Prins (1994) would be prepared from capillary pipettes (VWR Scientific, West Chester, **PA)** and gas chromatograph (GC) capillary tubing (Chromatography Research Supply, Louisville, KY).

The first sites were made from the tips of the capillary pipettes. The inside diameter of these pipette tips measured 1320 μm. The first 1 cm of the pipette tip was scored with the X-ACTO™ knife. This 1 cm length was then snapped off using a pair of tweezers. The rough cut end was then heated with a Bunsen burner and rotated in the flame until the rough cut end melted and fused together, sealing this end.

Smaller capillaries were prepared using the GC capillary tubing. Fused silica tubing with inside diameters of 50, 200, and 450 μm were obtained. This GC capillary tubing arrived in 1 m coils that had to be cut down to 1 cm lengths. Scotch@tape (3M, Saint Paul, MN) was wrapped around the GC capillary tubing three times on both sides of the desired cut. The tubing was then scored with the X-ACTO™ knife and snapped. The tape was then peeled off and the cut GC tubing was examined under a Bausch & Lomb microscope (Rochester, NY) with 4X, 10X, 40X, and 100X objectives. One in approximately every six cuts was smooth, clean, and thus considered to be acceptable. The smoothly cut GC capillary tubing was then placed under a Bunsen burner flame to burn off a strength and flexibility coating on the outside wall of the tubing. The fused

silica tubing did not melt under the Bunsen burner flame, but the exterior coating melted away, leaving a clear capillary to be used as a Harvey Nuclei site in future experimentation.

The glass rods used for suspending these capillaries inside the test cell were cut to 10 cm lengths. Shorter glass rod segments, measuring 2 cm long were cut and epoxy-bonded parallel to the last 2 cm of length on the 10 cm rods. Both types of prepared capillaries were then epoxy-bonded parallel to the rod so that half the length of the capillary extended beyond the top edge of the 2 cm glass rod segments. Care was taken to ensure that the bottom end of the capillary was completely covered with the epoxy to ensure an air-tight seal. The 2 cm glass rod segments helped separate the bubbles growing from the capillary from the vertical glass support rod.

A glass support shield was then epoxy-bonded onto the end of the glass rod-capillary assembly. Glass beakers with a capacity of 5 mL, designed for use with a Beckman pH meter (National Technical Laboratories, South Pasadena, **CA),** served as the supporting shield. The support shield prevented any rising bubbles originating from the bottom of the test cell from interfering with bubbles growing on the capillary.

A schematic showing the inside view of the test cell with an artificial capillary suspended from **a** glass rod appears in Figure **5-4.** The capillary is positioned so that it is submerged below the water line and can be viewed through the sapphire window. This arrangement was used for all artificial capillary experiments.

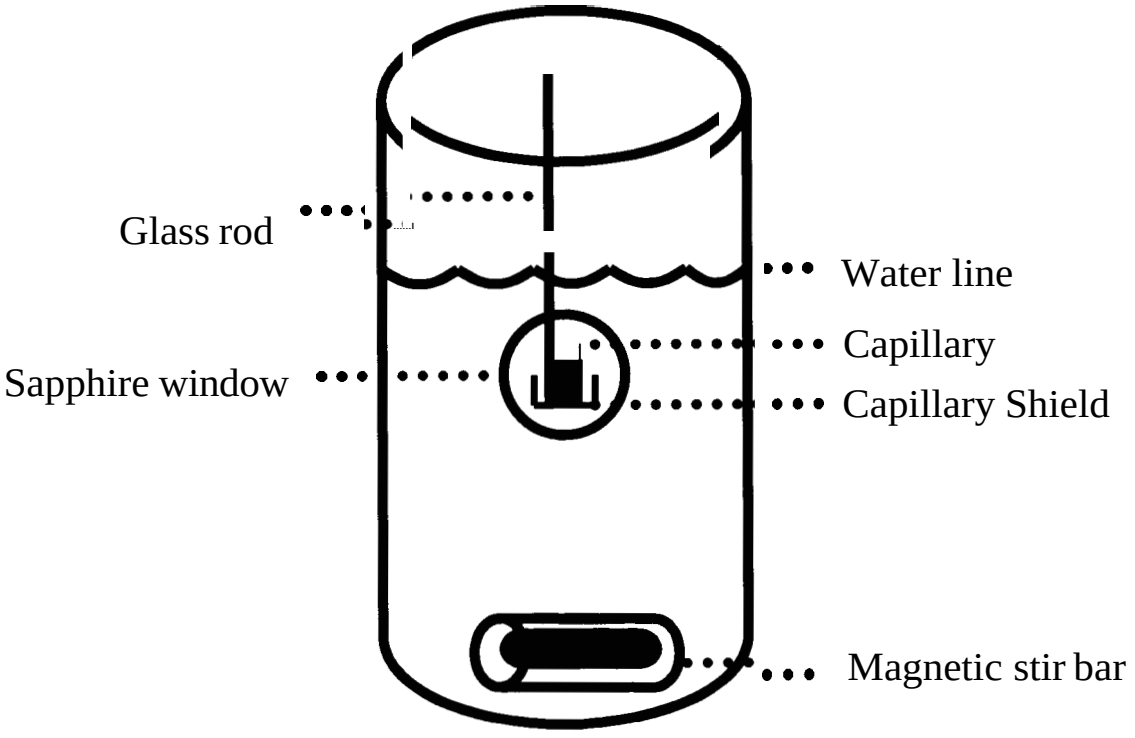

Figure 5-4. Schematic showing the inside view of the test cell with an artificial capillary suspended from a glass rod.

5.3 Capillary Experiments

Using the artificial capillaries with the setup displayed in Figure 5-4, bubbles did not form upon depressurization in a supersaturated solution. It was necessary to seed these capillaries with some pre-existing gas in order to make them active bubble production sites. Artificial capillaries seeded with a gas would behave similar to Harvey Nuclei containing some pre-existing gas.

To seed an artificial capillary with a gas bubble, first 190 mL of distilled water is added to the test cell along with a glass-encased magnetic stir bar. A glass rod with a capillary and capillary shield assembly is attached to the inside lid of the test cell. The lid is then positioned so that the capillary rests just below the water line inside the cell. A small glass syringe is then used to blow an air bubble onto the tip of the capillary. The bubble is then lowered to a position where, using a pipette, 50 mL of water can be removed from the cell. This results in a final water volume of **140** mL, which is optimum for mixing during saturation. After using the pipette, the lid is fully lowered and attached to the base of the test cell with an airtight seal.

When the test cell is pressurized, the attached bubble retreats into the capillary. The magnetic stir bar can then be activated to assist in the dissolving of gases into the water. After saturating the water under pressure, the stir bar is deactivated, and the system is depressurized. The air bubble that had retreated into the capillary now re-expands to its original volume and continues to grow because the surrounding liquid is now supersaturated with the dissolved gas. The bubble grows until the buoyancy force becomes large enough to cause it to detach from the capillary. A small part of the bubble

is left behind in the neck of the capillary upon detachment, and it continues to grow and forms the next bubble. Photographs illustrating this cycle of bubble production at an artificial capillary appear in Figure 5-5.

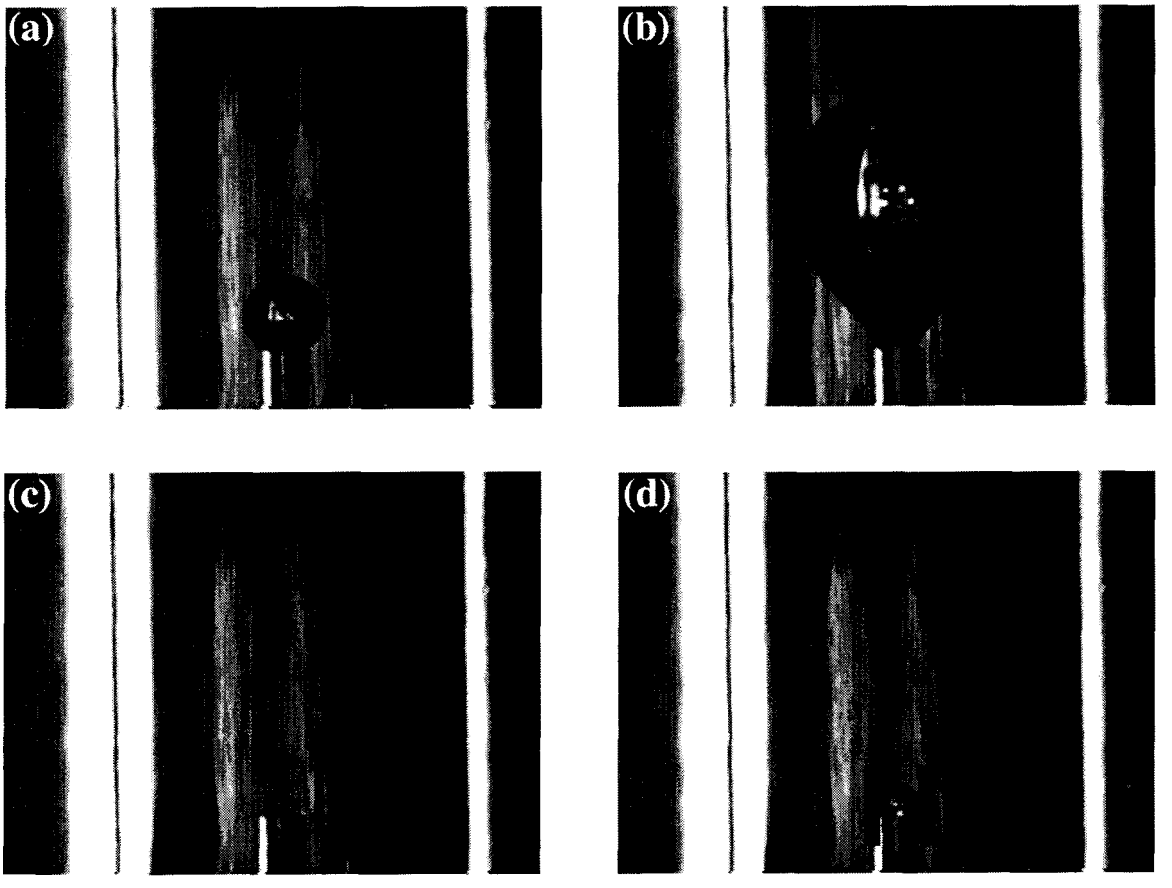

Figure 5-5. The cycle of bubble production at an artificial 450 μm ID capillary: (a) bubble added to the capillary with a syringe, (b) bubble just before detachment after pressurization, saturation, and depressurization, (c) small bubble cap is present at capillary opening immediately after detachment of previous bubble, and (d) bubble has grown to size larger than the opening of the capillary.

5.4 "Nucleation" Lapse Time Experiments

Earlier arguments, presented in §3.1, state that there is really no such thing as a "nucleation" lapse time for bubbles that exhibit a cyclical pattern of bubble production at specific sites. Additional supporting evidence appears in Figure 5-6. The high-speed video images in Figure 5-6, each taken 4 ms apart, clearly show a small circular bubble cap being left behind during the detachment of a full size bubble. This small bubble cap is not nucleated; it is simply part of the previous bubble left behind to continue the cycle of bubble production.

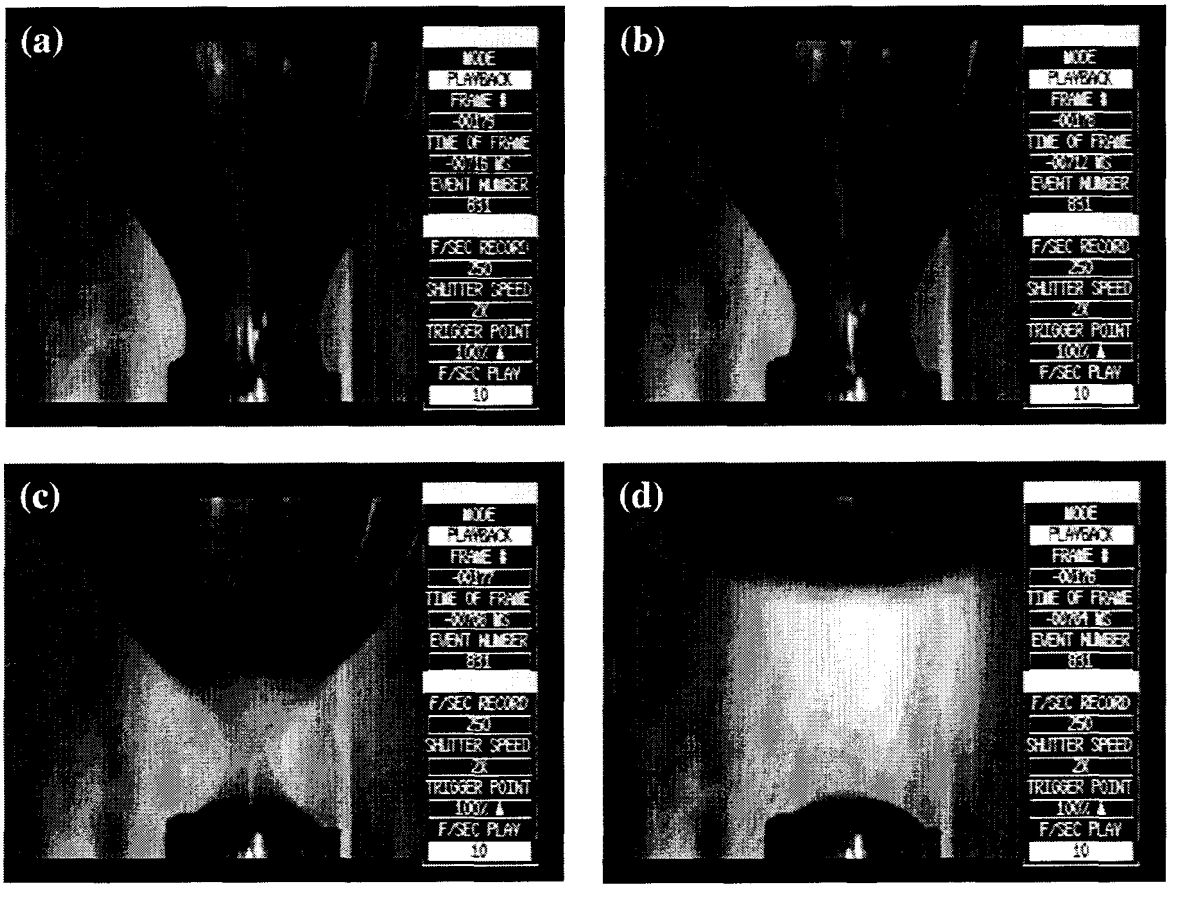

Figure 5-6. High-speed video sequence of a detachment event from a 450 μm ID capillary, showing that a small bubble cap is left behind by the previous bubble upon detachment.

Small bubble caps were only observed to form at the opening of a capillary immediately following detachment when the capillary opening was smooth and flat. For example, the behavior at a roughly cut capillary is presented in Figure 5-7. When the capillary opening is not smooth and flat, the bubble tends to shear away at a location inside the capillary instead of the location right at the capillary opening.

Regardless of whether the capillary opening was smooth and flat or rough and irregular, it was understandable that earlier researchers would have identified bubble production sites as having "nucleation" lapse times. When viewed from above, the presence of a bubble cap would not have been visible to earlier researchers. This bubble cap would not have been visible until the bubble had grown to a size larger than the opening of the bubble production site. For the purpose of comparison with earlier research, we will redefine the "nucleation" lapse time as the period of time between the detachment of one bubble and the point in time at which the next bubble has grown to a size larger than the site opening.

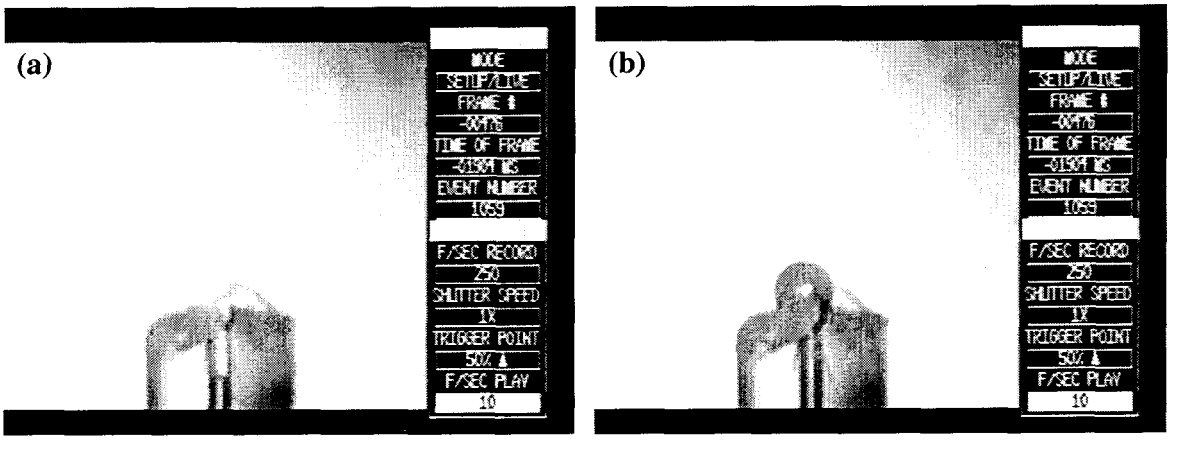

Figure 5-7. Behavior at a roughly cut 50 μm ID capillary following detachment: (a) following detachment, bubble cap is located 100-150 μm below the top of the capillary and (b) after a period of time, the bubble re-emerges from the capillary.

Experiments on smooth and flat cut 200,450, and 1320 μm ID capillaries were to be performed to determine "nucleation" lapse times. The water was saturated with air at 1400 psig for 10 minutes to produce solutions with supersaturation ratios ranging from 18-21. The time between the first bubble detachment and the point at which the bubble cap becomes larger than the capillary opening is recorded as the "nucleation" lapse time. These experiments were performed so that comparisons could be made with the soda bottle "nucleation" lapse time measurements reported in Figure 3-7.

5.5 Long Term Behavior at Artificial Capillaries

Using the XC-75 CCD camera, Makro-Kilar Zoomar lens, and the Series 180 Fiber-Lite System with gooseneck attachments to provide frontal lighting, the long term behavior of successive bubbles growing from artificial capillaries was investigated. "Nucleation" lapse times were dropped from further consideration, since they were determined to be an experimental artifact in that the bubble cap cannot be seen until it becomes larger than the capillary opening. Variables that were tracked for consecutive bubbles growing at the capillary were bubble detachment diameter, bubble growth time (defined as the time between detachments of successive bubbles), and the quantity of gas collected by the gas collection system.

Experiments involving a 450 μm ID capillary were performed using air at 1400 psig to saturate water for 5, 10, 25, and 40 minutes. One trial was also run with a 200 μm ID capillary at an air pressure of 1400 psig and a saturation time of 10 minutes. The long term behavior of bubbles growing from these capillaries was measured over 4-6 hour time periods.

5.6 First Full Bubble Only Experiments

For comparison with modeling results, it was determined to be advantageous to only examine the first full bubble only, growing from the capillary. This would be the bubble that forms after the very first detachment of the bubble that rapidly expands from the capillary upon depressurization. The same camera, lens, and lighting equipment described in §5.5 were also used in these experiments. Table 5-1 summarizes the First Full Bubble Only Experiments performed.

Table 5-1. List of First Full Bubble Only Experiments Performed.

Capillary ID	Saturating Gas	Saturation Pressure	Saturation Times
450 μm	air	1400 psig	2, 3, 10, 25, 40 min
450 μm (repeat)	air	1400 psig	2, 3, 10, 25, 40 min
200 μm	air	1400 psig	2, 3, 10, 25, 40 min
50 μm	air	1400 psig	2, 3, 10, 25, 40 min
450 μm	air	700 psig	4, 6, 20, 50, 80 min
50 μm	air	1400 to 72.5 psig	10, 25, 40 min
450 μm	carbon dioxide	75 psig	5, 10, 15, 20 min
450 μm	helium	1400 psig	1, 2, 3, 5, 7, 10 min

Distilled water was used for all of the First Full Bubble Only Experiments. Water temperature was not controlled, but it was measured and recorded for each trial. Additional helium experiments were conducted with temperature adjusted water to validate the temperature correction of diffusion coefficients that was performed when comparing the experimental results to the modeling predictions. Low temperatures were achieved by packing the outside of the test cell with ice, while high temperatures were achieved by strapping hot water bottles to the outside of the test cell.

Finally, the accuracy of bubble detachment diameter measurements was verified by analyzing the photograph in Figure 5-8. The bubble detachment diameter (D_{max}) of this bubble was determined by measuring the maximum horizontal distance across the bubble. For the bubble pictured in Figure 5-8, this value was 1816.9 pm. For comparative purposes, the area of the bubble was next measured and determined to be 1.0825×10^7 μm^2. This area was found by finding a best fitting equation to represent the surface position for one half-side of the bubble. The standard calculus formula for finding the area of a surface of revolution can then be applied. The equivalent spherical diameter for an area of 1.0825×10^7 μm^2 is 1856.3 μm. This represents only a 2.2% discrepancy when compared to the D_{max} value.

Figure *5-8.* Bubble at detachment size D_{max} attached to a 450 μm Capillary.

6. Experimental Results

This chapter presents experimental results obtained using the experimental apparatus with the more established procedures described in §5.3 - §5.6. Appendices D and E contain the raw data for the experimental results presented throughout §6. "Nucleation" lapse time measurements are reported in §6.1, the long term behavior at artificial capillaries is reviewed in §6.2, and the results from the first full bubble only experiments appear in §6.3. Finally, a discussion on the significance of these experimental findings is presented in §6.4.

6.1 "Nucleation" Lapse Time Experiments

"Nucleation" lapse time results for smooth and flat cut 200, 450, and 1320 μm ID capillaries suspended in air-water solutions with supersaturation ratios ranging from 18-21 appear in Figure 6-1. A small bubble cap appeared at the opening of each of these capillaries immediately upon detachment of a full size bubble. "Nucleation" lapse times were measured as the time necessary for the bubble cap to grow larger than the capillary opening when viewed from above. Referring to Figure 5-5, the amount of time between images (c) and (d) correspond to a "nucleation" lapse time.

The results in Figure 6-1 reveal that capillaries having larger inside diameters yield longer "nucleation" lapse times. Raw data used to construct Figure 6-1 appears in Appendix D.1. The 200,450, and 1320 μm ID capillaries had average "nucleation" lapse times of 11.10 ± 1.99, 29.51 ± 2.29, and 86.52 ± 9.83 s, respectively. Consequently, the larger diameter capillaries also resulted in bubbles with larger detachment diameters (D_{max} values). The 200, 450, and 1320 μm ID capillaries resulted in bubble detachment diameters of 1981.3, 2410.7, and 3100.7 μm, respectively.

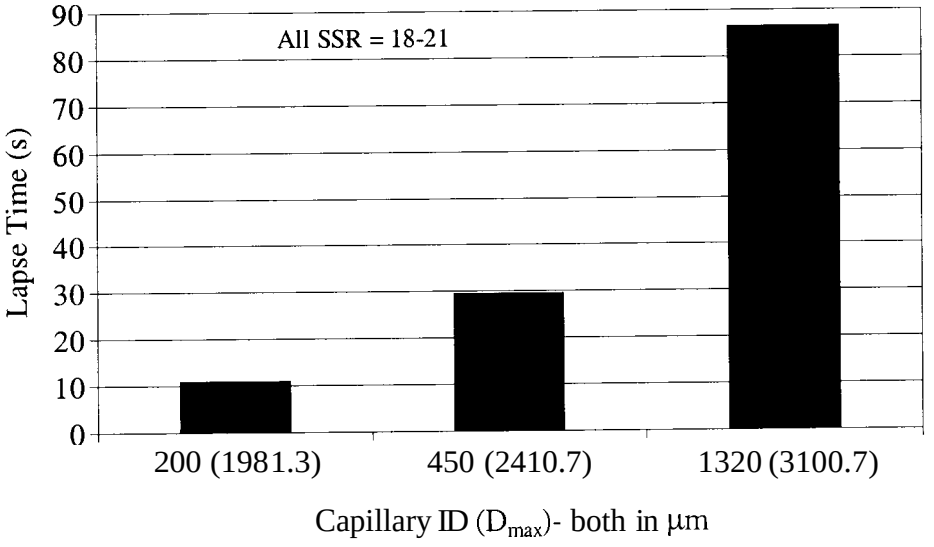

Figure 6-1. "Nucleation" lapse time measurements for three capillary sizes suspended in air-water solutions having supersaturation ratios ranging from 18-21.

6.2 Long Term Behavior at Artificial Capillaries

Figure 6-2 displays results on the long term behavior of a series of bubbles growing from a 450 μm capillary. Saturation was performed with air at a pressure of 1400 psig for 10 minutes. It was conducted at 20°C and resulted in an initial supersaturation ratio of 15.5. Figure 6-2 presents the bubble detachment diameters, bubble growth times, and dissolved gas concentrations for a series of bubbles over a six hour period. The results show very little variability in the bubble detachment diameter from bubble to bubble. The bubble growth times tend to increase as the dissolved gas concentration decreases over time. The same behavior was observed when this experiment was repeated using a 200 μm capillary, as indicated by Figure 6-3.

The long term behavior at a 450 μm capillary was revisited for three additional supersaturation ratios. Figure 6-4 shows that bubble detachment diameter was independent of the supersaturation ratio. When examining both the bubble growth time and dissolved gas concentration curves in Figure 6-4, a non-systematic trend in both of these curves was noted. The bubble growth times and dissolved gas concentration curves overlapped and crossed-over at certain locations. Because of this overlapping and cross-over in both bubble growth times and dissolved gas concentrations, it was decided that it was better to examine the growth characteristics of the first full bubble only when attempting to fit experimental data to bubble growth models.

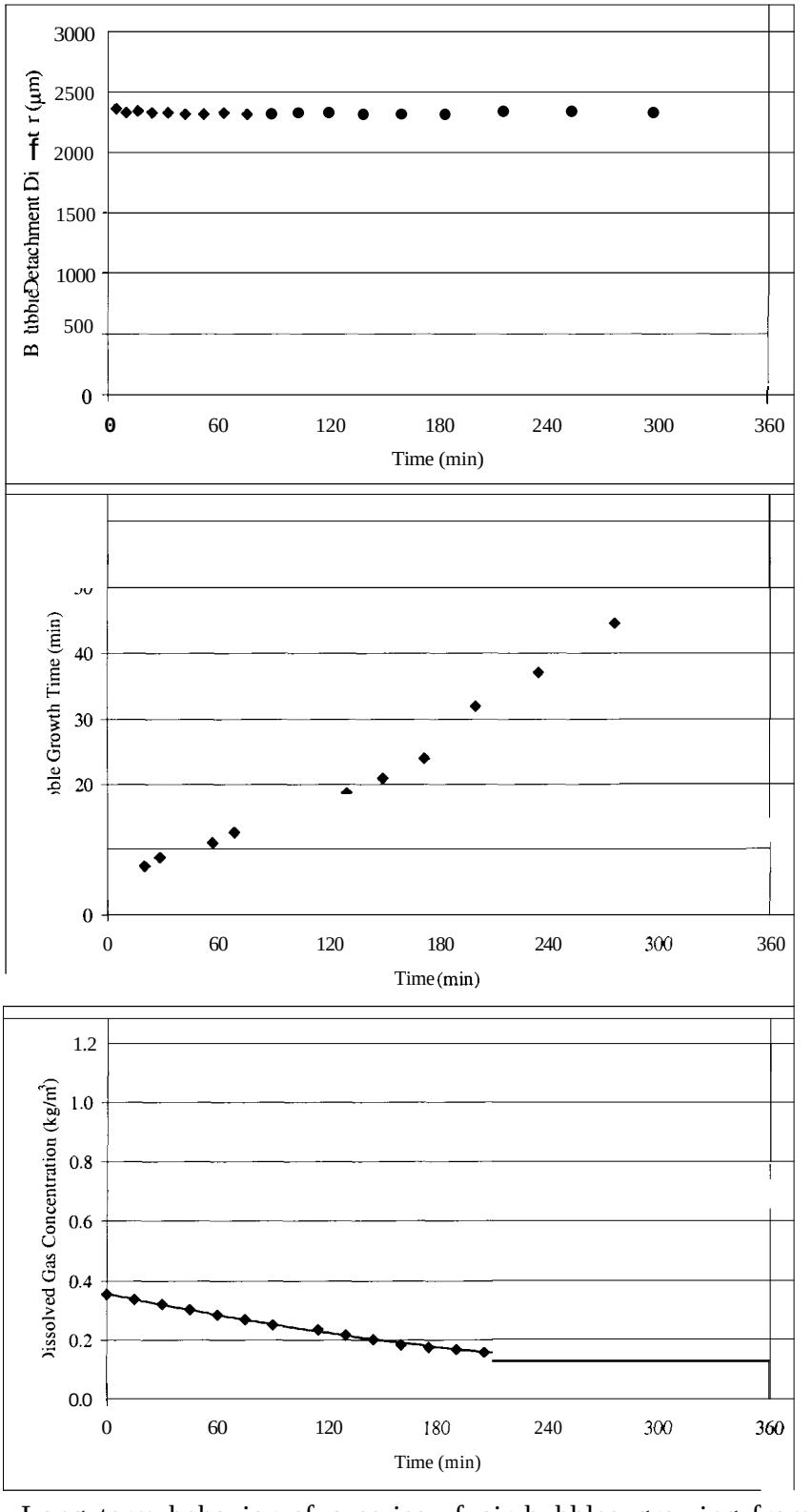

Figure 6-2. Long term behavior of a series of air bubbles growing from a 450 μm capillary suspended in water with an initial supersaturation ratio of 15.5. The three plots show the bubble detachment diameters, bubble growth times, and dissolved gas concentration since the moment of depressurization (time = 0 minutes).

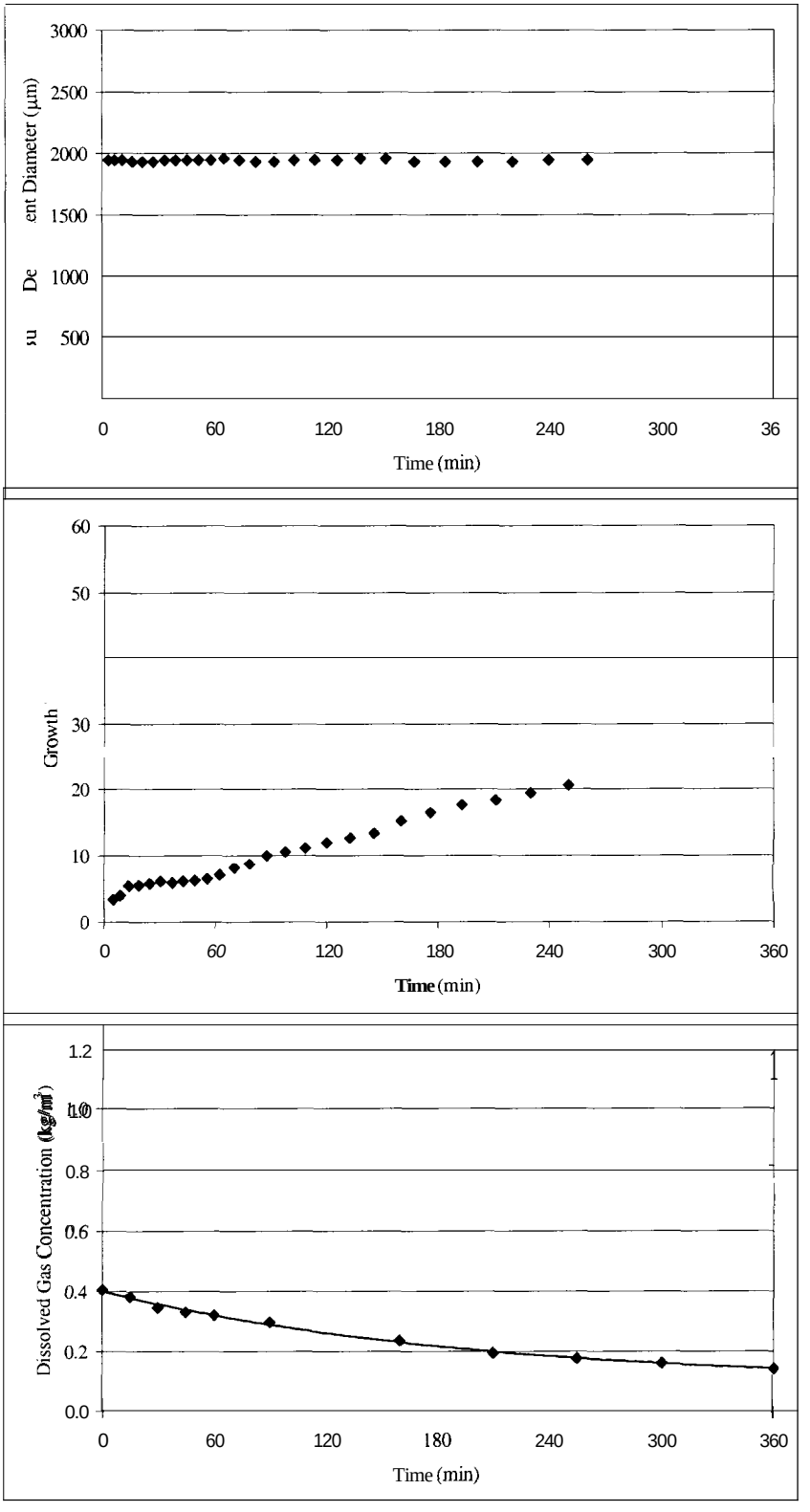

Figure 6-3. Long term behavior of a series of air bubbles growing from a 200 μm capillary suspended in water with an initial supersaturation ratio of 17.8. The three plots show the bubble detachment diameters, bubble growth times, and dissolved gas concentration since the moment of depressurization (time = 0 minutes).

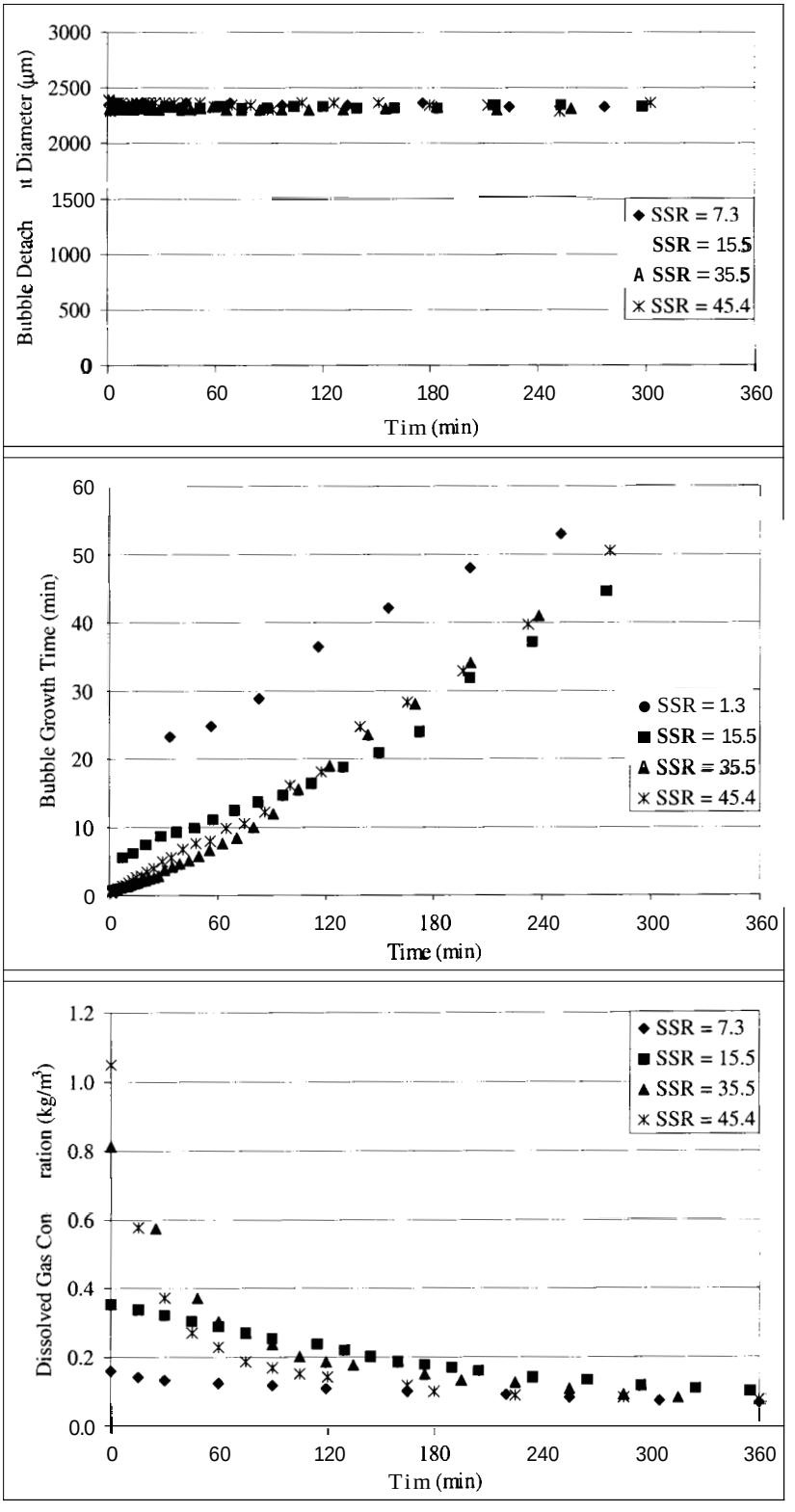

Figure 6-4. Long term behavior of a series of air bubbles growing from a 450 µm capillary suspended in water for four supersaturation ratios. The three plots show the bubble detachment diameters, bubble growth times, and dissolved gas concentration since the moment of depressurization (time = 0 minutes).

6.3 First Full Bubble Only Experiments

Raw data collected for all of the first full bubble only experiments appears in Appendix E. For each trial, the gas collection tube height difference ***(Ah)*** for the air and helium experiments or volume measurement for the carbon dioxide experiments are reported along with temperature, bubble detachment diameter (D_{max}), and bubble growth time (t_G). Five replicates were completed for each distinct set of conditions. The height difference or volume measurement is taken as the difference between the average reading during the first full bubble's existence and the reading after re-activating the stir bar to drive all remaining dissolved gases from the solution. The ***Ah*** and volume measurements in Appendix E are converted to supersaturation ratio *(SSR)* values based on the sample calculations of Appendix H.1. Temperatures tended to be higher for the larger supersaturation ratios because the longer mixing times supplied more mechanical energy to the test cell contents, thus elevating the temperature.

6.3.1 Air in water, 450 μm capillary

Table 6-1 displays the experimental results for trials involving a 450 μm capillary with air as the saturating gas. The water was saturated with air at 1400 psig for 2, 3, 10, 25, and 40 minutes yielding respective average supersaturation ratios of 4.5, 6.6, 16.1, 34.7, and 45.1. Bubble detachment diameter remained essentially unchanged while bubble growth times decreased with increasing supersaturation ratio.

SSR	T (ºC)	D_{max} (μm)	t_G (min)
4.5 ± 0.1	20.4 ± 0.5	2308.3 ± 5.4	55.36 ± 2.07
6.6 ± 0.2	20.4 ± 0.5	2327.8 ± 13.9	23.95 ± 0.58
16.1 ± 1.2	21.6 ± 1.1	2341.7 ± 22.1	4.95 ± 0.62
34.7 ± 1.1	24.2 ± 1.3	2338.9 ± 13.9	0.93 ± 0.08
45.1 ± 2.1	25.9 ± 1.7	2330.6 ± 10.2	0.38 ± 0.03

6.3.2 Air in water, 450 μm capillary (repeat)

Table 6-2 displays the experimental results for trials involving a 450 μm capillary with air as the saturating gas, under identical (repeat) conditions as the results presented in §6.3.1. The water was saturated with air at 1400 psig for 2, 3, 10, 25, and 40 minutes yielding respecting average supersaturation ratios of 4.6, 7.3, 18.7, 37.4, and 45.8. Bubble detachment diameter remained essentially unchanged while bubble growth times decreased with increasing supersaturation ratio.

Table 6-2. Experimental results for air in water, 450 μm capillary (repeat).

SSR	*T* (ºC)	D_{max} (μm)	t_G (min)
4.6 ± 0.1	21.1 ± 0.7	2350.0 ± 10.2	56.47 ± 1.92
7.3 ± 0.4	25.1 ± 1.6	2358.3 ± 20.0	22.05 ± 1.58
18.7 ± 0.6	26.5 ± 1.9	2347.2 ± 12.2	3.83 ± 0.34
37.4 ± 0.3	29.7 ± 0.4	2338.9 ± 6.7	0.79 ± 0.06
45.8 ± 2.8	28.5 ± 1.5	2361.1 ± 17.2	0.41 ± 0.07

6.3.3 Air in water, 200 μm capillary

Table 6-3 displays the experimental results for trials involving a 200 μm capillary with air as the saturating gas. The water was saturated with air at 1400 psig for 2, 3, 10, 25, and 40 minutes yielding respecting average supersaturation ratios of 4.1, 6.2, 15.3, 30.7, and 44.0. Bubble detachment diameter, although lower than the trials involving the 450 μm capillary, remained essentially unchanged while bubble growth times decreased with increasing supersaturation ratio.

SSR	*T* (ºC)	D_{max} (μm)	t_G (min)
4.1 k0.2	21.3 ± 0.9	1947.2± 10.2	44.10 ± 0.88
6.2 ± 0.2	21.1 k0.7	1950.0± 12.2	20.40 ± 2.48
15.3± 0.4	21.6 ± 0.8	1933.3± 26.4	4.08 ± 0.26
30.7 ± 0.5	24.0 ± 0.8	1952.8± 6.7	0.94 ± 0.02
44.0 ± 1.2	26.5 ± 1.8	1934.4± 10.0	0.36 ± 0.02

6.3.4 Air in water, 50 μm capillary

Table 6-4 displays the experimental results for trials involving a 50 μm capillary with air as the saturating gas. The water was saturated with air at 1400 psig for 2, 3, 10, 25, and 40 minutes yielding respective average supersaturation ratios of 4.1, 6.7, 15.7, 32.1, and 44.3. Bubble detachment diameter, although lower than the trials involving the 200 and 450 μm capillaries, remained essentially unchanged while bubble growth times decreased with increasing supersaturation ratio.

SSR	T (°C)	D_{max} (μm)	t_G (min)
4.1 ± 0.1	20.3 ± 0.9	1894.4 ± 32.9	40.57 ± 1.97
6.7 ± 0.4	21.3 ± 1.8	1852.8 ± 10.9	15.14 ± 1.43
15.7 ± 0.6	24.3 ± 0.7	1861.1 ± 37.5	3.83 ± 0.20
32.1 ± 0.9	23.5 ± 0.9	1847.2 ± 47.9	0.77 ± 0.04
44.3 ± 0.7	24.9 ± 1.0	1865.7 ± 30.3	0.32 ± 0.02

6.3.5 Air in water – double saturation time & half saturation pressure, 450 μm capillary

Table 6-5 displays the experimental results for trials involving a 450 μm capillary with air as the saturating gas. The water was saturated with air at 700 psig for 4, 6, 20, 50, and 80 minutes yielding respective average supersaturation ratios of 4.7, 7.5, 18.8, 30.1, and 39.4. Using double the saturation time and half the saturation pressure resulted in similar supersaturation ratios. Bubble detachment diameter remained essentially unchanged while bubble growth times decreased with increasing supersaturation ratio.

Table 6-5. Experimental results for air in water, 450 μm capillary (double the saturation time and half the saturation pressure).

SSR	T (°C)	D_{max} (μm)	t_G (min)
4.7 ± 0.2	22.7 ± 0.6	2350.0 ± 10.2	56.69 ± 2.48
7.5 ± 0.2	24.3 ± 0.5	2352.8 ± 6.7	20.27 ± 1.12
18.8 ± 0.8	25.6 ± 1.7	2369.4 ± 6.7	4.00 ± 0.25
30.1 ± 0.4	29.7 ± 1.3	2350.0 ± 13.3	1.47 ± 0.07
39.4 ± 1.5	29.8 ± 1.5	2352.8 ± 6.7	0.70 ± 0.02

6.3.6 Air in water – partial depressurization, 50 μm capillary

Table 6-6 displays the experimental results for trials involving a 50 μm capillary with air as the saturating gas that has been depressurized down to an intermediate pressure. The water was saturated with air at 1400 psig for 10, 25, and 40 minutes, but was depressurized down to 72.5 psig instead of 0 psig. This resulted in average supersaturation ratios of 3.6, 5.5, and 8.1, respectively. The seeded air bubbles did not reemerge from the 200 and 450 μm capillaries at an intermediate pressure of 72.5 psig, so a 50 μm capillary was used exclusively in these partial depressurization experiments.

SSR	T (°C)	D_{max} (μm)	t_G (min)
3.6 ± 0.2	27.6 ± 0.8	1883.3 ± 20.4	52.39 ± 1.61
5.5 ± 0.1	26.7 ± 0.9	1877.8 ± 10.2	21.63 ± 0.34
8.1 ± 0.4	28.2 ± 2.7	1888.9 ± 25.8	11.16 ± 0.23

6.3.7 Carbon dioxide in water, 450 μm capillary

Table 6-7 displays the experimental results for trials involving a 450 μm capillary with carbon dioxide as the saturating gas. The water was saturated with carbon dioxide at 75 psig for 5, 10, 15, and 20 minutes yielding respective average supersaturation ratios of 1.6, 2.3, 3.1, and 3.7. Bubble detachment diameter, similar to the air trials involving a 450 μm capillary, remained essentially unchanged while bubble growth times decreased with increasing supersaturation ratio.

Table 6-7. Experimental results for carbon dioxide in water, 450 μm capillary.

SSR	*T* (°C)	D_{max} (μm)	t_G (min)
1.6 ± 0.1	27.9 ± 1.3	2313.9 ± 10.9	3.11 ± 0.54
2.3 ± 0.1	30.4 ± 1.3	2327.8 ± 10.9	0.49 ± 0.05
3.1 ± 0.1	31.1 ± 1.1	2333.3 ± 12.2	0.17 ± 0.01
3.7 ± 0.1	32.8 ± 1.7	2319.4 ± 19.2	0.09 ± 0.01

6.3.8 Helium in water, 450 μm capillary

Table 6-8 displays the experimental results for trials involving a 450 μm capillary with helium as the saturating gas. The water was saturated with helium at 1400 psig for 1, 2, 3, 5, 7 and 10 minutes yielding respective average supersaturation ratios of 8.5, 12.0, 16.7, 32.2, 40.1, and 49.7. Bubble detachment diameter, similar to the air and carbon dioxide trials involving a 450 μm capillary, remained essentially unchanged while bubble growth times decreased with increasing supersaturation ratio.

Table 6-8. Experimental results for helium in water, 450 μm capillary.

SSR	*T* (°C)	D_{max} (μm)	t_G (min)
8.5 ± 0.3	23.1 ± 0.7	2347.2 ± 12.2	24.34 ± 1.96
12.0 ± 0.2	22.3 ± 0.9	2355.6 ± 13.9	11.19 ± 0.81
16.7 ± 1.8	25.3 ± 0.5	2338.9 ± 13.9	5.85 ± 0.96
32.2 ± 0.3	25.7 ± 1.3	2344.4 ± 10.2	1.88 ± 0.11
40.1 ± 1.8	24.1 ± 1.4	2350.0 ± 30.3	1.40 ± 0.06
49.7 ± 1.6	26.8 ± 1.1	2330.6 ± 10.2	0.87 ± 0.05

6.3.9 Helium in water – temperature studies, 450 μm capillary

Table 6-9 displays the experimental results for trials involving a 450 μm capillary with helium as the saturating gas in which the temperature was adjusted. Water temperatures were decreased by surrounding the test cell with ice and increased by surrounding he test cell with a hot water bottle. The water was first saturated with helium at 1400 psig for 5 minutes at 14.1 and 42.3°C yielding supersaturation values of

24.8 and 44.6. Next, to achieve similar supersaturation ratios at a high and low temperature, water was saturated with helium at 1400 psig for 7.5 minutes at 14.9ºC and for 3 minutes at 41.4ºC. Bubble detachment diameters were lower for the higher temperature trials while bubble growth times decreased with increasing supersaturation ratio.

SSR	T (ºC)	D_{max} (μm)	t_G (min)
24.8 ± 0.6	14.1 ± 0.7	2352.8 ± 16.3	3.97 ± 0.21
44.6 ± 1.0	42.3 ± 0.7	2291.7 ± 8.6	0.70 ± 0.08
32.7 ± 1.1	14.9 ± 0.8	2347.2 ± 14.9	2.25 ± 0.29
31.9 ± 0.4	41.4 ± 0.8	2305.6 ± 12.2	1.41 ± 0.14

6.3.10 Comparison Graphs

Three graphs of bubble growth time ***vs.*** supersaturation ratio were then constructed so that visual comparisons of the experimental data could be made. It was expected that there would be little difference when comparing the bubble growth time vs. supersaturation ratio curves for air bubbles in water from a 450 μm capillary, a 450 μm capillary repeat, and a 450 μm capillary using double the saturation time and half the saturation pressure. In Figure 6-5, these three curves all lie on top of one another with only one instance where the 95% confidence intervals do not appear to overlap. It was not expected that the bubble growth time ***vs.*** supersaturation ratio curves for air bubbles in water from 50, 200, and 450 μm capillaries would lie completely on top of one another. In fact, Figure 6-6 indicates that bubble growth time systematically increases with increased capillary size. At the higher supersaturation ratios, this effect becomes less discernable. Also, it was not expected that the bubble growth time ***vs.***

supersaturation ratio curves for air, carbon dioxide, and helium bubbles in water would lie on top of one another, due to differences in solubility and diffusivity that these species have in water. Figure 6-7 shows that the helium curve lies above the air curve. The carbon dioxide bubble growth times are significantly lower and require much smaller supersaturation ratios.

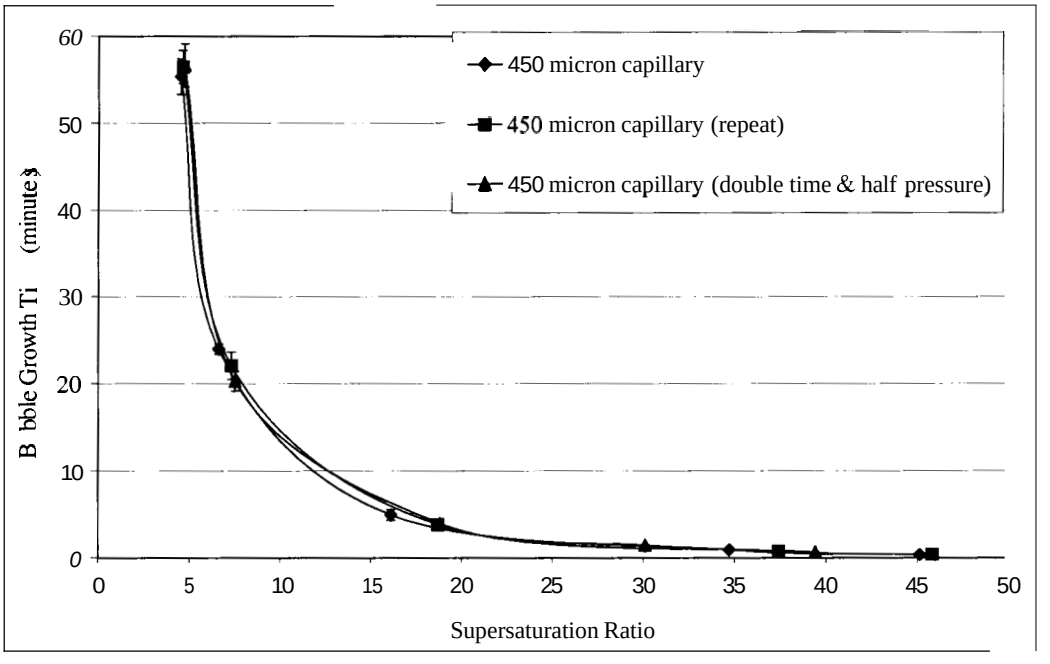

Figure *6-5.* Comparison of experimentally measured bubble growth times as a function of supersaturation ratio from a 450 μm ID capillary for three distinct trials, involving air dissolved in water.

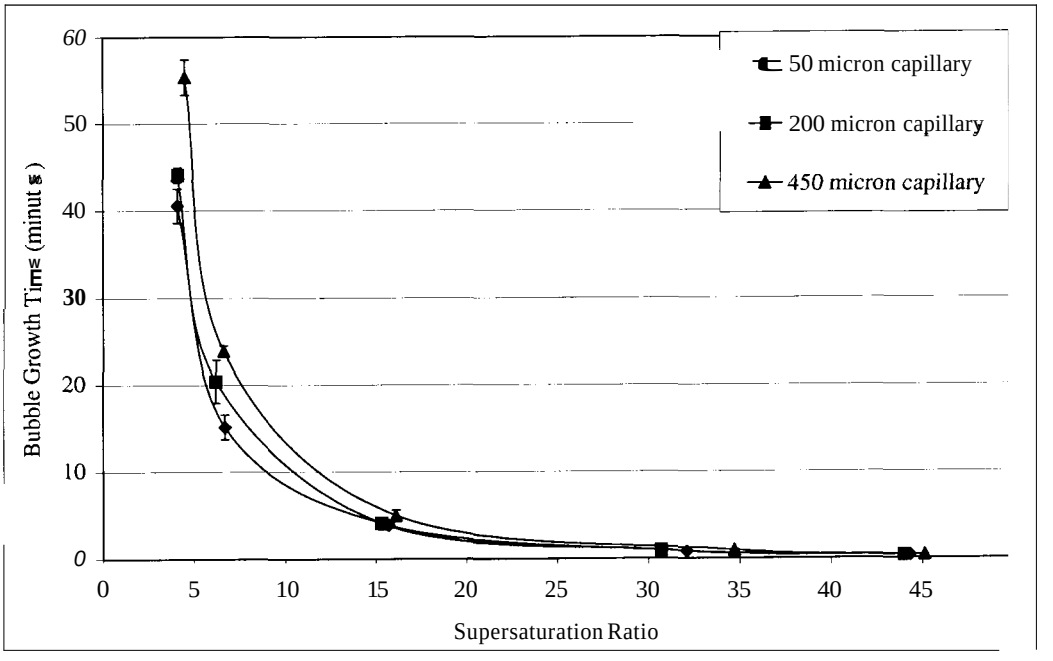

Figure 6-6. Comparison of experimentally measured bubble growth times as a function of supersaturation ratio from 50, 200, and 450 μm capillaries, involving air dissolved in water.

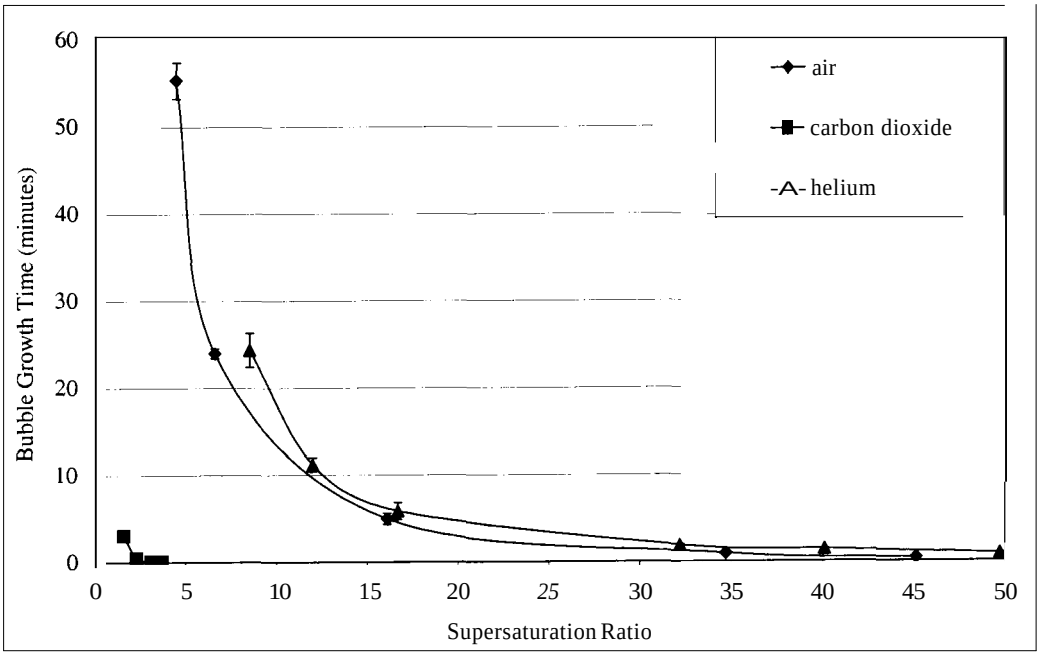

Figure 6-7. Comparison of experimentally measured bubble growth times as a function of supersaturation ratio from a 450 μm ID capillary for air, carbon dioxide, and helium dissolved in water.

6.4 Discussion of Experimental Results

From the "nucleation" lapse time experiments reported in **96.1,** a systematic trend of increased bubble detachment diameters (which corresponded to increased capillary sizes) resulted in increased lapse times. This is the behavior that Jones *et al*. (1998) predicted would occur; however, it was required that all the capillaries be smoothly cut so that a small bubble cap appeared at the tip of the capillary upon detachment. "Nucleation" lapse time measurements from the soda bottle experiments described in **93.3** did not show a systematic correlation between bubble detachment diameter and lapse time. This can be attributed to the fact that naturally occurring cavities containing trapped gases have variable geometries. Variable geometries could cause the bubble to shear away at different locations and leave a bubble cap at some unpredictable depth inside the naturally occurring cavity. Jones *et al*. (1998) believed that larger detaching bubbles would result in a larger depleted dissolved gas zone which would therefore increase lapse times by reducing the available amount of locally dissolved gas. The authors did not account for variable geometries, and the trend that they predicted was only observed in the experiments of §6.1 when the site geometry was held constant. Depleted dissolved gas zone sizes for the detaching bubbles could not be directly measured. An alternate explanation for larger detaching bubbles having longer lapse times from smooth and flat cut capillaries would be that it simply takes longer for a bubble to become larger than the capillary opening for larger capillary inside diameters.

The experiments described in §6.2 provided a better picture of the long term behavior at a bubble producing site. Bubble detachment diameter remained essentially constant from bubble to bubble while bubble growth times increased as dissolved gas

concentrations decreased. It was also logical to no longer consider "nucleation" lapse times, since it was determined to be an artifact of the experiment in that it depends on the bubble becoming larger than the site opening so that it can be visually observed. From the long term behavior studies performed on the 450 μm capillaries at four supersaturation ratios, the non-systematic trend in bubble growth time and dissolved gas concentration curves can be explained by the fact that the dissolved gas concentration dropped off in precipitous fashion initially for the highest supersaturation ratio. This large initial drop was caused by the presence of more interfering bubbles which more quickly depleted the dissolved gas concentration. Nevertheless, experiments could be performed at these higher supersaturation ratios if the analysis was limited to the first full bubble only.

The repeatability of the first full bubble only experiments was first verified in §6.3 by completing repeated trials involving a 450 μm capillary. Similar supersaturation ratios and bubble growth times were achieved. **As** expected, when plotting these results on a bubble growth time *vs.* supersaturation ratio graph along with results from another set of experiments involving half the saturation time and half the saturation pressure, all three curves appeared to lie almost completely on top of one another. Surprisingly, there was not a very large difference in bubble detachment diameters from the three different capillary sizes. Typical bubble detachment diameters from the 50, 200, and 450 μm capillaries were 1850, 1950, and 2330 pm, respectively. Despite the fact the initial bubble cap was smallest for the 50 μm capillary, bubble growth times increased with increasing capillary size. It was also interesting to investigate two other gases, carbon dioxide and helium, in place of air. Carbon dioxide in water had a similar diffusion

coefficient to air in water, but a much higher solubility. This led to a very rapid bubble growth at small supersaturation ratios. The high diffusivity of helium in water made it difficult to obtain low supersaturation ratios, but the reduced solubility compared to air in water resulted in similar bubble growth times. The partial depressurization experiments and helium temperature studies were mainly performed for comparison with bubble growth models.

7. Bubble Growth Modeling

The growth of a gas bubble in a supersaturated liquid solution may be described by the equation of continuity. Assuming a spherically symmetric bubble in which no chemical reactions occur, the equation of continuity in spherical coordinates for constant density and diffusion coefficient reduces to,

$$\frac{\partial C_A}{\partial t} + v_r \cdot \frac{\partial C_A}{\partial r} = D_{AB} \cdot \frac{1}{r^2} \cdot \frac{\partial}{\partial r}\left(r^2 \cdot \frac{\partial C_A}{\partial r} \right), \tag{7-1}$$

where ***A*** denotes the gas species, C_A is the concentration of ***A*** in the liquid, t is time, r is the radial coordinate, v_r is the velocity of the surrounding liquid at position r, and D_{AB} is the diffusion coefficient of the dissolved gas ***A*** in the liquid B.

Several previous theoretical treatments including Manley (1960), Barlow and Langlois (1962), Bankoff (1966), Cha and Henry (1981), and Bisperink and Prins (1994) have neglected the convective term, which leads to a simplified form of Equation 7-1,

$$\frac{\partial C_A}{\partial t} = D_{AB} \cdot \frac{1}{r^2} \cdot \frac{\partial}{\partial r}\left(r^2 \cdot \frac{\partial C_A}{\partial r} \right). \tag{7-2}$$

Scriven (1959) first presented a solution of Equation 7-1, including both the diffusive and convective terms. Some aspects of Scriven's solution were incorporated by later investigators, including Li and Yortsos (1995) and Venerus and Yala (1997), who studied bubble growth in porous media and in high viscosity polymer solutions, respectively. Scriven's solution describes the growth of a single bubble in an infinite medium due to either heat or mass transfer.

In this chapter, the diffusion only solution of Manley and the diffusion and convection solution of Scriven are described in greater detail in §7.1. **A** new bubble

growth model, denoted C-T (Cyr-Thompson), incorporating aspects from both of the earlier solutions, is described in §7.2. Experimentally determined bubble growth times are compared to the Manley, Scriven, and C-T model predictions in **97.3.** Finally, **97.4** presents a discussion on the modeling results.

7.1 Previous Models

7.1.1 Manley (1960)

Manley developed an approximate analytical solution to Equation 7-2 by extending the earlier work of Epstein and Plesset (1950). This solution takes the form,

$$D^2 = D_0^2 + \frac{8 \cdot D_{AB} \cdot (C_{A0} - C_{AS}) \cdot t}{\rho_G}, \tag{7-3}$$

where D is the bubble diameter at time t, D_0 is the initial bubble diameter, C_{A0} is the initial bulk concentration of A, C_{AS} is the saturated equilibrium concentration, and ρ_G is the gas density. Equation 7-3 depends on the following initial and boundary conditions,

$$at\ t = 0,\ C_A = C_{A0}, \tag{7-4}$$
$$at\ r \leq R,\ C_A = C_{AS}, \tag{7-5}$$
$$at\ r = \infty,\ C_A = C_{A0}, \tag{7-6}$$

where R is the bubble radius.

The sample calculations in Appendix H.3 explain and illustrate how the experimental parameters can be used to calculate the bubble growth time using a rearranged form of Equation 7-3. This is the bubble growth time predicted using the theory of Manley (t_M).

7.1.2 Scriven (1959)

Scriven (1959) developed a numerical type solution after recasting Equation 7-1 in conjunction with a mass balance equation at the bubble surface in a dimensionless form. This solution takes the form,

$$D = 4 \cdot \beta(\phi) \cdot \sqrt{D_{AB} \cdot t}, \tag{7-7}$$

where β is a dimensionless growth parameter that depends on the quantity, ϕ, a supersaturation parameter defined by,

$$\phi = \frac{\rho_L \cdot (C_{A0} - C_{AS})}{\rho_G \cdot (\rho_L - C_{AS})}, \tag{7-8}$$

where ρ_L is the liquid density.

Table 1 of Scriven (1959) provides a $\beta = \beta$ ($) correlation for selected discrete points. Instead of interpolating between these points, a simple Mathcad program, appearing in Appendix F, was created to obtain a more complete correlation from the same expression Scriven used. Table 1 of Scriven (1959) was undoubtedly obtained with much computational effort, but today the calculations can be easily performed with a Mathcad program. In Table 7-1, the discrete points calculated with Scriven are compared with the results obtained from Mathcad. The extremely low percent difference values indicate a negligible difference between the two methods. The advantage of using the Mathcad program is to avoid interpolation between the discrete points calculated by Scriven.

Table 7-1. Comparison of the $\beta = \beta(\phi)$ correlation for selected discrete points in Scriven with the Mathcad program results.

β	ϕ, Scriven	ϕ, Mathcad	% Difference
0.06	0.006504	0.006505	+0.015%
0.08	0.0112	0.0112	0.000%
0.10	0.01697	0.01697	0.000%
0.15	0.03546	0.03546	0.000%
0.20	0.05881	0.05881	0.000%
0.30	0.11660	0.11658	-0.017%
0.40	0.18500	0.18501	+0.005%
0.60	0.34200	0.34204	+0.012%
0.80	0.51520	0.51521	+0.002%
1.00	0.69770	0.69773	+0.004%
1.50	1.17500	1.17537	+0.031%

Initial and boundary conditions for Scriven's solution in Equation 7-7 are,

$$at\ t = 0,\ C_A = C_{A0}\ , \tag{7-9}$$

$$at\ t = 0,\ \dot{R} = 0\ , \tag{7-10}$$

$$at\ r = \infty,\ C_A = C_{A0}\ , \tag{7-11}$$

$$at\ r = R,\ \left(\frac{\partial C}{\partial r}\right) = \frac{\rho_G \cdot \dot{R}}{D_{AB}}, \tag{7-12}$$

where $\dot{R}$ is the bubble surface velocity. The boundary condition in Equation 7-12 requires that the gas density be very small compared to the liquid density.

The sample calculations in Appendix H.4 explain and illustrate how experimental parameters can be used to predict the bubble growth time using a rearranged form of Equation 7-7. This is the bubble growth time predicted using the theory of Scriven (t_S).

7.2 Development of the C-T Model

The C-T model is similar to the Scriven theory in that it also accounts for both diffusion and convection. In the C-T model, there is an improvement in the bubble surface velocity term and an additional restriction on one of the boundary conditions.

The initial condition stated by Equation 7-10 is that at $t = 0$ (immediately after depressurization), the bubble surface velocity is zero. The following analysis shows that this is not a good assumption and that the bubble surface velocity is in fact non-zero at $t = 0$.

Since bubble diameter squared *vs.* time is linear, it follows that the functional form of R^2 is given by,

$$R^2 = R_0^2 + c \cdot t \,, \tag{7-13}$$

where R_0 is the initial bubble radius and c is a constant. Taking the square root of both sides of Equation 7-13 and examining only positive values of R yields,

$$R = \sqrt{R_0^2 + c \cdot t} \,. \tag{7-14}$$

An expression for $\dot{R}$ may be obtained by taking the first derivative of Equation 7-14 with respect to time, resulting in,

$$\dot{R} = \frac{c}{2 \cdot \sqrt{R_0^2 + c \cdot t}} \tag{7-15}$$

Letting $t = 0$, which corresponds to the moment immediately after depressurization, a finite value for the bubble surface velocity is obtained. A plot of Equation 7-15 appears in Figure 7-1. It is evident that the bubble surface velocity is a maximum value at $t = 0$. This treatment of the bubble surface velocity is an essential new feature of the C-T model. It appears that Scriven assigned an initial value of the

bubble surface velocity equal to zero to avoid a singularity since his solution assumed that $R_0 = 0$.

The C-T model is a solution of Equation 7-1 with the initial and boundary conditions,

$$at\ t = 0,\ C_A = C_{A0}, \tag{7-16}$$

$$at\ r = R,\ \left(\frac{\partial C}{\partial r}\right) = \frac{\rho_G \cdot \dot{R}}{D_{AB}}, \tag{7-17a}$$

$$at\ r = R,\ C_A \geq C_{AS}, \tag{7-17b}$$

$$at\ r = \infty,\ C_A = C_{A0}. \tag{7-18}$$

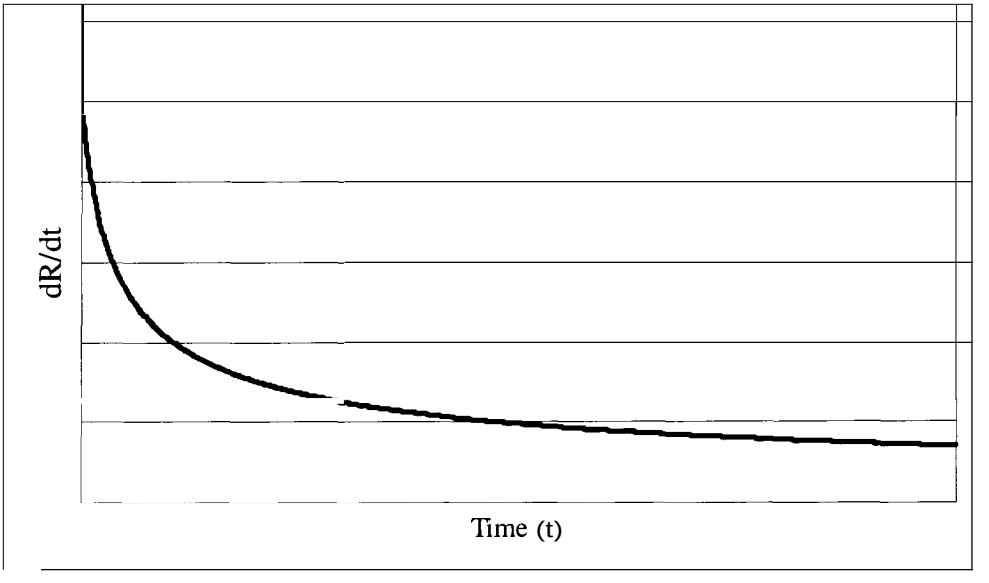

Figure 7-1. Theoretical bubble surface velocity as a function of time.

The boundary condition given by Equation 7-17b provides an additional restriction to the liquid concentration at the bubble surface that is not present in the Scriven model. The appropriate concentration gradient described by Equation 7-17a is maintained, but now the concentration in the liquid phase just outside the bubble is not allowed to fall below the equilibrium C_{AS} value. The gas inside the bubble would begin to redissolve back into the liquid phase if the concentration was allowed to fall below the equilibrium value.

Equation 7-15 is used to compute the bubble surface velocity as a function of time. The bubble surface velocity is related to the v_r term in Equation 7-1 in the same manner as in Scriven's work.

This partial differential equation is solved using the explicit form of the difference equation as outlined by Carnahan (1969). The method maintains first order accuracy in time and second order accuracy in the radial coordinate. A complete listing of the FORTRAN code appears in Appendix G. Input parameters for the C-T model include initial bubble radius, diffusion coefficient, time step increment, radial coordinate grid size, initial time, bubble detachment diameter, bubble growth time, gas density, a location "infinitely" far away from the bubble surface, C_{A0}, and C_{AS}. A value for the constant c that appears in Equations 7-13 through 7-15 is computed from the bubble detachment diameter (D_{max}) and bubble growth time (t_G).

The program calculates the concentration profile surrounding the bubble throughout time. For each time step, the program calculates the mass of dissolved gas that has entered the bubble, denoted *LHS* for left hand side of the mass balance, and the

mass of dissolved gas that has left the solution, denoted *RHS* for right hand side of the mass balance. The appropriate formulas for calculating the *LHS* and *RHS* values are,

$$LHS = \frac{4}{3} \cdot \pi \cdot \left(R^3 - R_0^3 \right) \cdot \rho_G \quad , \tag{7-19}$$

$$RHS = 4 \cdot \pi \cdot \int_R^\infty \left(C(\infty) - C(r) \right) \cdot r^2 \cdot dr \; . \tag{7-20}$$

By taking the percent difference between the *LHS* and *RHS* values, the initial mass balance error can be calculated; this value is almost always less than 20%. The bubble growth time is then adjusted and the program is re-executed until the *LHS* and *RHS* values agree to within **1%.** The bubble growth time that achieves this agreement in the mass balance is the predicted bubble growth time from the C-T model (t_{CT}).

A distance three times the largest maximum bubble diameter (7.05 mm) was found to sufficiently represent a location "infinitely" far away from the bubble surface since the concentration profiles remained unchanged near this "infinite" location. The time step increment was set such that the ratio of the time step increment divided by the chosen radial coordinate grid size squared was less than 0.5. Also, a radial coordinate grid size of 0.01250 mm, corresponding to 564 radial grid points, was found to be optimum.

Figure 7-2 helps show how the optimum radial coordinate grid size was determined. The raw data averages from Table E-1 were used in this determination. At the largest radial coordinate grid size of 0.10000 mm, the program executed in 20-30 seconds (using a computer with a 400 MHz microprocessor). The accuracy from using this particular grid size was gauged by cutting the grid size in half and re-executing the program. **As** seen in Figure 7-2, the *RHS* value increased by over 20% when changing to

a grid size of 0.05000 mm. The program executed in 1-2 minutes at this grid size. By continuing to cut the grid size in half and re-executing the program, it was observed that the *RHS* value started to level out. A grid size of 0.01250 mm was chosen as an optimal size because it provides a reasonable trade off between accuracy and computation time. The program executed in 45-60 minutes at a grid size of 0.01250 mm. The *RHS* value changed by less than 2% when cutting the grid size down to 0.00625 mm, and the program required 6-8 hours to execute. Since *RHS* values may be in error by 2%, it seemed logical to only require a 1% agreement between *LHS* and *RHS* when finding t_{CT}.

The sample calculations of Appendix H.5 describe an example in which input data is supplied to the FORTRAN program. The initial LSH and RHS values are listed along with the t_{CT} value needed to achieve agreement to within 1%.

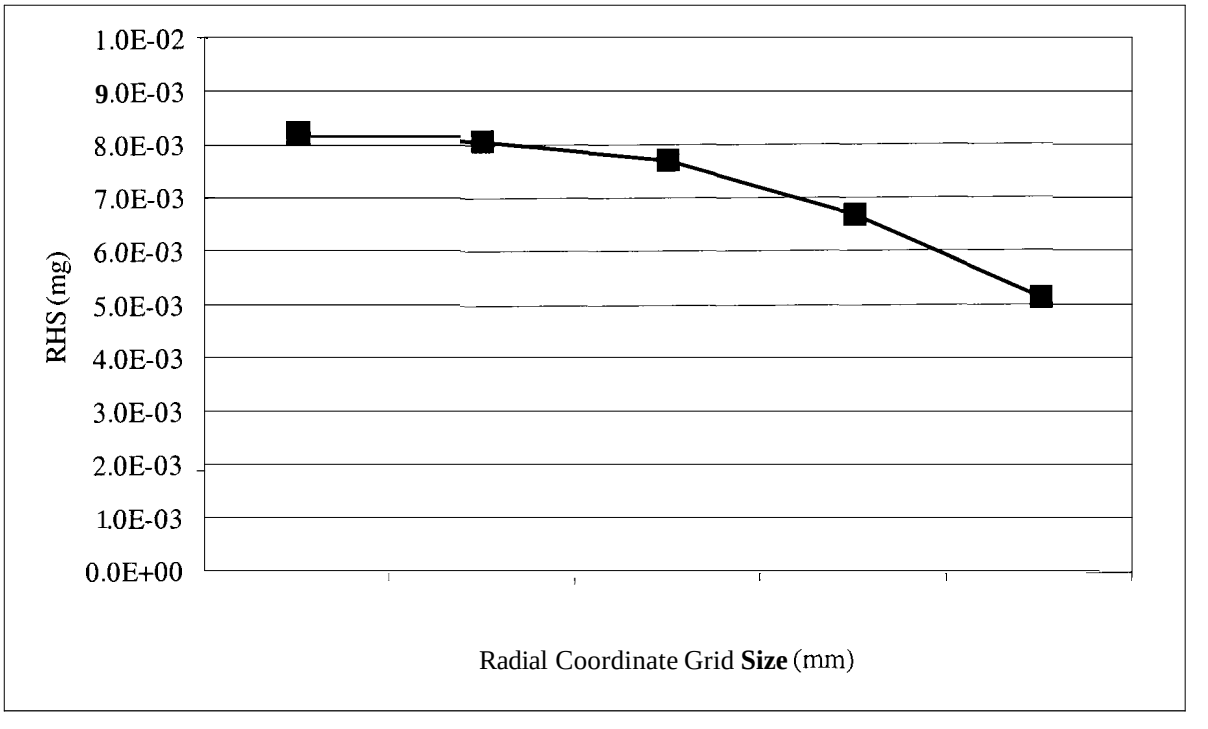

Figure 7-2. *RHS* value as function of the radial coordinate grid size plot used for determining the optimum radial coordinate grid size.

7.3 Results from the First Full Bubble Only Experiments Fit to the Manley, Scriven, and C-T Models

From the raw data tables of the experimental results appearing in Appendix E, calculated results in corresponding tables appear in Appendix I. For example, the raw data in Table E-7 corresponds to the calculated results in Table 1-7. Sample calculations in Appendix H explain how the raw data from the first full bubble only experiments in Appendix E are converted to the calculated results in Appendix I. The experimentally measured bubble growth times can then be compared to the bubble growth times predicted by the Manley, Scriven, and C-T models. Error bars calculated from 95% confidence intervals were determined for all bubble growth times except for the bubble growth time predicted by the C-T model which was determined from raw data averages.

7.3.1 Air in water, 450 μm capillary

Figure 7-3 displays the experimentally measured bubble growth times with the three theoretical predictions for trials involving a 450 μm capillary with air as the saturating gas. The water was saturated with air at 1400 psig for **2,** 3, 10, 25, and 40 minutes to generate five distinct supersaturation ratios. The Manley prediction shows the appropriate trend, but deviates the most from the experimental value for all of the supersaturation ratios. The Scriven theory agrees more closely with the experimental value at the lowest supersaturation ratio, but otherwise the C-T model provides a better prediction of bubble growth time for the remaining supersaturation ratios.

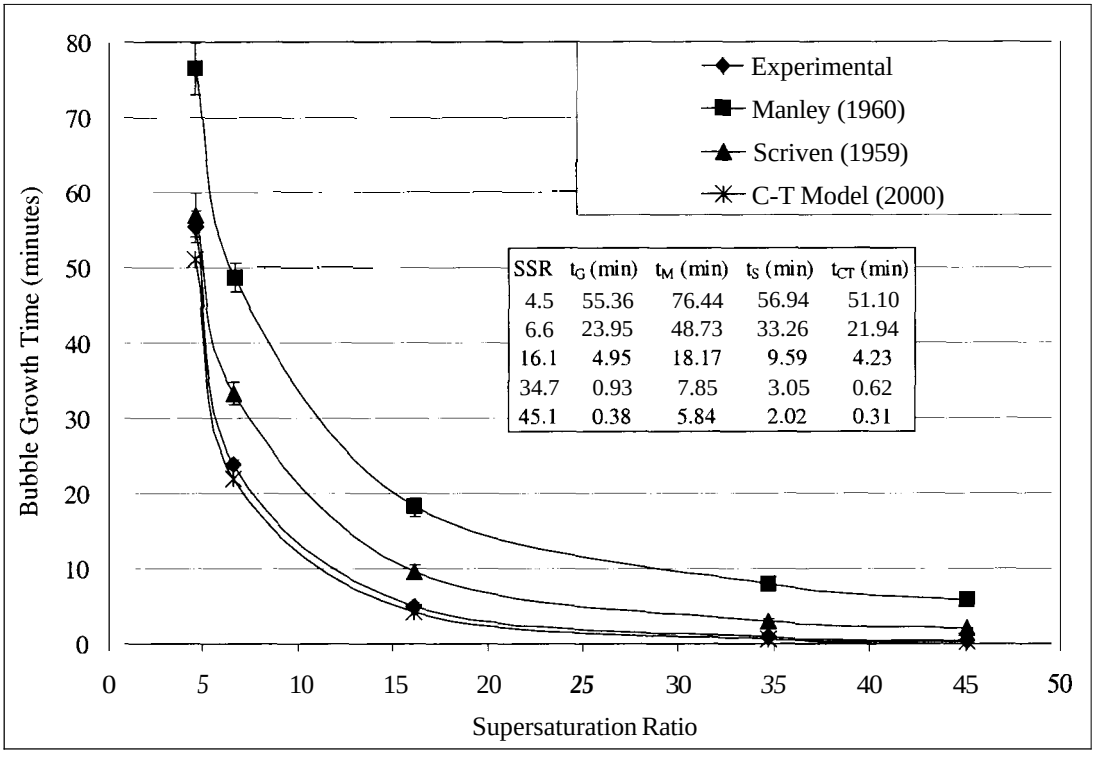

SSR	t_G (min)	t_M (min)	t_S (min)	t_{CT} (min)
4.5	55.36	76.44	56.94	51.10
6.6	23.95	48.73	33.26	21.94
16.1	4.95	18.17	9.59	4.23
34.7	0.93	7.85	3.05	0.62
45.1	0.38	5.84	2.02	0.31

Figure 7-3. Bubble growth time comparisons as a function of supersaturation ratio between actual experimental value and three theoretical predictions for air in water, 450 μm capillary. (note: **SSR** = supersaturation ratio, t_G = experimentally measured bubble growth time, t_M = bubble growth time predicted by Manley, t_S = bubble growth time predicted by Scriven, t_{CT} = bubble growth time predicted by the C-T model)

7.3.2 Air in water, 450 ym capillary (repeat)

Figure 7-4 displays the experimentally measured bubble growth times with the three theoretical predictions for trials involving a 450 μm capillary, under repeated conditions from the tests reported in §7.3.1, with air as the saturating gas. The water was saturated with air at 1400 psig for 2, 3, 10, 25, and 40 minutes to generate five distinct supersaturation ratios. The Manley prediction shows the appropriate trend, but deviates the most from the experimental value for all of the supersaturation ratios. The Scriven theory agrees more closely with the experimental value at the lowest supersaturation ratio, but otherwise the C-T model provides a better prediction of bubble growth time for the remaining supersaturation ratios.

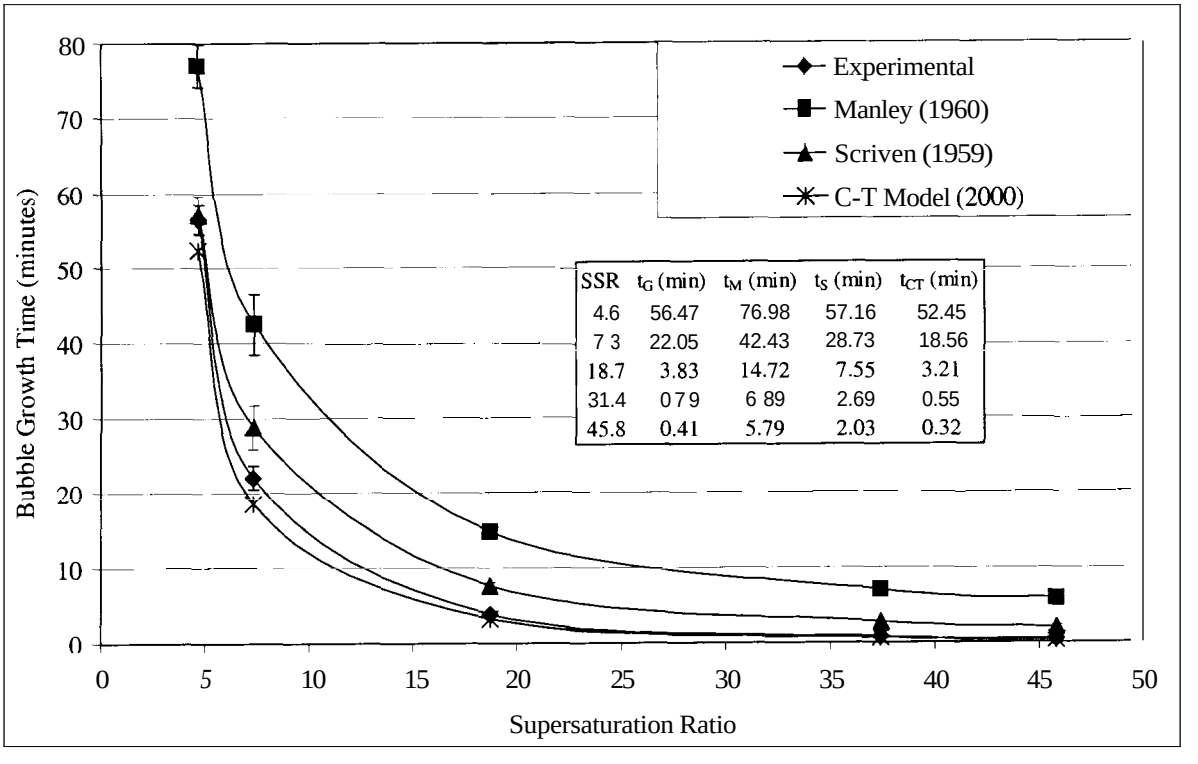

SSR	t_G (min)	t_M (min)	t_S (min)	t_{CT} (min)
4.6	56.47	76.98	57.16	52.45
7 3	22.05	42.43	28.73	18.56
18.7	3.83	14.72	7.55	3.21
31.4	0 7 9	6 89	2.69	0.55
45.8	0.41	5.79	2.03	0.32

Figure 7-4. Bubble growth time comparisons as a function of supersaturation ratio between actual experimental value and three theoretical predictions for air in water, 450 ym capillary (repeat).

7.3.3 Air in water, 200 μm capillary

Figure 7-5 displays the experimentally measured bubble growth times with the three theoretical predictions for trials involving a 200 μm capillary with air as the saturating gas. The water was saturated with air at 1400 psig for 2, 3, 10, 25, and 40 minutes to generate five distinct supersaturation ratios. The Manley prediction continues to over-predict the bubble growth times. The Scriven theory agrees more closely with the experimental value at the lowest supersaturation ratio, but otherwise the C-T model provides a better prediction of bubble growth time for the remaining supersaturation ratios.

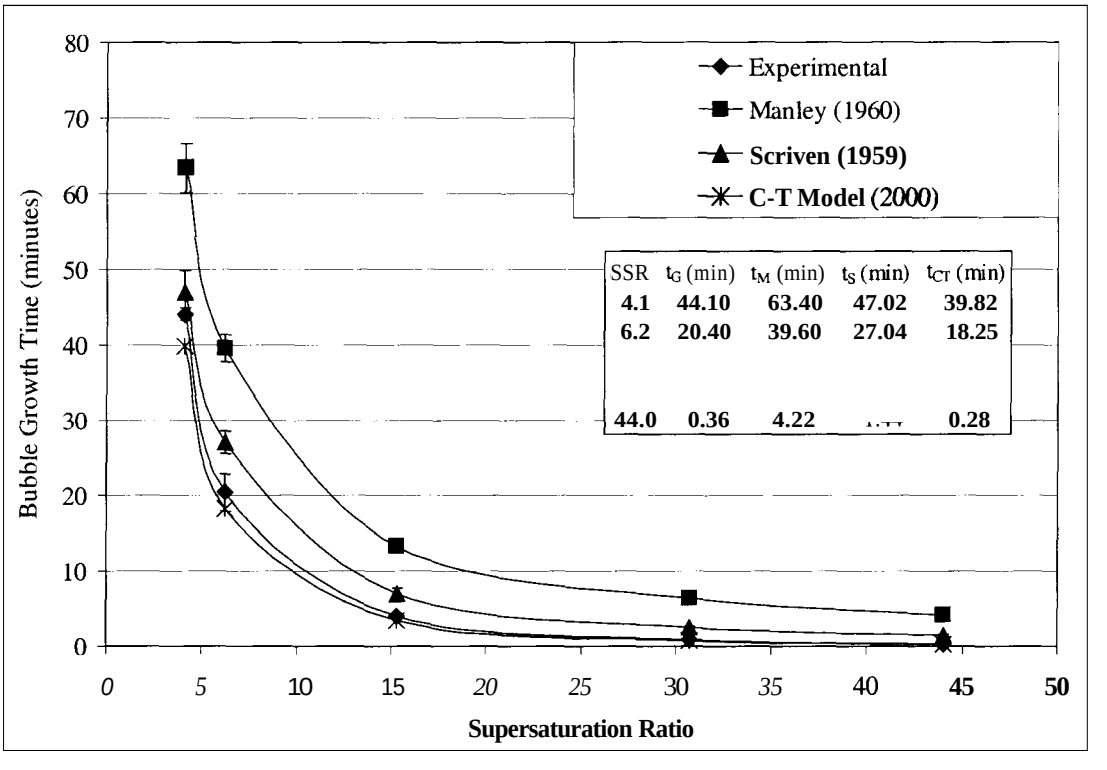

Figure 7-5. Bubble growth time comparisons as a function of supersaturation ratio between actual experimental value and three theoretical predictions for air in water, 200 μm capillary.

7.3.4 Air in water, 50 μm capillary

Figure 7-6 displays the experimentally measured bubble growth times with the three theoretical predictions for trials involving a 50 μm capillary with air as the saturating gas. The water was saturated with air at 1400 psig for 2, 3, 10, 25, and 40 minutes to generate five distinct supersaturation ratios. Consistent with previous findings, the Manley prediction deviates from the experimentally measured bubble growth time by the greatest amount. For the lowest supersaturation ratio, both the Scriven and C-T models had similar accuracy. For higher supersaturation ratios, the C-T model was once again the most accurate.

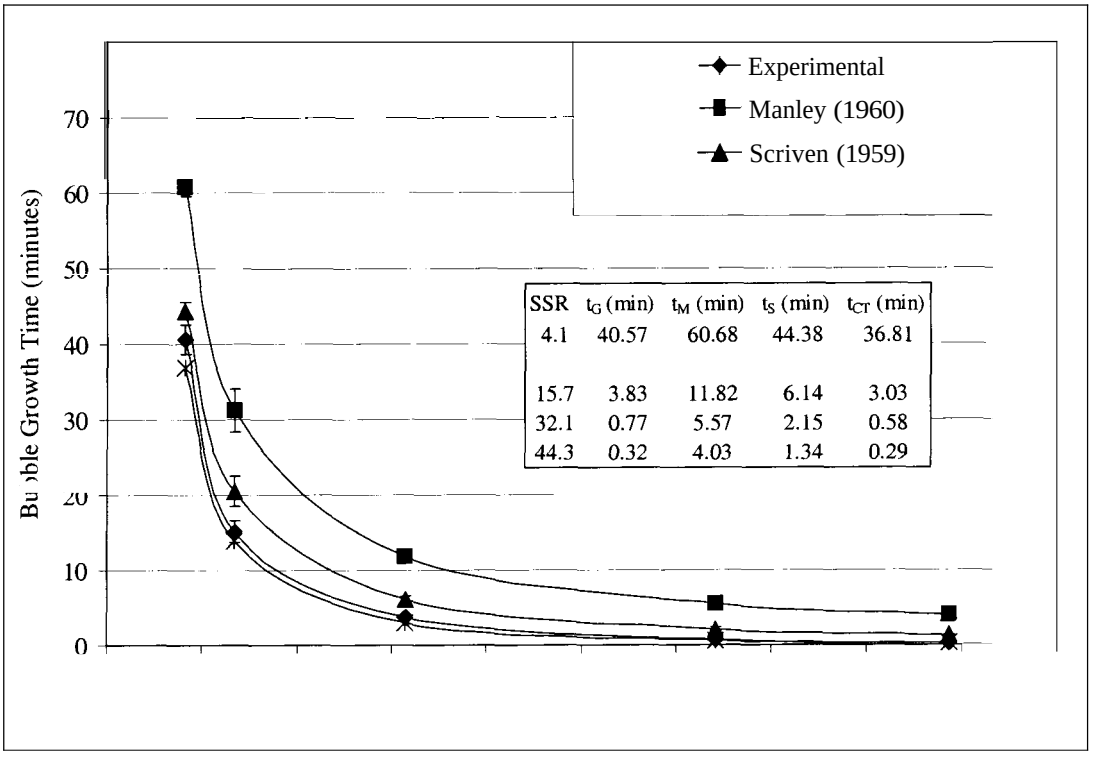

Figure 7-6. Bubble growth time comparisons as a function of supersaturation ratio between actual experimental value and three theoretical predictions for air in water, 50 μm capillary.

7.3.5 Air in water – double saturation time & half saturation pressure, 450 μm capillary

Figure 7-7 displays the experimentally measured bubble growth times with the three theoretical predictions for trials involving a 450 μm capillary using air in an altered saturation routine. The water was saturated with air at 700 psig for 4, 6, 20, 50, and 80 minutes to generate five distinct supersaturation ratios. Using double the saturation time and half the saturation pressure results in similar supersaturation ratios. The Manley theory continues to over-predict the bubble growth time. The Scriven theory more accurately approximates the bubble growth time at the lower supersaturation ratio while the C-T model is more accurate at the higher supersaturation ratios.

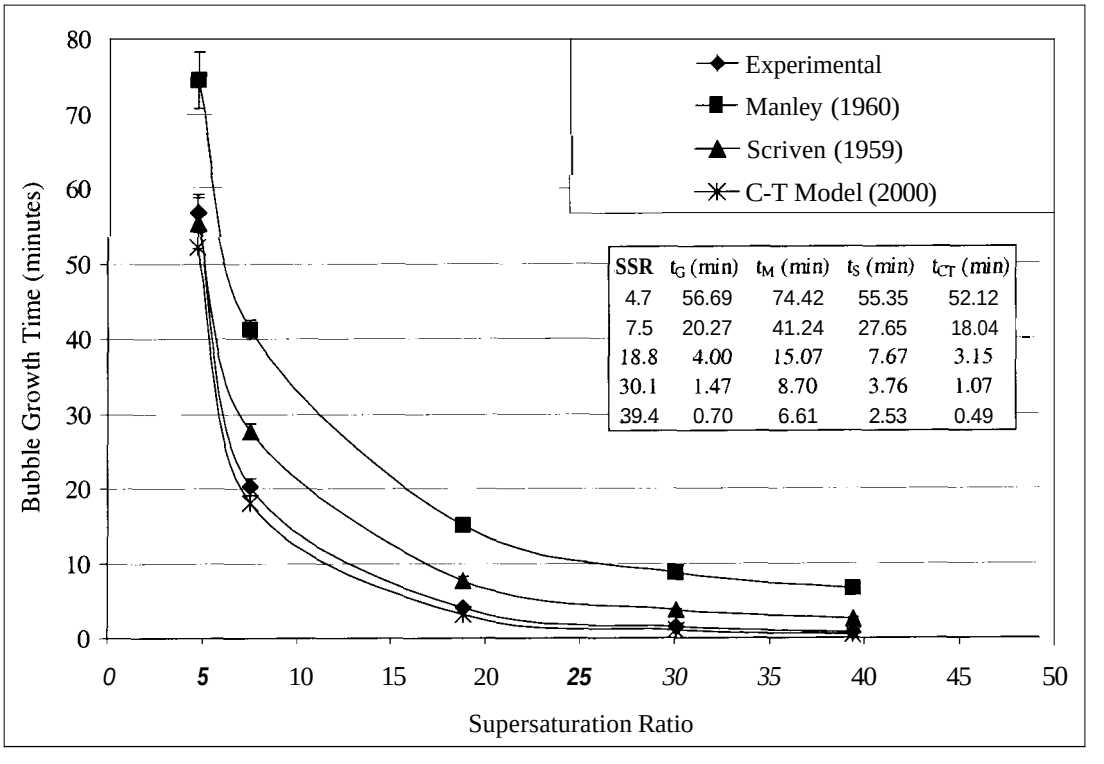

SSR	t_G (min)	t_M (min)	t_S (min)	t_{CT} (min)
4.7	56.69	74.42	55.35	52.12
7.5	20.27	41.24	27.65	18.04
18.8	4.00	15.07	7.67	3.15
30.1	1.47	8.70	3.76	1.07
39.4	0.70	6.61	2.53	0.49

Figure 7-7. Bubble growth time comparisons as a function of supersaturation ratio between actual experimental value and three theoretical predictions with double the saturation time and half the saturation pressure for air in water, 450 μm capillary.

7.3.6 Air in water – partial depressurization, 50 μm capillary

Figure 7-8 displays the experimentally measured bubble growth times with the three theoretical predictions for trials involving a 50 μm capillary with air as the saturating gas that has been depressurized down to an intermediate pressure. The water was saturated with air at 1400 psig for 10, 25, and 40 minutes, but was depressurized to approximately 6 atm instead of 1 atm. This results in smaller supersaturation ratios than in the previous cases because there is an increase in the equilibrium concentration due to the increased depressurization pressure. Once again, Manley over-predicts the bubble growth time. The C-T model provides a better fit to the bubble growth times particularly at the two higher supersaturation ratios, but is similar to the Scriven prediction at the lowest supersaturation ratio.

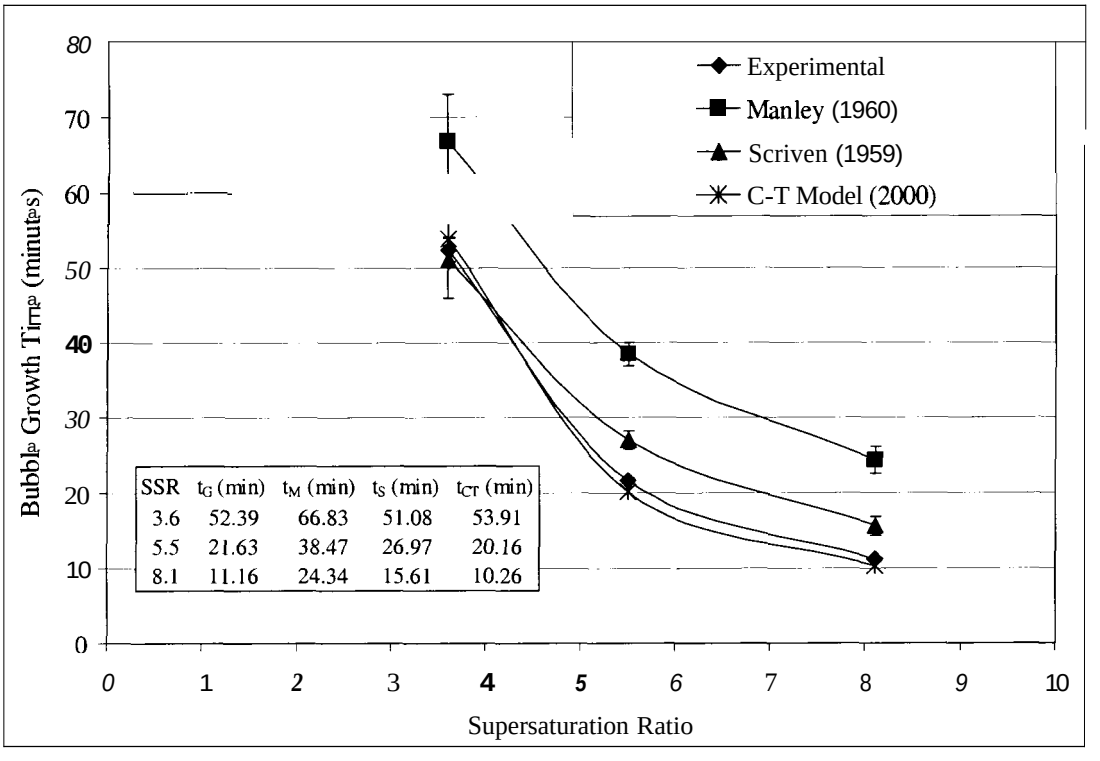

Figure 7-8. Bubble growth time comparisons as a function of supersaturation ratio between actual experimental value and three theoretical predictions with a partial depressurization down to 6 atm (instead of 1 atm) for air in water, 50 μm capillary.

7.3.7 Carbon dioxide in water, 450 μm capillary

Figure 7-9 displays the experimentally measured bubble growth times with the three theoretical predictions for trials involving a 450 mm capillary with carbon dioxide as the saturating gas. The water was saturated with carbon dioxide at 75 psig for 5, 10, 15, and 20 minutes. These conditions restricted the supersaturation ratios to levels below 5, but higher dissolved gas contents were still achieved because of the increased solubility of carbon dioxide in water. Carbon dioxide is approximately 30-60 times more soluble than air is in water, but has a similar diffusion coefficient. For this case, the C-T model more accurately predicts the bubble growth time than both the Manley or Scriven theories do for all four supersaturation ratios.

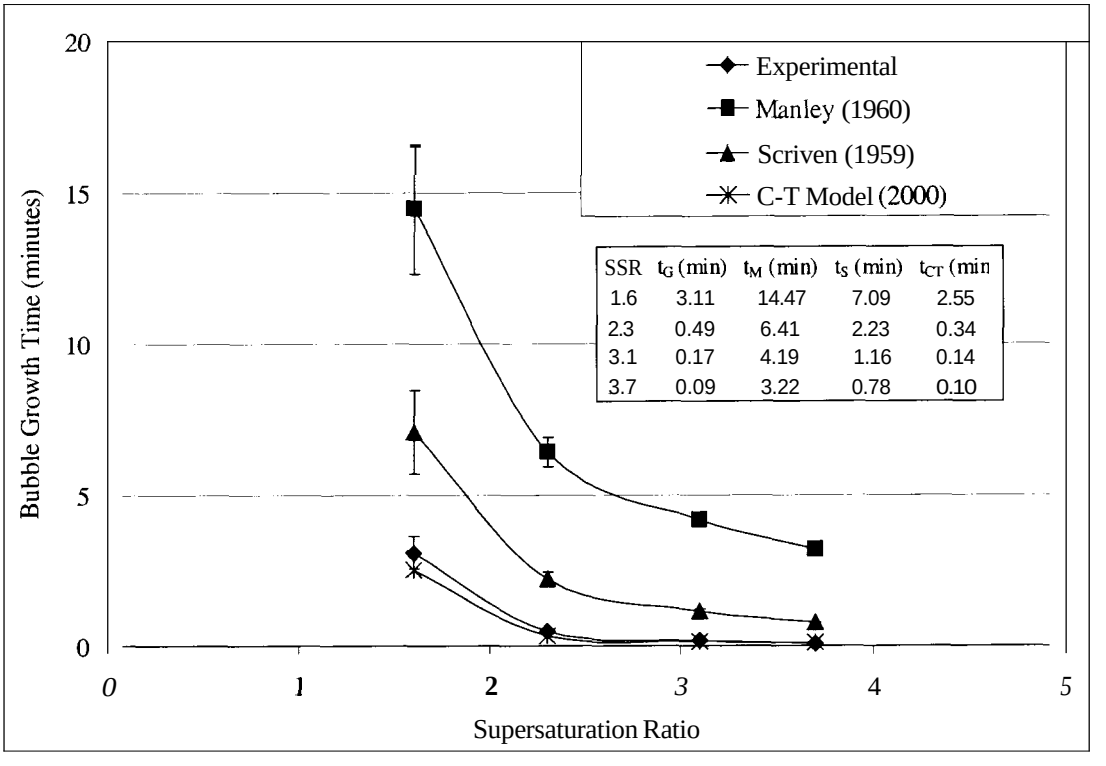

Figure 7-9. Bubble growth time comparisons as a function of supersaturation ratio between actual experimental value and three theoretical predictions for carbon dioxide in water, 450 μm capillary.

7.3.8 Helium in water, 450 μm capillary

Figure 7-10 displays the experimentally measured bubble growth times with the three theoretical predictions for trials involving a 450 μm capillary with helium as the saturating gas. The water was saturated with helium at 1400 psig for 1, 2, 3, 5, 7, and 10 minutes to generate six distinct supersaturation ratios. Helium is less soluble than air is in water, but has a diffusion coefficient almost three times larger. Manley over-predicts for all supersaturations. The Scriven and C-T model predictions are similar at the lowest supersaturation with the C-T model providing the superior fit for the higher supersaturation ratios.

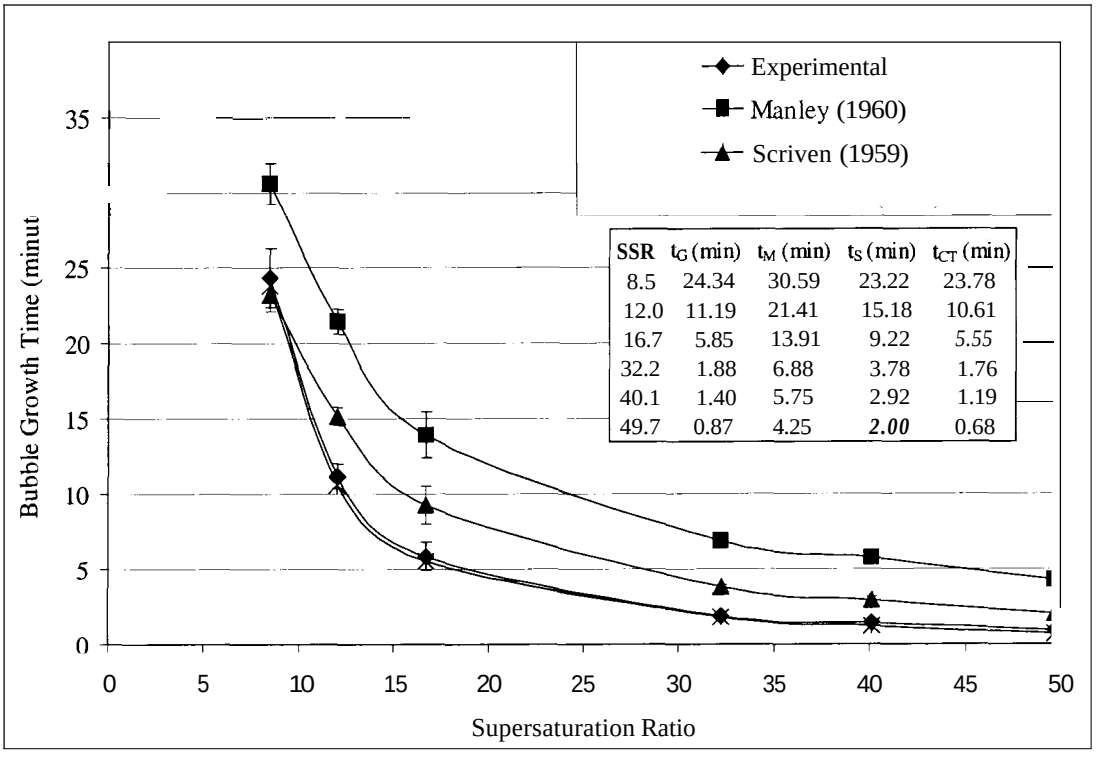

SSR	t_G (min)	t_M (min)	t_S (min)	t_{CT} (min)
8.5	24.34	30.59	23.22	23.78
12.0	11.19	21.41	15.18	10.61
16.7	5.85	13.91	9.22	*5.55*
32.2	1.88	6.88	3.78	1.76
40.1	1.40	5.75	2.92	1.19
49.7	0.87	4.25	***2.00***	0.68

Figure 7-10. Bubble growth time comparisons as a function of supersaturation ratio between actual experimental value and three theoretical predictions for helium in water, 450 μm capillary.

7.3.9 Helium in water – temperature studies, 450 μm capillary

Controlled temperature studies, involving a 450 μm capillary with helium dissolved in water, were performed to verify the validity of the temperature correction techniques applied to the diffusion coefficients. Appendix H.2 describes the details of this temperature correction technique. It was necessary to correct the diffusion coefficients for temperature because the literature reported diffusion coefficients at only one temperature for air in water, carbon dioxide in water, and helium in water. For example, Ferrell and Himmelblau (1967) listed the diffusion coefficient for helium in water at 25°C to be 6.280×10^{-9} m^2/s. Diffusion coefficients, corrected for temperature using the technique outlined in Appendix H.2, appear in Table J-3 of Appendix J.

Figure 7-11 displays the bubble growth time measured experimentally, the bubble growth time predicted by the C-T model with a temperature corrected diffusion coefficient, and the bubble growth time predicted by the C-T model with the constant known value for the diffusion coefficient as a function of temperature. The C-T model prediction with the temperature corrected diffusion coefficient agrees more favorably with the experimentally measured bubble growth time than the prediction made with the constant diffusion coefficient. All three bubble growth times are similar at the intermediate temperature because this temperature is very close to 25°C, which is the temperature that the diffusion coefficient is known. The accompanying plot of the initial mass balance errors in Figure 7-12 confirms that it is more accurate to use temperature corrected diffusion coefficients than the one known value as a constant.

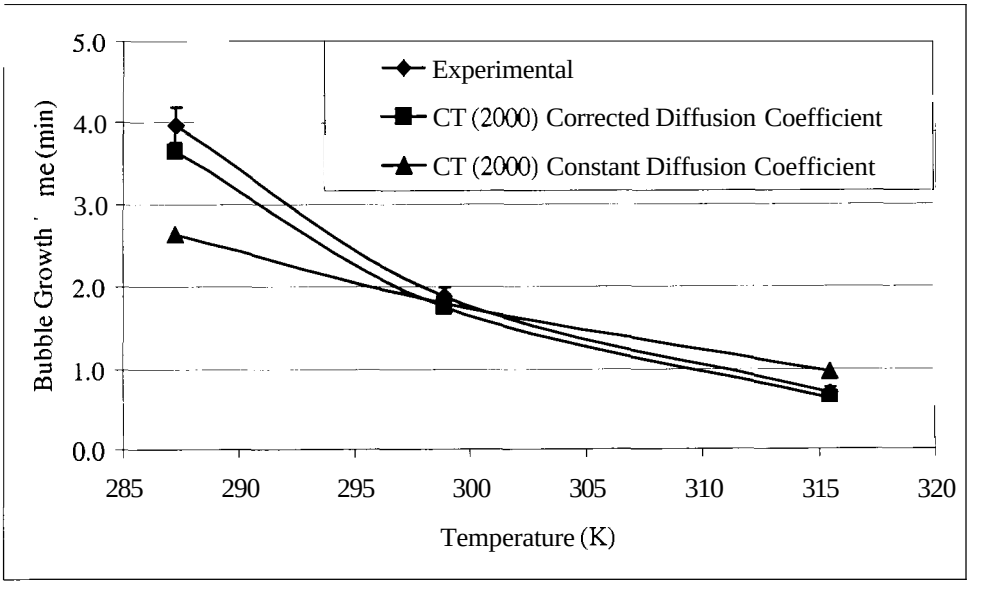

Figure 7-11. Comparison of bubble growth time measured experimentally, bubble growth time predicted by the C-T model with a temperature corrected diffusion coefficient, and bubble growth time predicted by the C-T model with a constant diffusion coefficient as a function of temperature for water saturated with helium at 1400 psig for 5 min.

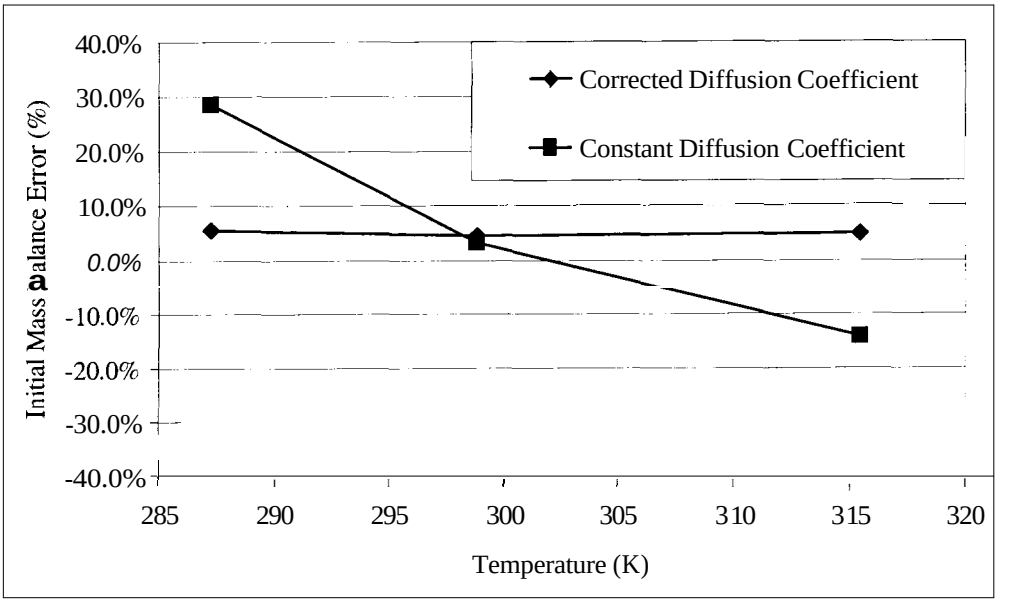

Figure 7-12. Initial mass balances errors for temperature corrected and constant diffusion coefficients in the C-T model as a function of temperature from water saturated with helium at 1400 psig for 5 minutes.

Additional temperature studies involving helium, in which the supersaturation ratio was held constant at a value ~ 32, were performed. Examination of Figures 7-13 and 7-14 shows similar results. The temperature correction technique of diffusion coefficients used in the C-T model provided a better fit of the experimentally measured bubble growth times, than using the one known diffusion coefficient as a constant.

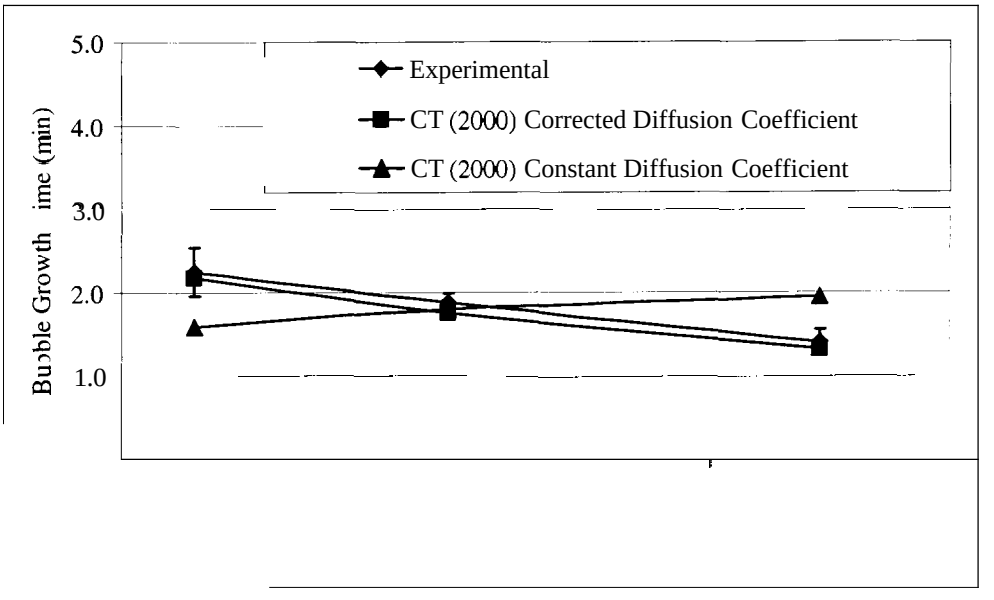

bubble growth time predicted by the C-T model with a temperature corrected diffusion coefficient, and bubble growth time predicted by the C-T model with a constant diffusion coefficient as a function of temperature for water saturated with helium at 1400 psig for saturation times that give a constant supersaturation ratio (~ 32).

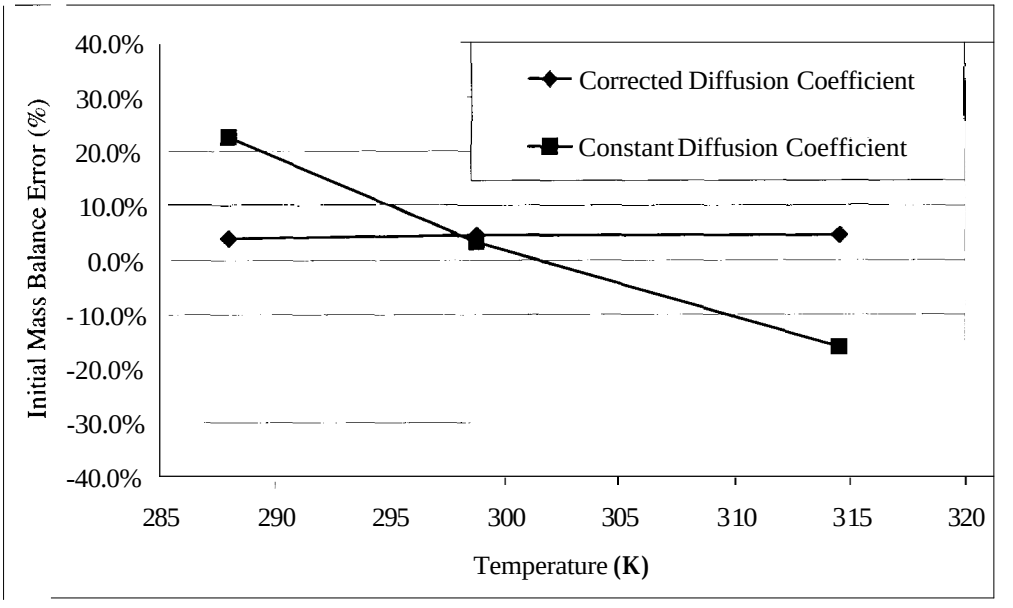

Figure 7-14. Initial mass balances errors for temperature corrected and constant diffusion coefficients in the C-T model as a function of temperature from water saturated with helium at 1400 psig saturation times that give a constant supersaturation ratio (– 32).

7.4 Discussion of Modeling Results

Overall, the C-T model appears to provide the best fit to the experimental data compared to the Manley and Scriven theories. The Manley predictions did follow the appropriate trend, but deviates from the experimentally measured bubble growth times by the greatest amount. This suggests that some combination of both diffusion and convection is responsible for the bubble growth. The Scriven theory provided slightly better predictions of the bubble growth time than the C-T model at some of the lowest supersaturation ratios, but the C-T model was a much better predictor of bubble growth time at the higher supersaturation ratios. At the higher supersaturation ratios, the convective contribution increases and the improvements to the initial bubble surface velocity and the propagation of the bubble surface velocity throughout time, that are present in the C-T model, become increasingly significant. It should also be pointed out that both the Manley and C-T models account for an initial non-zero bubble diameter. Although the Scriven theory is based on an initial bubble diameter of zero, if D_{max}^2 is replaced with $(D_{max}^2 - D_0^2)$, predicted bubble growth times would be lowered by only about 4%. This modification to the Scriven prediction does not account for the discrepancies at the higher supersaturation ratios.

Modeling of the bubble growth from the 50, 200, and 450 μm capillaries all showed similar results. A Laplace pressure equation (see Equation C-6 of Appendix C) was not needed to calculate the pressure inside of bubbles of this size, since the effect was negligible. Table 7-2 shows the pressure inside of a gas bubble at 20°C with an external liquid pressure (P_L) of 1 atm, calculated using a Laplace pressure equation. The pressure inside of a gas bubble is elevated by a Laplace expression, but quickly becomes

negligible. The smallest bubble ever encountered in the capillary experiments was 25 pm, the approximate size of the bubble cap upon detachment from a 50 μm capillary. At this point, the pressure inside the gas bubble would only be 5.7% higher than the assumed value of 1 atm. Bubbles from the 50 μm capillaries grew to sizes approximately 1850 μm in diameter, so there is only a very small fraction of time that the pressure inside the bubble would be more than 1% higher than the assumed value. Due to this reasoning, it was decided to neglect the Laplace pressure effects in the C-T model in order to gain computational speed.

Bubble radius (μm)	Pressure inside gas bubble (atm)
25	1.057
75	1.019
125	1.011
175	1.008
225	1.006

For the partial depressurization experiments, dissolved gas concentrations achieved for the 10, 25, and 40 minute saturation periods with air at 1400 psig were similar to the concentrations achieved before. The supersaturation ratios were significantly lower; however, because the equilibrium dissolved gas concentration at an intermediate pressure would be higher than at atmospheric pressure. Despite the high dissolved gas concentrations, the experimentally measured bubble growth times and

theoretical predictions behaved more like the previous experiments performed at the lower supersaturation ratios. The C-T model provided a better fit to the bubble growth times at the two higher supersaturation ratios in the partial depressurization experiments, but was similar to the Scriven prediction at the lowest supersaturation ratio.

The C-T model proved to be effective at predicting the bubble growth time for different gases dissolved in water. Using air in water, carbon dioxide in water, and helium in water, **a** range of solubilities and diffusivities could be investigated. The air in water and helium in water experiments were most similar in that both the Scriven and C-T models provided similar agreement with the experimentally measured bubble growth time at the lowest supersaturation ratios, but the C-T model proved superior at the higher supersaturation ratios. In the carbon dioxide in water experiments, where bubble growth was significantly faster, the C-T model provided a better fit to the experimentally measured bubble growth times for all four supersaturation ratios investigated.

The temperature correction of diffusion coefficients for use in the C-T model was determined to be more accurate than using the known value of 6.280×10^{-9} m^2/s at 25°C as a constant. It was unfortunate that the literature lacked more diffusion coefficient data as a function of temperature. Han and Bartels (1996) reported experimentally determined diffusion coefficients as a function of temperature for oxygen in water. The same temperature correction technique described in Appendix H.2 is applied to selected data from Han and Bartels (1996) in Table 7-3. This analysis also supports the validity of the diffusion coefficient temperature correction technique employed in this dissertation.

Temperature (°C)	Experimentally Measured Diffusion Coefficient (m^2/s)	Temperature Corrected Diffusion Coefficient (m^2/s)	Percent Difference
14.7	1.550×10^{-9}	1.500×10^{-9}	-3.2%
21.0	1.775×10^{-9}	1.793×10^{-9}	+1.0%
26.2	2.090×10^{-9}	2.090×10^{-9} (base **point)**	–
35.1	2.520×10^{-9}	2.588×10^{-9}	+2.7%
45.1	3.050×10^{-9}	3.144×10^{-9}	+3.1%

8. Conclusions

The presence of Harvey Nuclei was responsible for the bubble formation that occurred in the soda bottle experiments. The regular cyclical pattern of bubble production at specific sites in the walls of the glass soda bottles can only be explained by pre-existing gas trapped at a location on the interior surface of the bottle. CNT predicted that bubble formation could occur in a conical cavity at similar supersaturation levels, but the regular cyclical pattern of bubble production would not be expected from a process like CNT, which involves random statistical fluctuations. Visual evidence supported the fact that bubble formation from the container walls of glass soda bottles came from locations that appeared to have a very small cavity or geometric defect in the bottle surface. Also, the fact that these locations could be de-activated by improving the wetting characteristics and re-activated by re-seeding the surface with a gas further confirms that the Harvey Nuclei mechanism applies. CNT cannot be completely ruled out. It is possible that CNT still has some usefulness in describing the behavior at very high supersaturation ratios (greater than 1000) and in describing the behavior of perfectly wetted conical cavities of very specific geometry. For most common industrial processes and everyday situations, it appears that the presence of pre-existing gas is most critical in whether or not bubble formation will occur in supersaturated liquid solutions.

The experimental apparatus proved to be effective for studying the behavior of a series of bubbles growing at an artificial capillary, which functioned as Harvey Nuclei when seeded with an air bubble. Bubble detachment diameter varied little from bubble to bubble. Bubble growth times tended to increase as the dissolved gas concentration decreased. Upon detachment, the bubble was observed to leave part of itself behind in

the neck of the capillary. This bubble remnant would continue to grow due to the surrounding supersaturated solution. The appearance of a "nucleation" lapse time was explained by an inability to see the bubble remnant until it became larger than the site opening when viewed from above. The term "nucleation" lapse time was identified as a misnomer, since the presence of a bubble remnant implies a non-zero initial size. One study was conducted, redefining the "nucleation" lapse time as the time required for the bubble remnant to become larger than the site opening, for comparison with previous research. "Nucleation" lapse times were dropped from further consideration, since they were determined to be an experimental artifact in that the bubble cap cannot be seen until it becomes larger than the capillary opening. Further analysis was concerned only with the bubble growth time, or the time between consecutive bubble detachments.

While the long term studies of bubble growth from artificial capillaries were helpful in better understanding bubble behavior of partially wetted capillaries, analysis of first full bubble only data proved to be more valuable for studying the effects of increased supersaturation ratio. Similar bubble growth behavior was observed at a 450 μm capillary with air dissolved in water compared to a repeated trial under identical conditions, and a third trial with an altered saturation routine. Bubble growth times were longer for larger capillaries. Bubble growth times were also longer in an experiment involving a partial depressurization to an intermediate pressure. Carbon dioxide in water resulted in much faster bubble growth because of the much greater solubility than air in water, while helium in water, with higher diffusion coefficient, but lower solubility, resulted in only slightly longer bubble growth times than air in water.

The C-T model provided more accurate predictions of the bubble growth time than both the Manley and Scriven theories. Some combination of diffusion and convection is responsible for the bubble growth in supersaturated liquid solutions since the diffusion only solution of Manley provided the least accurate fit the experimentally measured bubble growth times. In some instances, the Scriven theory was more accurate than the C-T model at the lowest supersaturation ratios, but the C-T model always provided a superior fit at the higher supersaturation ratios. The improvements to the initial bubble surface velocity and the propagation of the bubble surface velocity throughout time, present in the C-T model, became increasingly important at the higher supersaturation ratios. The C-T model accurately accounted for bubble growth from artificial capillaries for three different sizes, an altered supersaturation routine, a partial depressurization, and carbon dioxide and helium in place of air as the saturating gas. Temperature adjusted studies involving helium dissolved in water verified the applicability of using a temperature correction technique for the diffusion coefficient.

9. Recommendations

Considering that the difference between bubble formation due to CNT and bubble formation from Harvey nuclei is now more clearly understood, further work in this area will be guided by this knowledge. Some interesting observations were made during the soda bottle experiments described in chapter 3, but it remains more advantageous to study bubble formation and growth phenomena in a more controlled experimental setting, where bubbles form at known artificial sites. Artificial Harvey nuclei have been successfully made, but future work could be performed to see if bubbles will indeed form in completely wetted conical cavities with the geometries described by Wilt (1986).

A few modifications could be made to the apparatus described in chapter 4. The bottom interior surface of the test cell could have been made smoother by boring the central core completely through the main body of the stainless steel block and attaching a removable smooth and flat bottom to the test cell. Having a smoother bottom would help minimize interfering bubbles rising from the bottom of the cell because fewer gases would become trapped on a smoother surface. The apparatus could also be equipped with a built-in temperature monitoring and control system, Although the employed temperature correction techniques proved to be accurate, further gains in agreement between experimental and predicted bubble growth times will be aided by controlling the temperature of the test cell contents. Finally, higher test cell pressures could be investigated by using a High Pressure Generator (High Pressure Equipment Company, Erie, **PA).** This device is a manually operated piston screw pump that could boost the pressure of the contents of the test cell to pressures as high as 60,000 psig. A completely new test cell would have to be designed with thicker walls, a smaller diameter but much

larger in thickness sapphire window, and a new technique for saturating liquid solutions with gases in this device. Higher supersaturation ratios could be achieved with these modifications.

Beyond investigating different gases and liquids with the experimental apparatus, a new type of experiment involving evacuation of the test cell contents could be performed. Depressurization to pressures less than one atmosphere absolute pressure is another technique for creating a supersaturated solution.

The C-T model proved versatile in predicting bubble growth times for the experimental situations studied. For experiments involving bubbles with diameters less than 50 μm, a Laplace pressure equation could be incorporated to determine the pressure and therefore the concentration of gas inside the bubble. As computers with microprocessors faster than 400 MHz become readily available, both the accuracy and/or length of time for the program to execute can be improved.

In completely new types of experimental work, the effect that the growing bubble has on the surrounding supersaturated solution can be investigated. Finding methods for measuring the dissolved gas concentration profile or the velocity profile in the liquid immediately surrounding the bubble would both be significant contributions to the literature. A logical extension of the experimental work is to also study the formation and growth of gas bubbles in flowing supersaturated solutions, since this would have industrial significance.

New mathematical modeling describing the effect of turbulence and flow situations on bubble formation and growth would be valued. Many complicated flow patterns undoubtedly influence bubble formation and growth characteristics in actual

turbulence and flow situations. Perhaps the earliest models could be made to study the influence of a solitary nearby pressure disturbance and how it alone would affect the formation of a nearby gas phase.

References

Apfel, R.E. (1970). The Role of Impurities in Cavitation-Threshold Determination. *The Journal of the Acoustical Society of America.* **48**(5, part 2): 1179-1186.

Bankoff, S.G. (1958). Entrapment of Gas in the Spreading of a Liquid Over a Rough Surface. *AIChE Journal.* **4**(1): 24-26.

Bankoff, S.G. (1966). Diffusion-Controlled Bubble Growth. *Advances in Chemical Engineering.* **6:** 1-60.

Barlow, E.J. and Langlois, W.E. (1962). Diffusion of Gas from a Liquid into an Expanding Bubble. IBM Journal. July. pp. 329-337.

Bernath, L. (1952). Theory of Bubble Formation in Liquids. *Industrial and Engineering Chemistry.* June. **44**(6): 1310-1313.

Bisperink, C.G.J. and Prins, A. (1994). Bubble growth in carbonated liquids. *Colloids and Surfaces A: Physicochemical and Engineering Aspects.* **85:** 237-253.

Blander, M. and Katz, J.L. (1975). Bubble Nucleation in Liquids. *AIChE Journal.* **21**(5): 833-848.

Blinkov, V.N., Jones, O.C., and Nigrnatulin, B.I. (1993). Nucleation and Flashing in Nozzles—2. *International Journal of Multiphase Flow.* 19(6): 965-986.

Bowers, P.G., Bar-Eli, K., Noyes, R.M. (1996). Unstable supersaturated solutions of gases in liquids and nucleation theory. *Journal of the Chemical Society: Faraday Transactions.* 92(16): 2843-2849.

Bowers, P.G., Hofstetter, C., Letter, C.R., and Toomey, R.T. (1995). Supersaturation Limit for Homogeneous Nucleation of Oxygen Bubbles in Water at Elevated Pressure: "Superhenry's Law". *Journal of Physical Chemistry.* **99**(23): 9632-9637.

Buehl, W.M. and Westwater, J.W. (1966). Bubble Growth by Dissolution: Influence of Contact Angle. *AIChE Journal.* **12**(3): 571-576.

Byers, H.R. (1965). Nucleation in the Atmosphere. *Industrial and Engineering Chemistry.* November. **57(**11): 32-40.

Carnahan, B, Luther, H.A., and Wilkes, J.O. (1969). *Applied Numerical Methods.* John Wiley and Sons, New York.

Cha, Y.S. and Henry, R.E. (1981). Bubble Growth During Decompression of a Liquid. *Journal of Heat Transfer.* February. 103: 56-60.

Ciholas, P.A. and Wilt, P.M. (1988). Nucleation Rates in Water-Carbon Dioxide Solutions: The Spherical Cavity Case. *Journal of Colloid and Interface Science.* **123**(1): 296-298.

Dean, R.B. (1944). The Formation of Bubbles. *Journal of Applied Physics.* May. **15:** 446-451.

Domnick, J. and Durst, F. (1995). Measurement of Bubble Size, Velocity, and Concentration in Flashing Flow Behind a Sudden Constriction. *International Journal of Multiphase Flow.* **21**(6): 1047-1062.

Eddington, R.I. and Kenning, D.B.R. (1979). The Effect of Contact Angle on Bubble Nucleation. *International Journal of Heat and Mass Transfer.* **22:** 1231-1236.

Eller, A.I. (1969). Growth of Bubbles by Rectified Diffusion. *The Journal of the Acoustical Society of America.* **46**(5, part 2): 1246-1250.

Epstein, P.S. and Plesset, M.S. (1950). On the Stability of Gas Bubbles in Liquid-Gas Solutions. *The Journal of Chemical Physics.* November **18**(11): 1505-1509.

Ferrell, R.T. and Himmelblau, D.M. (1967). Diffusion Coefficients of Hydrogen and Helium in Water. *AIChE Journal.* July. **13**(4): 702-708.

Finch, J.A. and Smith, G.W. (1979). Contact Angle and Wetting. *Minerals Science Engineering.* **11(**1): 36-63.

Fyrillas, M.M. and Szeri, A.J. (1994). Dissolution or growth of soluble spherical oscillating bubbles. *Journal of Fluid Mechanics.* 277: 381-407.

Geankoplis, C.J. (1983). *Transport Processes and Unit Operations, Second Edition.* Boston: Allyn and Bacon, Inc.

Gerth, W.A. and Hemmingsen, E.A. (1980). Heterogeneous nucleation of bubbles at solid surfaces in gas-supersaturated aqueous solutions. *Journal of Colloid and Interface Science.* 74(1): 80-89.

Ginn, M.E., Noyes, C.M., Jungermann, E. (1968). The Contact Angle of Water on Viable Human Skin. *Journal of Colloid and Interface Science.* 26: 146-151.

Glas, J.P. and Westwater, J.W. (1964). Measurements of the Growth of Electrolytic Bubbles. *International Journal of Heat Transfer.* **7:** 1427-1443.

Good, W.R. (1973). A Comparison of Contact Angle Interpretations. *Journal of Colloid and Interface Science.* 44(1): 63-71.

Hamilton, W.C. (1972). A Technique for the Characterization of Hydrophilic Solid Surfaces. *Journal of Colloid and Interface Science.* **40**(2): 219-222.

Han, P. and Bartels, D.M. (1996). Temperature Dependence of Oxygen Diffusion in H2O and D2O. *Journal of Physical Chemistry.* **100**(13): 5597-5602.

Harvey, E.N., Barnes, D.K., McElroy, W.D., Whiteley, A.H., Pease, D.C., and Cooper, K.W. (1944a). Bubble Formation in Animals, I. Physical Factors. *Journal of Cellular and Comparative Physiology.* August. 24(1): 1-22.

Harvey, E.N., Barnes, D.K., McElroy, W.D., and Whiteley, A.H. (1947). On Cavity Formation in Water. *Journal of Applied Physics.* February. 18: 162-172.

Harvey, E.N., Whiteley, A.H., McElroy, W.D., Pease, D.C., and Barnes, D.K. (1944b). Bubble Formation in Animals, II. Gas Nuclei and Their Distribution in Blood and Tissues. *Journal of Cellular and Comparative Physiology.* August. 24(1): 23-34.

Hemmingsen, E.A. (1975). Cavitation in Gas-Supersaturated Solutions. *Journal of Applied Physics.* January. **46**(1): 213-218.

Hill, T.L. (1963). Thermodynamics of Small Systems, Part 1. New York: W.A. Benjamin, Inc., Publishers.

Hill, T.L. (1964). Thermodynamics of Small Systems, Part 2. New York: W.A. Benjamin, Inc., Publishers.

Hirth, J.P., Pound, G.M., and St. Pierre, G.R. (1970). Bubble Nucleation. *Metallurgical Transactions.* April. 1: 939-945.

Jackson, M.L. (1994). Energy Effects in Bubble Nucleation. *Industrial Engineering Chemistry and Research.* **33**(4): 929-933.

Jones, O.C. and Zuber, N. (1978). Bubble Growth in Variable Pressure Fields. *Journal of Heat Transfer.* August. 100: 453-459.

Jones, S.F., Evans, G.M., and Galvin, K.P. (1999a). Bubble nucleation from gas cavities – a review. *Advances in Colloid and Interface Science.* **80:** 27-50.

Jones, S.F., Evans, G.M., and Galvin, K.P. (1999b). The cycle of bubble production from a gas cavity in a supersaturated solution. *Advances in Colloid and Interface Science.* **80:** 51-84.

Jones, S.F., Galvin, K.P., Evans, G.M., and Jameson, G.J. (1998). Carbonated water: The physics of the cycle of bubble production. *Chemical Engineering Science.* **53(** 1): 169-173.

Keller, A. (1972). The Influence of the Cavitation Nucleus Spectrum on Cavitation Inception, Investigated with a Scattered Light Counting Method. *Journal of Basic Engineering.* December. pp. 917-925.

Kemmer, F.N. (1988). *The Nalco Water Handbook, Second Edition.* New York: McGraw-Hill Book Company.

Kendoush, A.A. (1989). The delay time during depressurization of saturated water. *Znternational Journal of Heat and Mass Transfer.* 32(11): 2149-2154.

Kenrick, F.B., Wismer, K.L., and Wyatt, K.S. (1924). Supersaturation of Gases in Liquids. *Journal of Physical Chemistry.* 28: 1308-1315.

Li, X. and Yortsos, Y.C. (1995). Visualization and Simulation of Bubble Growth in Pore Networks. *AIChE Journal.* February, **41**(2): 214-222.

Liebermann, L. (1957). Air Bubbles in Water. *Journal of Applied Physics.* February. **28**(2): 205-211.

Liger-Belair, G., Marchal, R., Robillard, B., Dambrouck, T., Maujean, A., Vignes-Adler, M., and Jeandet, P. (2000). On the Velocity of Expanding Spherical Gas Bubbles Rising in Line in Supersaturated Hydroalcoholic Solutions: Application to Bubble Trains in Carbonated Beverages. *Langmuir.* 16: 1889-1895.

Lothe, J. and Pound, G.M. (1962). Reconsiderations of Nucleation Theory. *The Journal of Chemical Physics.* April. **36**(8): 2080-2085.

Lubetlun, S.D. (1995). The Fundamentals of Bubble Evolution. *Chemical Society Reviews.* pp. 243-250.

Lubetkin, **S.** and Blackwell, M. (1988). The Nucleation of Bubbles in Supersaturated Solutions. *Journal of Colloid and Interface Science.* **26**(2): 610-615.

Manley, D.M.J.P. (1960). Change in size of air bubbles in water containing a small dissolved air content. *British Journal of Applied Physics.* January. **11:**38-42.

McDonald, J.E. (1962). Homogeneous Nucleation of Vapor Condensation. I. Thermodynamic Aspects. *American Journal of Physics.* 30: 870-877.

McDonald, J.E. (1963). Homogeneous Nucleation of Vapor Condensation. I. Kinetic Aspects. *American Journal of Physics.* 31: 31-41.

Neumann, A.W., Harnoy, **Y.,** Stanga, D., Rapacchietta, A.V. (1976). Temperature Dependence of Contact Angles on Polyethylene Terephthalate. *Colloid and*

Interface Science: Proceedings of the 50th International Conference on Colloids and Surfaces. New York: Academic Press, Inc. pp. 301-312.

Pease, D.C. and Blinks, L.R. (1947). Cavitation from Solid Surfaces in the Absence of Gas Nuclei. *Journal of Physical and Colloid Chemistry.* 51: 556-567.

Riznic, J.R. and Ishii, M. (1989). Bubble number density and vapor generation in flashing flow. *International Journal of Heat and Mass Transfer.* **32**(10): 1821-1833.

Rubin, M.B. and Noyes, R.M. (1987). Measurements of Critical Supersaturation for Homogeneous Nucleation of Bubbles. *Journal of Physical Chemistry.* 91(15): 4193-4198.

Ryan, W.L. (1991). *An analysis of the role of hydrophobic surfaces and crevices in bubble formation at low gas supersaturation.* Ph.D. Thesis, University of California, SD.

Ryan, W.L. and Hemmingsen, E.A. (1993). Bubble Formation in Water at Smooth Hydrophobic Surfaces. *Journal of Colloid and Interface Science.* **157:** 312-317.

Ryffel, H.H. (1984). *Machinery's Handbook, 22nd Revised Edition.* New York: Industrial Press, Inc. pp. 324-331.

Scriven, L.E. (1959). On the dynamics of phase growth. *Chemical Engineering Science.* **10**(1/2): 1-13.

Shaffer, M.M. (1981). *Foam Coatings Produced by a Dissolved Vapor Technique.* M.S. Thesis, University of Maine.

Strey, R., Wagner, P.E., and Viisanen, Y. (1994). The Problem of Measuring Homogeneous Nucleation Rates and the Molecular Contents of Nuclei: Progress in the Form of Nucleation Pulse Measurements. *Journal of Physical Chemistry.* **98**(32): 7748-7758.

Takahashi, T., Miyahara, T., and Mochizuki, H. (1979). Fundamental Study of Bubble Formation in Dissolved Air Pressure Flotation. *Journal of Chemical Engineering of Japan.* **12**(4): 275-280.

Tao, L.N. (1978). Dynamics of growth or dissolution of a gas bubble. *Journal of Chemical Physics.* November. **69**(9): **4**189-4194.

Theofanous, T., Biasi, L., Isbin, H.S., and Fauske, H. (1969). A theoretical study on bubble growth in constant and time-dependent pressure fields. *Chemical Engineering Science.* 24: 885-897.

Toda, S. and Kitamura, M. (1983). Bubble Growth in Decompression Fields. *ASME-JSME Thermal Engineering Joint Conference Proceedings.* 3: 395-402.

Tucker, A.S. and Ward, C.A. (1975). Critical State of Bubbles in Liquid-Gas Solutions. *Journal of Applied Physics.* November. **46**(11): 4801-4808.

Venerus, D.C. and Yala, N. (1997). Transport Analysis of Diffusion-Induced Bubble Growth and Collapse in Viscous Liquids. *AZChE Journal.* November. **43**(11): 2948-2959.

Vivian, J.E. and King, C.J. (1964). Diffusivities of Slightly Soluble Gases in Water. *AZChE Journal.* March. **10**(2): 220-221.

Ward, C.A., Balakrishnan, A., and Hooper, F.C. (1970). On the Thermodynamics of Nucleation in Weak Gas-Liquid Solutions. *Journal of Basic Engineering.* December. pp. 695-704.

Ward, C.A., Johnson, W.R., Venter, R.D., and Ho, S. (1983). Heterogeneous bubble nucleation and conditions for growth in a liquid-gas system of constant mass and volume. *Journal of Applied Physics.* **54**(4): 1833-1843.

Weast, R.C. (1975). *CRC Handbook of Chemistry and Physics, 56th Edition.* Cleveland: CRC Press. pp. F-41,F-43.

Weatherford, W.D. (1970). Homogeneous Nucleation of Gas Bubbles in Liquids. *Journal of Colloid and Interface Science.* October. **34**(2): 197-204.

Wilke, C.R. and Chang, P. (1955). Correlation of Diffusion Coefficients in Dilute Solutions. *AZChE Journal.* June. **1**(2): 264-270.

Wilt, P.M. (1986). Nucleation Rates and Bubble Stability in Water-Carbon Dioxide Solutions. *Journal of Colloid and Interface Science.* **112**(2): 530-538.

Winterton, R.H.S. (1977). Nucleation of boiling and cavitation. *Journal of Physics D.* **10**: 2041-2056.

Yount, D.E. and Strauss, R.H. (1976). Bubble formation in gelatin: A model for decompression sickness. *Journal of Applied Physics.* November. **47**(11): 5081-5089.

Zettlemoyer, A.C. (1969). *Nucleation.* New York: Marcel Dekker, Inc.

Zhou, Z.A., Xu, Z., and Finch, J.A. (1998). Effect of Surface Properties of Fine Particles on Dynamic Bubble Formation in Gas-Supersaturated Systems. *Zndustrial Engineering Chemistry Research.* **37**(5): 1998-2004.

Appendices

Appendix A: Notation Used

The following is a complete list of all of the notation used throughout this dissertation. The only exceptions are in Appendix F and Appendix G where the use of subscripts, superscripts, and Greek letters had to be altered for use in the Mathcad and FORTRAN programs. All variables used in the two programs are defined in comment lines in each program itself.

A_{LG} surface area of liquid-gas interface
A_{SG} surface area of solid-gas interface
B correction factor in the pre-exponential term of nucleation rate expressions
C_A concentration of species **A,** the dissolved gas
C_{A0} initial bulk dissolved gas concentration
C_{AS} saturated OR equilibrium dissolved gas concentration
c proportionality constant
D bubble diameter
D_0 first observable bubble size OR initial bubble diameter (taken as capillary inside diameter)
D_{max} bubble detachment diameter
D_{AB} diffusion coefficient of gas **A** in liquid *B*
G_{1a} a contact angle correction factor for heterogeneous nucleation at a smooth planar interface
G_{1b} a geometric volume correction factor for heterogeneous nucleation at a smooth planar interface
G_{2a} a contact angle and cone semi-vertex angle correction factor for heterogeneous nucleation in a conical cavity
G_{2b} a geometric volume correction factor for heterogeneous nucleation in a conical cavity
G_{3a} a contact angle and cone semi-vertex angle correction factor for heterogeneous nucleation on a conical projection
G_{3b} a geometric volume correction factor for heterogeneous nucleation on a conical projection
J nucleation rate
k Boltzman constant (gas constant on a molecule basis)
m mass of a gas molecule
MBE mass balance error
MW molecular weight of solute
N number of molecules per unit volume
n number of bubbles per unit volume containing X molecules for homogeneous nucleation OR number of bubbles per unit area containing X molecules for heterogeneous nucleation

P_G	pressure inside a gas bubble of radius R
P_L	pressure of external liquid phase
P_S	saturation pressure **AND** pressure inside of a critically sized bubble
R	radius of gas bubble OR radius of curvature of gas bubble
R_C	radius of a critically sized bubble
R_{IG}	ideal gas constant on a mole basis
R_P	projected bubble radius
$\dot{R}$	bubble surface velocity (= dR/dt)
r	radial coordinate
SSR	supersaturation ratio
T	temperature
t	time
t_{CT}	bubble growth time predicted by the C-T model
t_G	bubble growth time
t_M	bubble growth time predicted by the Manley model
t_S	bubble growth time predicted by the Scriven model
V_G	volume of gas bubble
VOL	volume of gas released after running magnetic stir bar
x	number of gas molecules in bubble
x_C	number of gas molecules in a critically sized nucleus
Z	Zeldovich correction factor
z	defined by Figure C-1
α	pre-exponential kinetic rate factor
β	dimensionless growth parameter defined by Scriven (1959)
β'	rate per unit area at which molecules strike the surface
ε	simplifying substitution (= $1-\rho_G/\rho_L$)
ΔF	free energy change
ΔF_C	critical free energy change
Δh	height difference on the air and helium gas collection tube used to determine the dissolved gas concentration of the sample in the test cell
Δt_n	"nucleation" lapse time
ϕ	dimensionless supersaturation parameter defined by Scriven (1959)
μ_G	molecular chemical potential of the gas phase
μ_L	molecular chemical potential of the liquid phase
μ_W	viscosity of water
ρ_G	density of gas phase
ρ_L	density of liquid phase
σ_{LG}	surface tension at liquid-gas interface
σ_{SG}	surface tension at solid-gas interface
σ_{SL}	surface tension at solid-liquid interface
θ	contact angle
ω	cone semi-vertex angle
ξ	simplifying substitution (=z/R)

Appendix B: Soda Bottle Raw Data

Table B-1. First Observable Bubble Size (D_0), Detachment Diameter (D_{max}), "Nucleation" Lapse Time (Δt_n), and Bubble Growth Time (t_G) Data for all Soda Bottle Experiments in Addition to the Buehl and Westwater (1966) Data

Trial	D_0 (μm)	D_{max} (μm)	Δt_n (ms)	t_G (ms)
#1 (15 min)	50.2 ± 3.9	208.8 ± 6.6	461.2 ± 1.6	195.7 ± 1.2
#2 (15 min)	25.4f5.7	106.6 ± 1.3	67.0f2.0	28.0f0.0
#2 (45 min)	21.3 ± 1.8	104.1 ± 2.5	85.3 ± 2.6	37.3 ± 3.2
#3 (15 min)	26.9 ± 0.0	365.6 ± 10.5	446.0 ± 3.9	762.0 ± 3.9
#4 (15 min)	32.5 ± 2.4	523.8 ± 2.4	181.3 ± 6.9	1484.0 ± 0.0
#5 (15 min)	26.2 ± 1.3	362.9 ± 0.0	378.0 ± 0.0	710.7 ± 1.3
#6 (15 min)	27.9 ± 3.6	382.5 ± 0.0	364.0 ± 0.0	848.0 ± 0.0
#7 (15 min)	36.5 ± 1.9	600.6 ± 6.5	125.6 ± 1.9	1506.0 ± 0.0
#7 (re-10 days)	29.3 ± 1.5	607.5 ± 0.0	338.7 ± 11.1	5083.5 ± 1.0
#8 (15 min)	47.7 ± 5.6	259.4 ± 1.6	375.0 ± 4.9	287.5 ± 4.3
#8 (re-10 days)	29.2 ± 1.6	340.8 ± 3.3	788.7 ± 11.1	2450.0 ± 0.0
#9 (15 min)	32.8 ± 5.5	274.5 ± 4.6	579.7 ± 6.8	355.9 ± 3.8
#9 (30 min)	25.0 ± 2.7	283.3 ± 1.0	558.0 ± 2.0	364.5 ± 0.6
#9 (1 hr)	26.6 ± 1.7	294.1 ± 1.2	483.3 ± 0.7	393.6 ± 0.5
#9 (1.5 hrs)	24.8 ± 1.7	295.7 ± 0.0	479.5 ± 1.0	392.7 ± 0.7
#9 (2 hrs)	20.8 ± 0.9	295.7 ± 0.0	476.0 ± 0.0	392.0 ± 0.0
#9 (5.5 hrs)	24.6 ± 2.1	295.7 f 0.0	640.0 ± 0.0	575.7 f 0.7
#9 (19.5 hrs)	26.9 ± 3.8	322.4 ± 1.1	758.8 ± 8.2	1073.3 ± 17.1
#9 (24 hrs)	24.4 ± 1.5	322.1 ± 0.7	824.2 ± 5.2	1179.4 ± 9.8
#9 (48 hrs)	27.7 ± 1.6	325.3 ± 3.3	1664.3 ± 53.7	2075.5 ± 27.1
#9 (72 hrs)	26.2 ± 1.7	329.3 ± 2.6	2962.8 ± 69.8	2654.0 ± 27.5
#9 (96 hrs)	26.3 ± 4.2	311.3 ± 0.0	10.03s f 0.11 s	3667.5 ± 47.4
B&W (1966)	771.4 f 367.4	2394.3 ± 235.2	6561.1 ± 4233.6	12.19s ± 6.99 s

Appendix C: Derivation of Classical Nucleation Theory Expressions

C.1 Homogenous Nucleation

This appendix attempts to compile the most complete derivation of the nucleation rate expressions in Classical Nucleation Theory (CNT). Most previous theoretical treatments [Zettlemoyer (1969), Ward *et al.* (1970), and Blander and Katz (1975)] begin with a derivation of the work required to form a bubble or the change in free energy as a result of the formation of a bubble nucleus. This work requirement is equivalent to the free energy change, and this free energy change is,

$$\Delta F = \sigma_{LG} \cdot A_{LG} - (P_G - P_L) \cdot V_G + x \cdot (\mu_G - \mu_L), \qquad \text{(C-1)}$$

where ***AF*** is the change in free energy, σ_{LG} is the surface tension at the liquid-gas interface, A_{LG} is the surface area of the bubble, P_G is the pressure inside the gas bubble, P_L is the pressure in the external liquid phase, V_G is the volume of the gas bubble, x is the number of gas molecules inside the bubble, and μ_G and μ_L represent the gas and liquid chemical potentials, respectively. The change in free energy expression in Equation C-1 applies to a homogeneous nucleation where a single gas bubble forms in a bulk liquid phase.

Since the change in free energy is often plotted **as** a function of the bubble radius *(R)*, it is desirable to express the entire right hand side of Equation C-1 completely in terms of *R*. Equations C-2 through C-7 help accomplish this.

Surface area of gas bubble:
$$A_{LG} = 4 \cdot \pi \cdot R^2 \qquad \text{(C-2)}$$

Volume of gas bubble:
$$V_G = \frac{4}{3} \cdot \pi \cdot R^3 \qquad \text{(C-3)}$$

Chemical potential difference: $$\mu_G - \mu_L = k \cdot T \cdot ln\left(\frac{P_L + \frac{2 \cdot \sigma_{LG}}{R}}{P_S} \right) \quad \text{(C-4)}$$

Ideal gas law: $$x \cdot k \cdot T = \left(P_L + \frac{2 \cdot \sigma_{LG}}{R} \right) \cdot \frac{4}{3} \cdot \pi \cdot R^3 \quad \text{(C-5)}$$

Laplace Equation #1: $$P_G = P_L + \frac{2 \cdot \sigma_{LG}}{R} \quad \text{(C-6)}$$

Laplace Equation ***#2:*** $$P_S = P_L + \frac{2 \cdot \sigma_{LG}}{R_C} \quad \text{(C-7)}$$

New variables introduced here are the Boltzman constant ***(k),*** the absolute temperature (T), the saturation pressure/pressure inside a critically sized bubble (P_S), and the radius of a critically sized bubble (R_C). Equation C-7 is really a special case of Equation C-6 with the bubble radius equal to the critical radius.

If Equation C-6 is rearranged, Equation C-8 can be obtained. This equation will be used in a later substitution into Equation C-1.

$$-(P_G - P_L) = \frac{-2 \cdot \sigma_{LG}}{R} \quad \text{(C-8)}$$

Next, if we multiply both sides of the chemical potential difference equation (Equation C-4) by x, we then obtain,

$$x \cdot (\mu_G - \mu_L) = x \cdot k \cdot T \cdot ln\left(\frac{P_L + \frac{2 \cdot \sigma_{LG}}{R}}{P_S} \right). \quad \text{(C-9)}$$

Using the ideal gas law (Equation C-5), the $x \cdot k \cdot T$ term can be substituted for to obtain

$$x \cdot (\mu_G - \mu_L) = \left(P_L + \frac{2 \cdot \sigma_{LG}}{R} \right) \left| \frac{P_L + \frac{2 \cdot \sigma_{LG}}{R}}{P_S} \right| \qquad \text{(C-10)}$$

To obtain an expression for the free energy change in terms of the bubble radius, Equations C-2, C-3, C-8, and C-10 can be substituted into Equation C-1 to obtain,

$$\Delta F_{LG} = \left(P_L + \frac{2 \cdot \sigma_{LG}}{R} \right) R \left| \frac{P_L + \frac{2 \cdot \sigma_{LG}}{R}}{P_S} \right| \qquad \text{(C-11)}$$

When the bubble radius equals the critical radius ($R = R_C$), the free energy change is equivalent to the critical free energy change ($\Delta F = \Delta F_C$). At the critical conditions, ΔF is a maximum and $d(\Delta F)/dR = 0$.

Next, it will be shown that Laplace Equation #2 (Equation C-7), which defines the critical bubble radius, is mathematically consistent with the fact that $d(\Delta F)/dR = 0$ when $R = R_C$. First we will take the partial derivative of Equation C-11 with respect to the bubble radius to obtain,

$$\frac{\partial(\Delta F)}{\partial R} = \frac{8}{3} \cdot \pi \cdot R \cdot \sigma_{LG} + \left(P_L \cdot 4 \cdot \pi \cdot R^2 + \frac{16}{3} \cdot \pi \cdot R \cdot \sigma_{LG} \right) \cdot ln \left(\frac{P_L + \frac{2 \cdot \sigma_{LG}}{R}}{P_S} \right) \cdot$$

$$\ldots \; - \frac{8}{3} \cdot \pi \cdot \sigma_{LG} \cdot \left(\frac{P_L \cdot R + 2 \cdot \sigma_{LG}}{P_L + \frac{2 \cdot \sigma_{LG}}{R}} \right). \qquad \text{(C-12)}$$

If the left-hand side of Equation C-12 is set equal to zero, solving for R would give a value for the critical radius. This equation cannot be explicitly solved for R, so Equation C-7 will be substituted into the right-hand side of Equation C-12 instead. When

the left hand side of Equation C-12 is set equal to zero and Equation C-7 is used to substitute for R, Equation C-12 is satisfied, thus verifying that it is mathematically consistent to say that Equation C-7 provides the appropriate solution at the critical conditions.

The critical free energy change (ΔF_C) can be found by evaluating Equation C-11 at $R = R_C$. By also making use of Equation C-7, which does apply at the critical conditions, Equation C-11 can be simplified to,

$$\Delta F_C = \frac{4}{3} \cdot \pi \cdot R_C^2 \cdot \sigma_{LG} . \tag{C-13}$$

Prediction of nucleation rates has always been the ultimate goal of CNT. It is often stated that CNT is a combination of both the thermodynamics and kinetics of bubble nucleation. This is because the thermodynamic potential required for bubble formation, ΔF_C, becomes an activation parameter for the kinetics describing the nucleation rate (J). Nucleation rates have the dimensions of the number of nucleations per unit volume per unit time for homogenous nucleation (this changes to an area basis for cases involving heterogeneous nucleation). The expected form of a nucleation rate expression is,

$$J = \alpha \cdot exp\left(\frac{-\Delta F_C}{k \cdot T} \right), \tag{C-14}$$

where the pre-exponential factor (α) is calculated from the rate of encounters of dissolved gas with the incipient nucleus. To arrive at the expected form of the nucleation rate expression in Equation C-14, the derivation for nucleation rate expressions [Wilt (1986)] starts with ,

$$J = \frac{\beta'}{\int_{1}^{\infty} (n \cdot A_{LG})^{-1} \cdot dx} , \tag{C-15}$$

where β' is defined as the rate per unit area at which molecules strike the bubble surface and n represents the number of bubbles per unit volume containing x molecules for homogeneous nucleation or the number of bubbles per unit area containing x molecules for heterogeneous nucleation. Wilt provides further definitions for β' and n which are,

$$\beta' = \frac{P_S}{\sqrt{2 \cdot \pi \cdot m \cdot k \cdot T}} , \tag{C-16}$$

$$n = N \cdot exp\left(\frac{-\Delta F_C}{k \cdot T} \right) , \tag{C-17}$$

where m is the mass of one gas molecule and N is the number of molecules per unit volume. N is replaced with $N^{2/3}$ for heterogeneous nucleation situations.

An approximate solution to Equation C-15 is,

$$J = Z \cdot \beta' \cdot A_{LG}(x_C) \cdot n . \tag{C-18}$$

According to Zettlemoyer (1969), the Zeldovich Correction Factor (Z) is defined by Equation C-19. Also, $A_G(x_C)$ is the surface area of a critically sized bubble.

$$Z = \left(\frac{\Delta F_C}{3 \cdot \pi \cdot k \cdot T \cdot x_C^2} \right)^{\frac{1}{2}} \tag{C-19}$$

In Equation C-19, x_C is the number of gas molecules inside a critically sized nucleus.

Substituting Equation C-13 into Equation C-19 arrives at,

$$Z = \frac{2 \cdot R_C}{3 \cdot x_C} \cdot \left(\frac{\sigma_{LG}}{k \cdot T} \right)^{\frac{1}{2}} . \tag{C-20}$$

Next, Equations C-20, C-16, C-2 (evaluated at $x = x_C$ or $R = R_C$), and C-17 can be substituted into Equation C-18. Equation C-5, the ideal gas law is also used as applied to a critically sized bubble. After simplification, a nucleation rate expression for the case of homogeneous nucleation as shown in Equation C-21 is achieved.

Homogeneous Nucleation:
$$J = N \cdot \left(\frac{2 \cdot \sigma_{LG}}{\pi \cdot m} \right)^{\frac{1}{2}} \cdot \exp\left(\frac{-\Delta F_C}{k \cdot T} \right) \qquad \text{(C-21)}$$

Sometimes a correction factor, B, is also included inside the $(\quad)^{1/2}$ term in the denominator of Equation C-21 [Blander and Katz (1975)]. For situations involving chemical equilibrium $B = 1$, so it is simply omitted here.

C.2 Heterogeneous Nucleation

The concepts and methods of homogeneous nucleation theory can be extended to account for situations involving heterogeneous nucleation. Equations C-22 through C-24 list the appropriate expressions for heterogeneous nucleation at a smooth planar interface (Case 1), heterogeneous nucleation in a conical cavity (Case 2), and heterogeneous nucleation on a conical projection (Case 3). These three special cases are presented in Wilt (1986).

Case 1:
$$J = N^{\frac{2}{3}} \cdot G_{1a} \cdot \left(\frac{2 \cdot \sigma_{LG}}{\pi \cdot m \cdot G_{1b}} \right)^{\frac{1}{2}} \cdot exp\left(\frac{-\Delta F_C \cdot G_{1b}}{k \cdot T} \right) \tag{C-22}$$

Case 2:
$$J = N^{\frac{2}{3}} \cdot G_{2a} \cdot \left(\frac{2 \cdot \sigma_{LG}}{\pi \cdot m \cdot G_{2b}} \right)^{\frac{1}{2}} \cdot exp\left(\frac{-\Delta F_C \cdot G_{2b}}{k \cdot T} \right) \tag{C-23}$$

Case 3:
$$J = N^{\frac{2}{3}} \cdot G_{3a} \cdot \left(\frac{2 \cdot \sigma_{LG}}{\pi \cdot m \cdot G_{3b}} \right)^{\frac{1}{2}} \cdot exp\left(\frac{-\Delta F_C \cdot G_{3b}}{k \cdot T} \right) \tag{C-24}$$

The correction factors G_{1a}, G_{1b}, G_{2a}, G_{2b}, G_{3a}, and G_{3b} are defined by,

$$G_{1a} = \frac{1 + \cos\theta}{2} , \tag{C-25}$$

$$G_{1b} = \frac{2 + 3 \cdot \cos\theta - \cos^3\theta}{4} , \tag{C-26}$$

$$G_{2a} = \frac{1 - \sin(\theta - \omega)}{2} , \tag{C-27}$$

$$G_{2b} = \frac{2 - 2 \cdot \sin(\theta - \omega) + \frac{\cos\theta \cdot \cos^2(\theta - \omega)}{\sin\omega}}{4} , \tag{C-28}$$

$$G_{3a} = \frac{1 + sin(\theta + \omega)}{2} , \qquad \text{(C-29)}$$

$$G_{3b} = \frac{2 + 2 \cdot sin(\theta + \omega) + \frac{cos\theta \, .cos^2(e + \omega)}{sin\omega}}{4} , \qquad \text{(C-30)}$$

where θ represents the contact angle and ω represents the cone semi-vertex angle.

To illustrate how the derivation of the nucleation rate expression for homogeneous nucleation can be extended to arrive at the nucleation rate expressions for heterogeneous nucleation, the derivation of Equation C-22 for Case 1 is now developed.

In homogeneous nucleation there is only a liquid-gas interface; however, in heterogeneous nucleation at a smooth planar interface there are now liquid-gas, solid-gas, and solid-liquid interfaces. Taking the appropriate areas and surface free energies for the interfaces into account, the ***AF*** expression for heterogeneous nucleation at a smooth planar interface is,

$$\Delta F = \sigma_{LG} \cdot A_{LG} + (\sigma_{SG} - \sigma_{SL}) \cdot A_{SG} - (P_G - P_L) \cdot V_G + x \cdot (\mu_G - \mu_L) , \qquad \text{(C-31)}$$

where **A** stands for an area and σ denotes an interfacial tension. The subscripts *LG,* SG, and ***SL*** stand for liquid-gas, solid-gas, and solid-liquid, respectively.

The diagram in Figure C-1 represents a gas bubble on a smooth interface with contact angle θ. This diagram defines *z*, R_P, and ***R***. ***R*** can also be interpreted as the bubble's radius of curvature.

Letting $\xi = z/R$ and applying principles from geometry allows us to arrive at,

$$\xi = cos(\pi - e) = -cos\theta , \qquad \text{(C-32)}$$

$$V_G = \frac{\pi}{3} \cdot (R - z)^2 \cdot (2 \cdot R + z) = \frac{\pi}{3} \cdot R^3 \cdot \left(2 - 3 \cdot \xi + \xi^3\right) , \quad \text{(C-33)}$$

$$A_{LG} = 2 \cdot \pi \cdot R_P \cdot (R - z) = 2 \cdot \pi \cdot R^2 \cdot (1 - \xi) , \quad \text{(C-34)}$$

$$A_{SG} = \pi \cdot R_P^2 = \pi \cdot R^2 \cdot \left(1 - \xi^2\right) . \quad \text{(C-35)}$$

A force balance at the edges of the bubble (known as Young's Equation) yields,

$$\sigma_{SL} = \sigma_{SG} + \sigma_{LG} \cdot \cos(\pi - \theta) = \sigma_{SG} + \xi \cdot \sigma_{LG} . \quad \text{(C-36)}$$

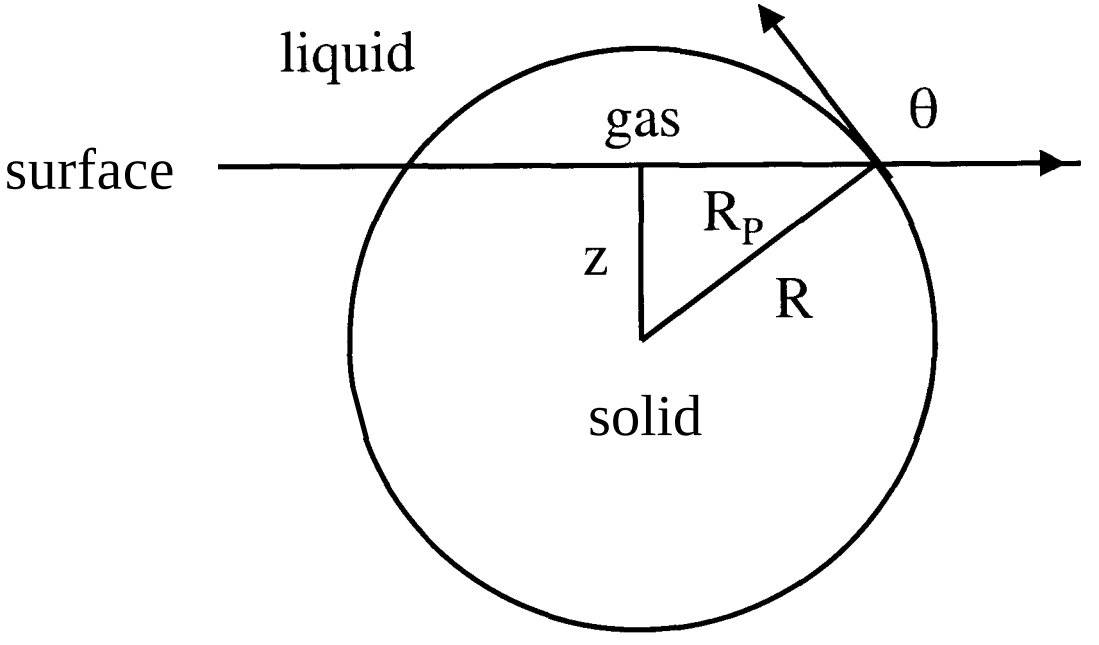

Figure C-1. Diagram for heterogeneous nucleation on a smooth planar interface showing the dimensions z, R_P, and R [modified from Blander and Katz (1975)].

The chemical potential difference equation (C-4) along with the Laplace equations (C-6 and C-7) remain the same since R represents the bubble's radius of curvature. The ideal gas law expression in Equation C-5 is modified to,

$$x = \frac{P_G \cdot V_G}{k \cdot T} = \left(P_L + \frac{2 \cdot \sigma_{LG}}{R} \right) \cdot \frac{4 \cdot \pi \cdot R^3 \cdot G_{1b}}{3 \cdot k \cdot T} \qquad \text{(C-37)}$$

The **ΔF** expression in Equation C-31 can now be substituted into using Equations C-32 through C-37 along with the appropriate Laplace and chemical potential difference equations. The ΔF expression for heterogeneous nucleation at a smooth planar interface can then be simplified to,

$$\Delta F \qquad {}_{LG} \cdot G_{1b} + \frac{4}{3} \cdot \pi \cdot R^3 \cdot G_{1b} \cdot \left(P_L + \frac{2 \cdot \sigma_{LG}}{R} \right. \qquad \left| \frac{P_L + \frac{2 \cdot \sigma_{LG}}{R}}{P_L + \frac{2 \cdot \sigma_{LG}}{R_C}} \right) \qquad \text{(C-38)}$$

The critical free energy change for heterogeneous nucleation at a smooth planar interface can be found by letting the radius of curvature (R) equal the critical radius of curvature (R_C). The critical free energy change thus simplifies to,

$$\Delta F_C = \frac{4}{3} \cdot \pi \cdot R_C^2 \cdot \sigma_{LG} \cdot G_{1b} \ . \qquad \text{(C-39)}$$

The same approximation technique as in Equation C-18 is now applied to determine the heterogeneous nucleation rate on a smooth planar interface. The result appearing in Equation C-22 for heterogeneous nucleation at a smooth planar interface (Case 1) is arrived at after applying the Zeldovich correction factor technique.

Appendix D: Initial Raw Data from Experimental Apparatus

D.1 Raw Data from "Nucleation" Lapse Time Experiments

The following experiments were conducted by saturating air with water at 1400 psig for 10 minutes. This led to supersaturation ratios in the range of 18-21. Shielded 200 μm, 450 μm, and 1320 μm capillaries were used for these experiments.

Table D-1. Raw Data "Nucleation Lapse Time" Experiments

200 μm Capillary		450 μm Capillary		1320 μm Capillary	
D_{max} (μm)	Δt_n (s)	D_{max} (μm)	Δt_n (s)	D_{max} (μm)	Δt_n (s)
2069.4	6.62	2458.3	36.31	3111.1	71.20
2083.3	6.36	2500.0	29.64	3083.3	70.43
2055.6	6.36	2486.1	30.28	3097.2	67.97
1958.3	4.01	2472.2	28.03	3097.2	93.82
2069.4	7.64	2293.8	37.13	3125.0	97.81
2069.4	7.73	2343.2	28.12	3097.2	102.15
1997.9	12.21	2269.2	28.22	3097.2	91.06
1899.2	9.85	2416.7	25.90	3097.2	97.72
1997.9	10.81	2402.8	25.06		
1973.2	8.24	2444.4	28.79		
1997.9	10.92	2430.6	27.08		
1973.2	18.71				
1997.9	14.68				
1973.2	18.34				
1973.2	13.80				
1973.2	15.29				
1800.5	13.95				
1800.5	14.20				
200 μm Capillary Averages: D_{max} = 1981.3 ± 37.7 μm; Δt_n = 11.10 ± 1.99 s					
450 μm Capillary Averages: D_{max} = 2410.7 ± 45.6 μm; Δt_n = 29.51 ± 2.29 s					
1320 μm Capillary Averages: D_{max} = 3100.7 ± 8.5 μm; Δt_n = 86.52 ± 9.83 s					

D.2 Raw Data from Long Term Behavior at Artificial Capillaries

Table D-2: Time Study Analysis of Air Bubbles in Water Growing from a 450 μm Capillary with $T = 21.0°C$ and $SSR = 7.3$

Time (min)	D_{max} (μm)
20.63	2361.1
43.88	2361.1
68.72	2361.1
97.53	2347.2
133.97	2347.2
176.08	2361.1
224.08	2333.3
277.12	2333.3

Time (min)	t_G (min)
33.26	23.25
56.30	24.83
83.12	28.82
115.75	36.43
155.02	42.12
200.08	48.00
250.60	53.03

Time (min)	Δh (cm)
0	0.95
15	0.85
30	0.80
60	0.75
90	0.70
120	0.65
165	0.60
220	0.55
255	0.50
305	0.45
360	0.40

Table D-3: Time Study Analysis of Air Bubbles in Water Growing from a 450 μm Capillary with $T = 20.0°C$ and $SSR = 15.5$

Time (min)	D_{max} (pm)
4.50	2361.1
10.05	2333.3
16.32	2347.2
23.80	2333.3
32.52	2333.3
41.90	2319.4
51.78	2319.4
62.88	2333.3
75.47	2319.4
89.25	2319.4
103.98	2333.3
120.47	2333.3
139.25	2319.4
160.22	2319.4
184.25	2319.4
216.12	2347.2
253.18	2347.2
297.73	2333.3

Time (min)	t_G (min)
7.27	5.55
13.18	6.27
20.06	7.48
28.16	8.72
37.21	9.38
46.84	9.88
57.33	11.10
69.17	12.58
82.36	13.78
96.62	14.73
112.22	16.48
129.86	18.78
149.73	20.97
172.23	24.03
200.18	31.87
234.65	37.07
275.46	44.55

Time (min)	Δh (cm)
0	2.10
15	2.00
30	1.90
45	1.80
60	1.70
75	1.60
90	1.50
115	1.40
130	1.30
145	1.20
160	1.10
175	1.05
190	1.00
205	0.95
235	0.85
265	0.80
295	0.70
325	0.65
355	0.60

Table D-4: Time Study Analysis of Air Bubbles in Water Growing from a 450 μm Capillary with $T = 20.0°C$ and $SSR = 35.5$

Time (min)	D_{max} (μm)	Time (min)	t_G (min)	Time (min)	Δh (cm)
1.45	2319.4	1.88	0.87	0	4.80
2.32	2305.6	2.83	1.02	25	3.40
3.33	2305.6	3.87	1.07	48	2.20
4.40	2319.4	5.02	1.23	60	1.80
5.63	2319.4	6.24	1.22	75	1.60
6.86	2305.6	7.54	1.37	90	1.40
8.22	2305.6	8.91	1.37		
9.59	2319.4	10.31	1.45		
11.04	2305.6	11.86	1.65		1.05
12.69	2305.6	13.57	1.77	175	0.90
14.46	2305.6	15.41	1.90	195	0.80
16.36	2319.4	17.39	2.07	225	0.75
18.42	2333.3	19.52	2.20	255	0.65
20.62	2319.4	21.86	2.47	285	0.55
23.09	2305.6	24.41	2.63	315	0.50
25.72	2319.4	27.17	2.90		
28.62	2305.6	30.50	3.75		
32.37	2333.3	34.49	4.23		
36.61	2333.3	38.97	4.73		
41.34	2305.6	43.90	5.12		
46.46	2305.6	49.34	5.77		
52.22	2319.4	55.58	6.72		
58.94	2333.3	62.76	7.65		
66.59	2305.6	70.83	8.48		
75.07	2305.6	80.08	10.02		
85.09	2305.6	91.10	12.02		
97.11	2305.6	104.90	15.58		
112.69	2305.6	122.22	19.07		
131.76	2305.6	143.57	23.63		
155.39	2319.4	169.44	28.09		
183.48	2333.3	200.49	34.02		
217.50	2305.6	237.97	40.93		
258.43	2319.4				

Table D-5: Time Study Analysis of Air Bubbles in Water Growing from a 450 μm

Time (min)	D_{max} (pm)	Time (min)	t_G (min)	Time (min)	Δh (cm)
0.67	2388.9	0.88	0.42	0	6.20
1.09	2375.0	1.44	0.70	15	3.40
1.79	2291.7	2.16	0.74	30	2.20
2.53	2361.1	2.92	0.78	45	1.60
3.31	2361.1	3.78	0.94	60	1.35
4.25	2361.1	4.82	1.13	75	1.10
5.38	2361.1	5.94	1.12	90	1.00
6.50	2361.1	7.24	1.48	105	0.90
7.98	2361.1	8.74	1.52	121	0.85
9.50	2347.2	10.43	1.87	165	0.70
11.37	2319.4	12.49	2.25	180	0.60
13.62	2361.1	14.96	2.68	225	0.53
16.30	2361.1	17.76	2.92	285	0.50
19.22	2361.1	20.93	3.43	360	0.45
22.65	2361.1				
26.68	2361.1	29.17	4.97		
31.65	2361.1	34.42	5.55		
37.20	2361.1	40.59	6.78		
43.98	2361.1	47.82	7.67		
51.65	2361.1	55.66	8.02		
59.67	2333.3	64.62	9.92		
69.58	2347.2	74.86	10.55		
80.13	2347.2	86.28	12.28		
92.42	2305.6	100.47	16.10		
108.52	2361.1	117.57	18.10		
126.62	2361.1	138.99	24.75		
151.37	2361.1	165.52	28.32		
17968	2347.2	196.12	32.88		
212.57	2347.2	232.36	39.58		
252.15	2291.7	277.40	50.50		
302.65	2361.1				

Table D-6: Time Study Analysis of Air Bubbles in Water Growing from a 200 μm Capillary with $T = 20.0°C$ and $SSR = 17.8$

Time (min)	D_{max} (μm)	Time (min)	t_G (min)	Time (min)	Δh (cm)
3.18	1944.4	4.92	3.47	0	2.40
6.65	1944.4	8.67	4.05	15	2.25
10.70	1944.4	13.42	5.43	30	2.05
16.13	1930.6	18.91	5.55	45	1.95
21.68	1930.6	24.57	5.78	60	1.90
27.47	1930.6	30.53	6.13	90	1.75
33.60	1944.4	36.55	5.90	160	1.40
39.50	1944.4	42.57	6.15	210	1.15
45.65	1944.4	48.80	6.30	255	1.05
51.95	1944.4	55.20	6.50	300	0.95
58.45	1944.4	62.02	7.13	360	0.85
65.58	1958.3	69.68	8.20		
73.78	1944.4	78.16	8.75		
82.53	1930.6	87.52	9.97		
92.50	1930.6	97.77	10.55		
103.05	1944.4	108.63	11.17		
114.22	1944.4	120.23	12.03		
126.25	1944.4	132.60	12.70		
138.95	1958.3	145.64	13.38		
152.33	1958.3	159.99	15.32		
167.65	1930.6	175.92	16.53		
184.19	1930.6	193.06	17.75		
201.94	1930.6	211.13	18.38		
220.32	1930.6	230.04	19.45		
239.77	1944.4	250.09	20.63		

D.3 Analysis of the Long Term Behavior Experiments

Table D-7 summarizes the findings of an analysis performed on the experiments listed in §D.2. The purpose of this analysis was to compare the actual drop in dissolved gas concentration to the drop caused by bubbles from the capillary itself. For all of the experiments, less than 1% of the drop in dissolved gas concentration could be attributed to the bubbles that formed at the artificial capillary. If we assume that there were ten extraneous bubbles for every one that formed at the capillary, 90% of the drop in dissolved gas concentration would still have to occur from the large gas-liquid interface at the top of the bubble cell. It is interesting to note the apparent importance of this interface, but it does not impact the results of the First Full Bubble Only Experiments since the actual dissolved gas concentration is measured.

SSR	ID (μm)	% Drop in C_A Caused by Bubbles from the Capillary
7.3	450	0.57%
15.5	450	0.50%
17.8	200	0.37%
35.5	450	0.28%
45.4	450	0.19%

Appendix E: Raw Data for First Full Bubble Only Experiments

Table E-1. Raw Data for 450 μm Capillary, 2 min Air Saturation

Trial ID	Δh (cm)	T (°C)	D_{max} (μm)	t_G (min)
#1	0.475	20.0	2305.6	54.72
#2	0.475	20.0	2305.6	55.57
#3	0.450	21.0	2319.4	57.55
#4	0.450	20.0	2305.6	57.28
#5	0.500	21.0	2305.6	51.70
Average	0.470	20.4	2308.3	55.36
Std. Deviation	0.021	0.5	6.2	2.36
± 95 %	0.018	0.5	5.4	2.07

Table E-2. Raw Data for **450** μm Capillary, 3 min Air Saturation

Trial ID	Δh (cm)	T (°C)	D_{max} (μm)	t_G (min)
#1	0.725	20.0	2347.2	24.85
#2	0.800	20.0	2333.3	23.32
#3	0.725	21.0	2333.3	24.28
#4	0.775	20.0	2319.4	23.32
#5	0.725	21.0	2305.6	24.00
Average	0.750	20.4	2327.8	23.95
Std. Deviation	0.035	0.5	15.8	0.66
± 95 %	0.031	0.5	13.9	0.58

Table E-3. Raw Data for 450 μm Capillary, 10 min Air Saturation

Trial ID	Δh (cm)	T (°C)	D_{max} (μm)	t_G (min)
#1	1.875	20.0	2319.4	5.27
#2	1.875	21.0	2333.3	5.60
#3	1.875	21.5	2319.4	5.42
#4	2.225	22.0	2361.1	3.87
#5	2.025	23.5	2375.0	4.62
Average	1.975	21.6	2341.7	4.95
Std. Deviation	0.154	1.3	25.2	0.71
± 95 %	0.135	1.1	22.1	0.62

Table E-4. Raw Data for 450 μm Capillary, 25 min Air Saturation

Trial ID	Δh (cm)	T (°C)	D_{max} (μm)	t_G (min)
#1	4.175	22.0	2347.2	0.95
#2	4.275	24.0	2361.1	0.98
#3	4.125	24.0	2333.3	1.03
#4	4.225	25.0	2333.3	0.88
#5	4.275	26.0	2319.4	0.78
Average	4.215	24.2	2338.9	0.93
Std. Deviation	0.065	1.5	15.8	0.10
± 95 %	0.057	1.3	13.9	0.08

Table E-5. Raw Data for 450 μm Capillary, 40 min Air Saturation

Trial ID	Δh (cm)	T (°C)	D_{max} (μm)	t_G (min)
#1	5.675	22.5	2347.2	0.42
#2	5.225	26.0	2319.4	0.33
#3	5.725	27.0	2333.3	0.35
#4	5.175	27.0	2319.4	0.40
#5	4.975	27.0	2333.3	0.40
Average	5.355	25.9	2330.6	0.38
Std. Deviation	0.329	1.9	11.6	0.04
± 95 %	0.288	1.7	10.2	0.03

Table E-6. Raw Data for 450 μm Capillary (Repeat), 2 min Air Saturation

Trial ID	Δh (cm)	T (°C)	D_{max} (μm)	t_G (min)
#1	0.500	21.0	2361.1	55.92
#2	0.500	21.0	2347.2	54.77
#3	0.450	22.0	2347.2	57.48
#4	0.475	20.0	2361.1	54.43
#5	0.450	21.5	2333.3	59.75
Average	0.475	21.1	2350.0	56.47
Std. Deviation	0.025	0.7	11.6	2.19
± 95 %	0.022	0.7	10.2	1.92

Table E-7. Raw Data for 450 μm Capillary (Repeat), 3 min Air Saturation

Trial ID	Δh (cm)	T (°C)	D_{max} (μm)	t_G (min)
#1	0.800	26.0	2333.3	22.17
#2	0.800	26.0	2347.2	22.25
#3	0.775	27.0	2347.2	19.77
#4	0.725	22.5	2375.0	21.33
#5	0.775	24.0	2388.9	24.73
Average	0.775	25.1	2358.3	22.05
Std. Deviation	0.031	1.8	22.8	1.80
± 95 %	0.027	1.6	20.0	1.58

Table E-8. Raw Data for 450 μm Capillary (Repeat), 10 min Air Saturation

Trial ID	Δh (cm)	T (°C)	D_{max} (μm)	t_G (min)
#1	2.125	30.0	2333.3	3.18
#2	2.125	24.5	2361.1	3.78
#3	2.225	25.0	2361.1	4.00
#4	2.125	26.0	2347.2	4.18
#5	2.025	27.0	2333.3	4.02
Average	2.125	26.5	2347.2	3.83
Std. Deviation	0.071	2.2	13.9	0.39
± 95 %	0.062	1.9	12.2	0.34

Table E-9. Raw Data for 450 μm Capillary (Repeat), 25 min Air Saturation

Trial ID	Δh (cm)	T (°C)	D_{max} (μm)	t_G (min)
#1	4.175	30.0	2333.3	0.88
#2	4.200	29.0	2347.2	0.78
#3	4.100	29.5	2347.2	0.73
#4	4.150	30.0	2333.3	0.82
#5	4.150	30.0	2333.3	0.73
Average	4.155	29.7	2338.9	0.79
Std. Deviation	0.037	0.4	7.6	0.06
± 95 %	0.033	0.4	6.7	0.06

Trial ID	Ah (cm)	T (°C)	D_{max} (μm)	t_G (min)
#1	5.150	29.0	2388.9	0.45
#2	5.225	29.5	2361.1	0.33
#3	4.875	25.5	2361.1	0.53
#4	5.275	28.5	2333.3	0.38
#5	5.525	30.0	2361.1	0.33
Average	5.210	28.5	2361.1	0.41
Std. Deviation	0.234	1.8	19.6	0.09
± 95 %	0.205	1.5	17.2	0.07

Table E-11. Raw Data for 200 μm Capillary, 2 min Air Saturation

Trial ID	Δh (cm)	T (°C)	D_{max} (μm)	t_G (min)
#1	0.425	20.0	1944.4	43.42
#2	0.425	21.0	1958.3	44.36
#3	0.425	22.5	1958.3	42.83
#4	0.375	21.0	1930.6	44.82
#5	0.375	22.0	1944.4	45.28
Average	0.405	21.3	1947.2	44.10
Std. Deviation	0.027	0.9	11.6	1.01
± 95 %	0.024	0.9	10.2	0.88

Table E-12. Raw Data for 200 μm Capillary, 3 min Air Saturation

Trial ID	Δh (cm)	T (°C)	D_{max} (μm)	t_G (min)
#1	0.600	20.0	1972.2	24.22
#2	0.650	20.0	1944.4	21.68
#3	0.650	21.0	1944.4	21.87
#4	0.675	22.0	1930.6	17.85
#5	0.700	22.5	1958.3	16.40
Average	0.675	21.1	1950.0	20.40
Std. Deviation	0.025	0.8	13.9	2.83
± 95 %	0.022	0.7	12.2	2.48

Trial ID	Ah (cm)	T (°C)	D_{max} (μm)	t_G (min)
#1	1.800	22.0	1888.9	4.00
#2	1.850	22.0	1944.4	4.48
#3	1.900	20.0	1958.3	4.30
#4	1.875	21.5	1916.7	3.82
#5	1.950	22.5	1958.3	3.80
Average	1.875	21.6	1933.3	4.08
Std. Deviation	0.056	1.0	30.1	0.30
f 9 5 %	0.049	0.8	26.4	0.26

Table E-14. Raw Data for 200 μm Capillary, 25 min Air Saturation

Trial ID	Δh (cm)	T (°C)	D_{max} (μm)	t_G (min)
#1	3.725	24.0	1958.3	0.98
#2	3.725	23.0	1944.4	0.93
#3	3.675	24.0	1958.3	0.95
#4	3.775	23.5	1944.4	0.92
#5	3.725	25.5	1958.3	0.93
Average	3.725	24.0	1952.8	0.94
Std. Deviation	0.035	0.9	7.6	0.03
± 95 %	0.031	0.8	6.7	0.02

Table E-15. Raw Data for 200 μm Capillary, 40 min Air Saturation

Trial ID	Δh (cm)	T (°C)	D_{max} (μm)	t_G (min)
#1	5.325	23.5	1933.3	0.35
#2	5.125	25.5	1944.4	0.37
#3	5.025	27.5	1916.7	0.37
#4	5.100	27.5	1944.4	0.38
#5	5.275	28.5	1933.3	0.33
Average	5.175	26.5	1934.4	0.36
Std. Deviation	0.125	2.0	11.4	0.02
± 95 %	0.110	1.8	10.0	0.02

Table E-16. Raw Data for 50 μm Capillary, 2 min Air Saturation

Trial ID	Δh (cm)	T (°C)	D_{max} (μm)	t_G (min)
#1	0.450	20.0	1930.6	39.60
#2	0.425	19.5	1916.7	41.13
#3	0.400	20.0	1861.1	42.60
#4	0.400	20.0	1847.2	37.15
#5	0.400	22.0	1916.7	42.35
Average	0.415	20.3	1894.4	40.57
Std. Deviation	0.022	1.0	37.5	2.25
± 95 %	0.020	0.9	32.9	1.97

Trial ID	**Ah** (cm)	T (°C)	D_{max} (μm)	t_G (min)
#1	0.750	20.0	1861.1	14.25
#2	0.700	19.5	1833.3	16.98
#3	0.725	20.0	1847.2	16.83
#4	0.775	**24.0**	1861.1	13.63
#5	0.800	23.0	1861.1	13.98
Average	0.750	21.3	1852.8	15.14
Std. Deviation	0.040	2.0	12.4	1.63
f 9 5 %	0.035	1.8	10.9	1.43

Table E-18. Raw Data for 50 μm Capillary, 10 min Air Saturation

Trial ID	Δh (cm)	T (°C)	D_{max} (μm)	t_G (min)
#1	1.725	24.0	1875.0	4.00
#2	1.825	23.0	1833.3	3.58
#3	1.875	24.5	1833.3	3.63
#4	1.875	25.0	1833.3	3.85
#5	1.875	25.0	1930.6	4.10
Average	1.835	24.3	1861.1	3.83
Std. Deviation	0.065	0.8	42.8	0.22
± 95 %	0.057	0.7	37.5	0.20

Table E-19. Raw Data for 50 μm Capillary, 25 min Air Saturation

Trial ID	Δh (cm)	T (°C)	D_{max} (μm)	t_G (min)
#1	3.875	22.0	1930.6	0.85
#2	3.975	24.0	1805.6	0.77
#3	3.875	23.0	1805.6	0.73
#4	3.925	24.0	1875.0	0.78
#5	4.025	24.5	1819.4	0.73
Average	3.935	23.5	1847.2	0.77
Std. Deviation	0.065	1.0	54.7	0.05
± 95 %	0.057	0.9	47.9	0.04

Trial ID	Δh (cm)	T (°C)	D_{max} (μm)	t_G (min)
#1	5.300	24.5	1902.8	0.35
#2	5.350	26.5	1847.2	0.32
#3	5.400	23.5	1847.2	0.32
#4	5.325	25.0	1916.7	0.33
#5	5.350	25.0	1847.2	0.30
Average	5.345	24.9	1865.7	0.32
Std. Deviation	0.037	1.1	34.6	0.02
f 9 5 %	0.033	1.0	30.3	0.02

Trial ID	Δh (cm)	T (°C)	D_{max} (μm)	t_G (min)
#1	0.500	23.5	2347.2	53.72
#2	0.500	22.0	2361.1	54.05
#3	0.450	22.0	2333.3	56.73
#4	0.450	23.0	2347.2	58.85
#5	0.450	23.0	2361.1	60.10
Average	0.470	22.7	2350.0	56.69
Std. Deviation	0.027	0.7	11.6	2.83
+ 95 %	0.024	0.6	10.2	2.48

Table E-22. Raw Data for Double Time/Half Pressure (450 μm), 6 min Air Saturation

Trial ID	Δh (cm)	T (°C)	D_{max} (μm)	t_G (min)
#1	0.825	23.5	2361.1	18.73
#2	0.825	24.0	2361.1	21.90
#3	0.850	24.5	2347.2	19.77
#4	0.775	25.0	2347.2	19.70
#5	0.775	24.5	2347.2	21.25
Average	0.810	24.3	2352.8	20.27
Std. Deviation	0.034	0.6	7.6	1.28
± 95 %	0.029	0.5	6.7	1.12

Table E-23. Raw Data for Double Time/Half Pressure (450 μm), 20 min Air Saturation

Trial ID	Δh (cm)	T (°C)	D_{max} (μm)	t_G (min)
#1	2.075	24.0	2375.0	4.18
#2	2.125	25.5	2375.0	4.17
#3	2.225	27.0	2361.1	4.08
#4	2.200	28.0	2375.0	3.50
#5	2.225	23.5	2361.1	4.05
Average	2.170	25.6	2369.4	4.00
Std. Deviation	0.067	1.9	7.6	0.28
± 95 %	0.059	1.7	6.7	0.25

Table E-24. Raw Data for Double Time/Half Pressure (450 μm), 50 min Air Saturation

Trial ID	Δh (cm)	T (°C)	D_{max} (μm)	t_G (min)
#1	3.425	27.5	2361.1	1.52
#2	3.275	29.0	2361.1	1.55
#3	3.300	30.5	2361.1	1.50
#4	3.300	31.0	2333.3	1.35
#5	3.300	30.5	2333.3	1.43
Average	3.320	29.7	2350.0	1.47
Std. Deviation	0.060	1.4	15.2	0.08
± 95 %	0.052	1.3	13.3	0.07

Table E-25. Raw Data for Double Time/Half Pressure (450 μm), 80 min Air Saturation

Trial ID	Δh (cm)	T (°C)	D_{max} (μm)	t_G (min)
#1	4.275	28.0	2347.2	0.67
#2	4.525	30.5	2361.1	0.73
#3	4.725	28.0	2361.1	0.70
#4	4.175	31.0	2347.2	0.72
#5	4.175	31.5	2347.2	0.68
Average	4.375	29.8	2352.8	0.70
Std. Deviation	0.242	1.7	7.6	0.03
± 95 %	0.212	1.5	6.7	0.02

Table E-26. Raw Data for Partial Depressurization (50 μm), 10 min Air Saturation

Trial ID	Δh (cm)	T (°C)	D_{max} (μm)	t_G (min)
#1	2.400	26.5	1902.8	53.52
#2	2.275	27.5	1902.8	52.85
#3	2.275	27.0	1888.9	52.87
#4	2.400	28.0	1875.0	53.55
#5	2.575	29.0	1847.2	49.15
Average	2.385	27.6	1883.3	52.39
Std. Deviation	0.123	1.0	23.2	1.84
± 95 %	0.108	0.8	20.4	1.61

Table E-27. Raw Data for Partial Depressurization (50 μm), 25 min Air Saturation

Trial ID	Δh (cm)	T (°C)	D_{max} (μm)	t_G (min)
#1	3.825	27.0	1875.0	21.77
#2	3.800	26.0	1861.1	21.00
#3	3.750	27.0	1888.9	22.03
#4	3.750	28.0	1875.0	21.62
#5	3.675	25.5	1888.9	21.72
Average	3.760	26.7	1877.8	21.63
Std. Deviation	0.058	1.0	11.6	0.38
± 95 %	0.050	0.9	10.2	0.34

Trial ID	Ah (cm)	T (°C)	D_{max} (μm)	t_G (min)
#1	5.425	32.0	1888.9	10.92
#2	5.475	24.0	1875.0	11.05
#3	5.525	26.5	1916.7	11.58
#4	5.550	29.0	1916.7	11.23
#5	5.475	29.5	1847.2	11.00
Average	5.490	28.2	1888.9	11.16
Std. Deviation	0.049	3.1	29.5	0.27
± 95 %	0.043	2.7	25.8	0.23

Table E-29. Raw Data for CO_2 (450 μm), 5 min CO_2 Saturation

Trial ID	Volume (cm^3)	T (°C)	D_{max} (μm)	t_G (min)
#1	60	30.0	2333.3	2.28
#2	45	26.0	2305.6	3.48
#3	50	27.5	2305.6	2.98
#4	40	27.5	2319.4	3.90
#5	50	28.5	2305.6	2.88
Average	49.0	27.9	2313.9	3.11
Std. Deviation	7.4	1.5	12.4	0.62
± 95 %	6.5	1.3	10.9	0.54

Table E-30. Raw Data for CO_2 (450 μm), 10 min CO_2 Saturation

Trial ID	Volume (cm^3)	T (°C)	D_{max} (μm)	t_G (min)
#1	95	29.0	2347.2	0.57
#2	105	30.0	2333.3	0.47
#3	110	31.0	2319.4	0.42
#4	105	31.0	2305.6	0.47
#5	105	31.0	2333.3	0.52
Average	104.0	30.4	2327.8	0.49
Std. Deviation	5.5	1.5	12.4	0.06
± 95 %	4.8	1.3	10.9	0.05

Table E-31. Raw Data for CO_2 (450 μm), 15 min CO_2 Saturation

Trial ID	Volume (cm^3)	T (°C)	D_{max} (μm)	t_G (min)
#1	160	33.0	2347.2	0.17
#2	150	29.5	2319.4	0.17
#3	150	31.0	2333.3	0.15
#4	155	31.0	2319.4	0.18
#5	165	31.0	2347.2	0.17
Average	156.0	31.1	2333.3	0.17
Std. Deviation	6.5	1.2	13.9	0.01
± 95 %	5.7	1.1	12.2	0.01

Trial ID	Volume (cm^3)	T (°C)	D_{max} (μm)	t_G (min)
#1	190	33.0	2291.7	0.08
#2	190	34.0	2305.6	0.10
#3	190	35.0	2347.2	0.10
#4	200	30.0	2333.3	0.08
#5	195	32.0	2319.4	0.10
Average	193.0	32.8	2319.4	0.09
Std. Deviation	4.5	1.9	22.0	0.01
± 95 %	3.9	1.7	19.2	0.01

Table E-33. Raw Data for He (450 μm), 1 min He Saturation

Trial ID	Δh (cm)	T (°C)	D_{max} (μm)	t_G (min)
#1	0.450	22.0	2361.1	26.92
#2	0.400	23.0	2333.3	23.98
#3	0.450	23.0	2361.1	20.87
#4	0.425	23.5	2333.3	25.43
#5	0.450	24.0	2347.2	24.50
Average	0.435	23.1	2347.2	24.34
Std. Deviation	0.022	0.7	13.9	2.24
± 95 %	0.020	0.7	12.2	1.96

Table E-34. Raw Data for He (450 μm), 2 min He Saturation

Trial ID	Δh (cm)	T (°C)	D_{max} (μm)	t_G (min)
#1	0.650	21.0	2347.2	11.73
#2	0.625	22.0	2375.0	10.87
#3	0.650	22.0	2361.1	11.62
#4	0.625	23.0	2361.1	12.00
#5	0.650	23.5	2333.3	9.72
Average	0.640	22.3	2355.6	11.19
Std. Deviation	0.014	1.0	15.8	0.92
± 95 %	0.012	0.9	13.9	0.81

Table E-35. Raw Data for He (450 μm), 3 min He Saturation

Trial ID	Δh (cm)	T (°C)	D_{max} (μm)	t_G (min)
#1	1.025	25.0	2319.4	4.92
#2	0.775	25.5	2333.3	7.13
#3	0.925	25.5	2361.1	5.67
#4	0.775	26.0	2347.2	6.83
#5	1.000	24.5	2333.3	4.70
Average	0.900	25.3	2338.9	5.85
Std. Deviation	0.120	0.6	15.8	1.10
± 95 %	0.105	0.5	13.9	0.96

Table E-36. Raw Data for He (450 μm), 5 min He Saturation

Trial ID	Δh (cm)	T (°C)	D_{max} (μm)	t_G (min)
#1	1.775	27.0	2333.3	1.80
#2	1.800	27.5	2361.1	1.75
#3	1.775	24.0	2333.3	2.05
#4	1.800	25.0	2347.2	1.98
#5	1.775	25.0	2347.2	1.82
Average	1.785	25.7	2344.4	1.88
Std. Deviation	0.014	1.5	11.6	0.13
± 95 %	0.012	1.3	10.2	0.11

Trial ID	Ah (cm)	T (°C)	D_{max} (μm)	t_G (min)
#1	2.300	22.0	2361.1	1.33
#2	2.050	23.0	2291.7	1.48
#3	2.300	24.5	2347.2	1.40
#4	2.300	25.0	2375.0	1.45
#5	2.300	26.0	2375.0	1.32
Average	2.250	24.1	2350.0	1.40
Std. Deviation	0.112	1.6	34.6	0.07
+ 95 %	0.098	1.4	30.3	0.06

Table E-38. Raw Data for He (450 μm), 10 min He Saturation

Trial ID	Δh (cm)	T (°C)	D_{max} (μm)	t_G (min)
#1	2.900	25.0	2333.3	0.82
#2	2.900	26.0	2347.2	0.87
#3	2.700	27.0	2333.3	0.83
#4	2.675	28.0	2319.4	0.88
#5	2.675	28.0	2319.4	0.97
Average	2.770	26.8	2330.6	0.87
Std. Deviation	0.119	1.3	11.6	0.06
+ 95 %	0.104	1.1	10.2	0.05

Table E-39. Raw Data for He (450 μm), 5 min He Saturation (Low Temperature)

Trial ID	Δh (cm)	T (°C)	D_{max} (μm)	t_G (min)
#1	1.500	15.0	2361.1	3.78
#2	1.450	13.0	2333.3	4.23
#3	1.450	14.0	2375.0	4.18
#4	1.400	14.5	2361.1	3.68
#5	1.400	14.0	2333.3	3.98
Average	1.440	14.1	2352.8	3.97
Std. Deviation	0.042	0.7	18.6	0.24
± 95 %	0.037	0.7	16.3	0.21

Trial ID	Ah (cm)	T (°C)	D_{max} (μm)	t_G (min)
#1	2.300	41.0	2305.6	0.82
#2	2.400	42.5	2291.7	0.73
#3	2.450	43.0	2291.7	0.62
#4	2.400	42.5	2277.8	0.73
#5	2.350	42.5	2291.7	0.62
Average	2.380	42.3	2291.7	0.70
Std. Deviation	0.057	0.8	9.8	0.09
± 95 %	0.050	0.7	8.6	0.08

Table E-41. Raw Data for He (450 μm), 7.5 min He Saturation (Low Temperature)

Trial ID	Δh (cm)	T (°C)	D_{max} (μm)	t_G (min)
#1	2.000	16.5	2361.1	2.72
#2	1.950	14.5	2347.2	2.35
#3	1.850	14.5	2361.1	1.82
#4	1.900	15.0	2319.4	2.21
#5	1.850	14.0	2347.2	2.15
Average	1.910	14.9	2347.2	2.25
Std. Deviation	0.065	1.0	17.0	0.33
+ 95 %	0.057	0.8	14.9	0.29

Table E-42. Raw Data for He (450 μm), 3 min He Saturation (High Temperature)

Trial ID	Δh (cm)	T (°C)	D_{max} (μm)	t_G (min)
#1	1.650	40.5	2319.4	1.55
#2	1.700	41.5	2305.6	1.33
#3	1.700	41.0	2291.7	1.47
#4	1.700	41.0	2319.4	1.55
#5	1.700	43.0	2291.7	1.17
Average	1.690	41.4	2305.6	1.41
Std. Deviation	0.022	1.0	13.9	0.16
± 95 %	0.020	0.8	12.2	0.14

Appendix F: Mathcad Program to find $\beta = \beta(\phi)$ for the Scriven Model

The following solve block was used *to calculate* β (represented here with b) as a function of ϕ (represented here with p).

$b := 0.1$ (initial guess)

$p := 0.06706$

Given

$$p = 2 \cdot b^3 \cdot \exp\left(3 \cdot b^2\right) \cdot \int_b^{\infty} x^{-2} \cdot \exp\left(-x^2 - 2 \cdot b^3 \cdot x^{-1}\right) dx$$

Find(b) = 0.21582

Appendix G: FORTRAN Code for the C-T Model

```
C     C-T (Cyr-Thompson) Bubble Growth Model
C     David R. Cyr
C     Updated: August 26,2000

C     Program Description:  This program can be used to solve the
C     partial differential equation for spherically symmetric phase
C     growth of a bubble by taking into account both the diffusive
C     and convective effects.  This program is an improvement over
C     the Scriven (1959) model due to a more accurate representation
C     of the bubble surface velocity.  For a given set of experimental
C     conditions, the value of the bubble growth time (TG) is adjusted
C     until the mass balance is satisfied to within +/- 1%.

C     Definition of Variables

C     CAO = Initial dissolved gas concentration and the dissolved gas
C     concentration at a location infinitely far away from the
C           bubble surface (mg/mm^3)
C     CAS   = Equilibrium dissolved gas concentration (mg/mm^3)
C     C( ) = Array for the concentration profile in the radial
C           coordinate throughout the liquid phase (mg/mm^3)
C     DENSG = Density of the gas phase (mg/mm^3)
C     DMAX = Bubble diameter at detachment (mm)
C     DR = Radial coordinate grid size (mm)
C     DT = Time coordinate grid size (min)
C     H = DO loop index range variable
C     I = DO loop index range variable
C     INF = Final radial position, assumed to be equivalent to a point
C           infinitely far away from the bubble surface, it is between
C           three and four maximum bubble diameters away from the initial
C           position
C     INT = Integral (approximated by using the trapezoidal rule) needed
C           for evaluation of RHS variable (mg)
C     J = DO loop index range variable
C     K = Diffusion coefficient (mm^2/min)
C     LHS = Left hand side of mass balance, which is the amount of gas
C           inside the bubble (mg)
C     P = DO loop index range variable
C     PT1 = Part one of the explicit form of the difference equation for
C           this partial differential equation (mg/(min*mm^3))
C     PT2 = Part two of the explicit form of the difference equation for
C           this partial differential equation (mg/(min*mm^3))
C     PT3 = Part three of the explicit form of the difference equation
```

```
C           for this partial differential equation (mg/(min*mm^3))
C       R( ) = Array for the radial position (mm)
C       RA = Bubble radius (mm)
C       RAD = First derivative with respect to time of the bubble radius
C           (mm/min)
C       RAO = Initial bubble radius, also assumed to be inside diameter of
C           capillary (mm)
C       RHS = Right hand side of mass balance, which is the amount of
C           dissolved gas that has left the liquid phase and entered the
C           bubble (mg)
C       RS = Real storage for the value of S
C       S = Radial position representing the location of the bubble
C           surface (S = 2 for 50 micron capillary, S = 8 for 200 micron
C           capillary, and S = 18 for 450 micron capillary when 564 grid
C           grid points in the radial direction are used)
C       SC( ) = Storage array for the concentration profile in the radial
C           coordinate throughout the liquid phase (mg/mm^3)
C       SLOPE = Constant slope, approximating the growth characteristics
C           of a bubble diameter squared versus time plot (mm^2/min)
C       T = Time (min)
C       TG = Bubble growth time (min)
C       TSTEPS = Number of required time steps
C       W = DO loop index range variable

        DOUBLE PRECISION C(564), DENSG, DMAX, DR, DT, INT, K, LHS
        DOUBLE PRECISION PT1, PT2, PT3, R(564), RA, RAD, RAO, RHS
        DOUBLE PRECISION SC(564), SLOPE, T, TG, CAO, CAS, RS
        INTEGER H, I, INF, J, P, S, TSTEPS, W

C       INPUT PARAMETERS

        RAO = 0.225
        K = 0.12741
        DT = 0.000075
        DR = 0.0125
C       The ratio of DT/(DR)^2 must be less than 0.5 in order to
C           guarantee convergence
        T = O
        DMAX = 2.308333333333333333
        TG = 55.36333333333333333
        SLOPE = (((DMAX)''''2)-((2*RA0)**2))/TG
        DENSG = 0.00120524
        S = 18
        INF = 564
        TSTEPS = 738178
        CAO = 1.021093e-4
```

```
      CAS = 2.2664e-5

      DO 10 I = S,INF
      R(I) = (I)*DR
      C(I) = CAO
      SC(I) = CAO
10    CONTINUE

      DO 70 P = 1,TSTEPS
      T = (P-1)*DT
      RA = (0.5)*(((2*RA0)**2)+((SLOPE)*T))**0.5
      RAD = SLOPE/4/((((2*RA0)**2)+((SLOPE)*T))**0.5)

C     START OF TRAPEZOIDAL RULE INTEGRATION

      INT = 0

      SC(S) = SC(S+1) - DR*DENSG*RAD/K
      IF (SC(S).LT.CAS) SC(S)=CAS
      C(S) = SC(S)

      IF (SC(S).EQ.CAS) SC(S+1) = CAS + DR*DENSG*RAD/K

      DO 20, J = S+1,(INF-1)
      PT1 = K*((SC(J-1))-(2*SC(J))+(SC(J+1)))/(DR*DR)
      PT2 = K*(((SC(J+1))-(SC(J-1)))/(DR*(R(J))))
      PT3 = ((RA/(R(J)))**2)*RAD*((SC(J+1))-(SC(J-1)))/(2*DR)
      C(J) = SC(J) + DT*(PT1+PT2-PT3)
      IF (C(J).LT.C(S)) C(J)=C(S)
      IF (SC(S).EQ.CAS) C(S+1) = CAS + DR*DENSG*RAD/K
      INT = INT + ((R(J))*(R(J)))*(C(INF)-C(J))*(DR)
20    CONTINUE

      INT = INT + ((DR)/2)*(RA*RA*(C(INF)-C(S))+0)

C     MASS BALANCE

      LHS = 4*3.14159*(((RA)*(RA)*(RA))-((RA0)*(RA0)*(RA0)))*DENSG/3
      RHS = 4*3.14159*INT

      DO 30, H = S,INF
      SC(H) = C(H)
30    CONTINUE

      RS = S
      IF (RA.LT.((RS+0.5)*DR)) GOTO 50
```

```
      S=S+1

      DO 40, W = S,INF
      SC(W)=C(W-1)
40    CONTINUE

      SC(S-1)=CAS
      C(S-1)=CAS
50    WRITE (*,60) T,LHS,RHS
60    FORMAT (2X,E17.10,2X,E17.10,2X,E17.10,2X,E17.10)

70    CONTINUE

      WRITE (*,80) ((RHS-LHS)/LHS)
80    FORMAT (2X,E17.10,2X,E17.10,2X,E17.10,2X,E17.10)

      END
```

Appendix H: Sample Calculations

The following sample calculation shows how the raw data from the First Full Bubble Only Experiments in Appendix E are converted to the calculated results that appear in Appendix I. The raw data from Table E-1 will be used as an example to show how the corresponding calculated results in Table I-1 were obtained.

H.1 Supersaturation Ratio *(SSR)*

The supersaturation ratio **is** defined as the ratio of the actual dissolved gas concentration to the equilibrium dissolved gas concentration. To determine the actual dissolved gas concentration, the collected gas volume must be determined. After depressurization, the gas collection tube is used to collect any gases that are released from the solution. These dissolved gases are released at a slow rate initially when the supersaturation is not disturbed by agitation. After a bubble growth experiment, the magnetic stir bar is turned back on to drive off any remaining dissolved gases. For the air and helium experiments, a gas collection tube with markings every 0.1 cm was used. This gas collection tube had a volume of 19.635 mL for every 1.0 cm of height. Equation H-1 can be used to convert the Ah readings in cm to volume of gas released in mL.

$$VOL(\text{mL}) = 19.635 \cdot \Delta h(\text{cm}) \tag{H-1}$$

An actual graduated cylinder with 10 mL markings was used for the C02 experiments because larger quantities of gas were released by the highly soluble CO_2. The volume of gas released for the CO_2 experiments could be determined directly, so it was not necessary to use an expression like Equation H-1 to find the volume.

The volume of gas released is converted to the mass of gas released using the gas density and this quantity is then divided by the liquid volume in the cell, which was always 140 mL. The resulting quantity is the mass of gas released per unit volume of liquid. To find the actual bulk concentration this quantity is added to the equilibrium solubility concentration. The bulk concentration of dissolved gas can therefore be found with,

$$C_{A0} = \frac{VOL \cdot \rho_G}{140mL} + C_{AS} \quad . \tag{H-2}$$

The supersaturation ratio (SSR) can then be calculated with,

$$SSR = \frac{C_{A0}}{C_{AS}} \quad . \tag{H-3}$$

As an example, the data from Trial #1 in Table E-1 for air dissolved in water will be used to calculate the corresponding supersaturation ratio for Trial #1 in Table I-1. In this trial, $\Delta h = 0.475$ cm. Using equation H-1, this gives $VOL = 9.326625$ mL. Since the temperature of this trial was 20.0°C, we can use Appendix J to find that $\rho_G = 1.2068$ kg/m^3 and that $C_{AS} = 0.02286$ kg/m^3. Using Equation H-2 along with appropriate unit conversions, C_{A0} is found to be 0.103256 kg/m^3. Finally, a SSR of 4.5 is then calculated by using Equation H-3. A SSR of 4.5 is the value that appears in Table I-1 for the calculated supersaturation ratio for Trial #1.

H.2 Diffusion Coefficient (D_{AB})

Diffusion coefficient data for air in water, carbon dioxide in water, and helium in water are listed in Appendix J as a function of temperature. Literature tends to report these diffusion coefficients at only one temperature, but the temperature dependence can

be estimated using the Wilke and Chang (1955) correlation. For gases dissolved in water, this correlation has the form of,

$$D_{AB} = c \cdot T/\mu_W, \tag{H-4}$$

where the diffusion coefficient is proportional to the absolute temperature divided by the viscosity of the solvent (in this case water). The proportionality constant c can be found if the diffusion coefficient is known for at least one temperature.

Manley (1960) reported a diffusion coefficient for air in water of 2.100 **x** 10^{-9} m^2/s at 20°C. The diffusion coefficient for carbon dioxide in water at 25°C was found to be 2.000 x 10^{-9} m^2/s by Vivian and King (1964). Ferrell and Himmelblau (1967) listed the diffusion coefficient for helium in water at 25°C to be 6.280 **x** 10^{-9} m^2/s. These three diffusion coefficients with their corresponding temperatures were used to construct Table J-3.

For our chosen example (Trial #1 of Table E-l), the temperature of 20°C leads to an air in water diffusion coefficient of 2.100 x 10^{-9} m^2/s for Trial #1 in Table I-1.

H.3 Bubble Growth Time Predicted by Manley (t_M)

The bubble growth expression developed by Manley (1960), listed in Equation H-5, can be rearranged to solve for the bubble growth time ($t = t_M$):

$$D^2 = D_0^2 + \frac{8 \cdot D_{AB} \cdot (C_{A0} - C_{AS}) \cdot t}{\rho_G} \tag{H-5}$$

For Trial #1 of Table E-1, D_{max} was found to be 2305.6 μm. Since all of the data in Table E-1 was found using a 450 μm ID capillary, D_0 can be taken as 450 μm. **Also,** as noted earlier, ρ_G = 1.2068 kg/m^3, D_{AB} = 2.100 x 10^{-9} m^2/s, C_{A0} = 0.103256 kg/m^3, and

C_{AS} = 0.02286 kg/m^3 for Trial #1 in Table E-1. Using these values along with appropriate unit conversions, a t_M value of 76.14 minutes is calculated. This is in agreement with the calculated result for t_M appearing in Table I-1.

H.4 Bubble Growth Time Predicted by Scriven (t_S)

The Scriven (1959) bubble growth expression, listed in Equation H-6, can also be rearranged to solve for the bubble growth time ($t = t_S$):

$$D = 4 \cdot \beta(\phi) \cdot \sqrt{D_{AB} \cdot t} \,. \tag{H-6}$$

The same values for D_{max} and D_{AB} that were used in §H.3 are also used here for our example (Trial #1 of Table E-1). Before β, the dimensionless growth parameter defined by Scriven, can be evaluated, ϕ, the dimensionless supersaturation parameter also defined by Scriven must be determined. For bubble growth controlled by mass transfer, Scriven defined ϕ according to,

$$\phi = \frac{\rho_L \cdot (C_{A0} - C_{AS})}{\rho_G \cdot (\rho_L - C_{AS})}. \tag{H-7}$$

Considering that C_{AS} is very small compared to ρ_L and that the ideal gas law can be substituted for ρ_G, ϕ is commonly calculated using,

$$\phi = \frac{R_{IG} \cdot T \cdot (C_B - C_S)}{P \cdot MW} \,, \tag{H-8}$$

The ideal gas constant (R_{IG}) is 82.06 cm^3·atm/mol·K and the molecular weight (MW) of air, which was the solute for all of the trials in Table E-1 is 28.84 g/mole. The other two solutes, carbon dioxide and helium have molecular weights of 44.01 g/mole and 4.00 g/mole, respectively. Recalling that T = 293.15 K (20°C converted to the absolute scale),

$C_{A0} = 0.103256$ kg/m^3, $C_{AS} = 0.02286$ kg/m^3, and that the system was depressurized down to 1 atmosphere (P = 1 atm) in Trial #1, Equation H-8 can be used along with appropriate unit conversion factors to obtain a ϕ value of 0.06706.

By using the Mathcad program in Appendix F, the appropriate value of β corresponding to $\phi = 0.06706$ can be calculated. As shown in the Mathcad program, $\beta =$ 0.21582 for this case.

Equation H-6 can now be used along with appropriate unit conversion factors to calculate a t_S value of 64.93 minutes. This is in agreement with the t_S number reported in Table I-1.

H.5 Results from Using the Raw Data Averages in the C-T Model

The raw data averages from Table E-1 are used to run the C-T Model in FORTRAN. The code for this FORTRAN program appears in Appendix G. Table H-1 contains all of the information that must be supplied to the FORTRAN program. As an example, the raw data averages from Table E-1 are also included.

	Abbreviation	from Table E-1 Data
Initial Bubble Radius (1/2 of capillary ID)	RA0	0.225 mm
Diffusion Coefficient	K	0.12741 mm^2/min
Time Step	DT	0.000075 min
Radial Coordinate Grid Size	DR	0.0125 mm
Initial Time	T	0 min
Bubble Detachment Diameter	DMAX	2.308333333 mm
Bubble Growth Time	TG	55.36333333 min
Gas Density	DENSG	0.00120524 mg/mm^3
Initial Radial Position of Bubble Surface	S	18
Radial Position at Infinity ($3 \cdot D_{max}$)	INF	564
Number of Required Time Steps (TG/DT)	TSTEPS	738178
Initial Concentration Throughout Bulk	C(I)	$1.021093 \cdot 10^{-4}$ mg/mm^3
Concentration at Bubble Surface	C(S)	$2.2664 \cdot 10^{-5}$ mg/mm^3

The initial bubble radius is assumed to be one half the inside diameter of the capillary. Even though the bubble cap attached to the capillary is not perfectly spherical, it soon grows into a sphere like shape so any error due to this approximation is small.

The numerical method used to solve the partial differential equation involves the explicit form of the difference equation. **As** shown in §7.2, DR = 0.0125 provides a sufficiently small grid size. For this method, the ratio of $DT/(DR)^2$ must be less than 0.5 in order to guarantee convergence. DT = 0.000075 satisfies this requirement.

The location corresponding to infinity was chosen as being three maximum bubble diameters large. Since the concentration profiles remained unchanged far away from the bubble, this was deemed to be a good rule of thumb to use for the "infinite" location.

Note that the units of the input items shown in Table H-1 are different from the units used for these quantities elsewhere. The program works best using the units that appear in Table H-1, because numerical errors involving the multiplication of very large and very small numbers are minimized. The units that appear elsewhere are the ones that are more commonly used to report these quantities.

As the program runs, it prints the current time along with the values for the left-hand-side (*LHS*) and right-hand-side *(RHS)* of the mass balance. The *LHS* of the mass balance represents the amount of gas inside the bubble while the *RHS* of the mass balance represents the amount of the dissolved gas that has left the liquid phase and entered the bubble. The *LHS* and *RHS* values should be similar throughout the history of the bubble.

When the program finishes running, the values for *LHS* and *RHS* at the last time step are used to calculate the mass balance error (*MBE*). The formula for calculating the initial mass balance error is,

$$MBE = \left(\frac{RHS - LHS}{LHS} \right) \tag{H-9}$$

Positive *MBE* values represent a greater amount of the dissolved gas having left the solution compared top the amount that is inside the bubble while negative *MBE* values indicate that not enough of the dissolved gas has left the solution to account for the amount of gas inside of the bubble. The first *MBE* value that is calculated from the experimental parameters is known as the initial mass balance error.

Using the Raw Data Averages in Table E-1 as an example, at T = 55.36327763 the values for *LHS* = 0.007704371892 and *RHS* = 0.008007265516. These leads to an initial mass balance error of +3.93% when used in Equation H-9, agreeing with the result that appears in Table I-1.

The bubble growth times predicted by the C-T model are found by adjusting the bubble growth time (TG in FORTRAN) and the number of required time steps (TSTEPS in FORTRAN) until the mass balance is satisfied to within ±1%.

With TG reset to 51.10 and TSTEPS set at 681334, for the last time step FORTRAN displays T = 51.09997743, *LHS* = 0.007704378815, and *RHS* = 0.007740930969. This results in a mass balance error of only +0.47%, which is within the 1% requirement. The bubble growth time predicted by the C-T Model (t_{CT}) would therefore be 51.10 min for this example. This is the number reported in Table I-1.

The value in parentheses after the t_{CT} value represents the percentage of the bubble growth the bubble growth that is caused by diffusion-only (the balance being the convective contribution). The diffusion contribution is found by setting the PT1 and PT2 terms in the FORTRAN code equal to zero and re-running it. Equation H-10 can then be used to calculate the contribution that diffusion alone has on the bubble growth.

$$\%Diffusion = \frac{\left(LHS - RHS_{no\ diffusion}\right)}{LHS} \tag{H-10}$$

After re-running the program with PT1 and PT2 set equal to zero, the final T and final *LHS* value will remain the same, but the *RHS* value will change. Upon re-running the program $RHS_{,,\ diffusion} = 0.0009132043374$. Using this value in Equation H-10 leads to the result that 88.15% of the bubble growth is caused by diffusion (the balance caused by the convective effect). This value is in agreement with the result in Table I-1.

Appendix I: Calculated Results from 1st Full Bubble Only Experiments

Table I-1. Results for 450 μm Capillary, 2 min Air Saturation

Trial ID	*SSR*	D_{AB} (m^2/s)	t_M (min)	t_S (min)
#1	4.5	2.100×10^{-9}	76.14	56.61
#2	4.5	2.100×10^{-9}	76.14	56.61
#3	4.4	2.159×10^{-9}	79.17	59.35
#4	4.3	2.100×10^{-9}	80.37	60.29
#5	4.8	2.159×10^{-9}	70.37	51.86
Average	4.5	2.124×10^{-9}	76.44	56.94
Std. Deviation	0.2	3.215×10^{-11}	3.87	3.28
± 95 %	0.1	2.818×10^{-11}	3.39	2.88
Using Raw Data Averages: Initial Mass Balance Error = +3.93% t_{CT} = 51.10 min (88.15% Diffusion)				

Table I-2. Results for 450 μm Capillary, 3 min Air Saturation

Trial ID	*SSR*	D_{AB} (m^2/s)	t_M (min)	t_S (min)
#1	6.4	2.100×10^{-9}	51.78	35.55
#2	6.9	2.100×10^{-9}	46.35	31.19
#3	6.5	2.159×10^{-9}	49.75	34.17
#4	6.7	2.100×10^{-9}	47.25	32.03
#5	6.5	2.159×10^{-9}	48.53	33.36
Average	6.6	2.124×10^{-9}	48.73	33.26
Std. Deviation	0.2	3.215×10^{-11}	2.13	1.73
± 95 %	0.2	2.818×10^{-11}	1.87	1.51
Using Raw Data Averages: Initial Mass Balance Error = +5.77% t_{CT} = 21.94 min (80.82% Diffusion)				

Table 1-3. Results for 450 μm Capillary, 10 min Air Saturation

Trial ID	*SSR*	D_{AB} (m^2/s)	t_M (min)	t_S (min)
#1	14.9	2.100×10^{-9}	19.53	10.47
#2	15.1	2.159×10^{-9}	19.24	10.30
#3	15.3	2.189×10^{-9}	18.74	10.04
#4	18.1	2.220×10^{-9}	16.15	8.16
#5	17.0	2.319×10^{-9}	17.20	8.97
Average	16.1	2.197×10^{-9}	18.17	9.59
Std. Deviation	1.4	8.103×10^{-11}	1.44	0.99
± 95 %	1.2	7.102×10^{-11}	1.26	0.87
Using Raw Data Averages: Initial Mass Balance Error = +10.00% t_{CT} = 4.23 min (50.15% Diffusion)				

Table 1-4. Results for 450 μm Capillary, 25 min Air Saturation

Trial ID	*SSR*	D_{AB} (m^2/s)	t_M (min)	t_S (min)
#1	33.1	2.220×10^{-9}	8.50	3.32
#2	35.1	2.353×10^{-9}	7.93	3.06
#3	33.9	2.353×10^{-9}	8.02	3.15
#4	35.3	2.425×10^{-9}	7.60	2.95
#5	36.3	2.501×10^{-9}	7.19	2.78
Average	34.7	2.371×10^{-9}	7.85	3.05
Std. Deviation	1.3	1.039×10^{-10}	0.49	0.20
+ 95 %	1.1	9.105×10^{-11}	0.43	0.18
Using Raw Data Averages: Initial Mass Balance Error = +19.01% t_{CT} = 0.62 min (9.62% Diffusion)				

Table I-5. Results for 450 μm Capillary, 40 min Air Saturation

Trial ID	*SSR*	D_{AB} (m^2/s)	t_M (min)	t_S (min)
#1	45.0	2.252×10^{-9}	6.17	2.07
#2	44.1	2.501×10^{-9}	5.89	2.06
#3	49.0	2.574×10^{-9}	5.29	1.76
#4	44.4	2.574×10^{-9}	5.77	2.03
#5	42.7	2.574×10^{-9}	6.08	2.18
Average	45.1	2.495×10^{-9}	5.84	2.02
Std. Deviation	2.4	1.392×10^{-10}	0.35	0.15
± 95 %	2.1	1.220×10^{-10}	0.30	0.14
Using Raw Data Averages: Initial Mass Balance Error = +12.27% t_{CT} = 0.31 min (5.31% Diffusion)				

Table I-6. Results for 450 μm Capillary (Repeat), 2 min Air Saturation

Trial ID	*SSR*	D_{AB} (m^2/s)	t_M (min)	t_S (min)
#1	4.8	2.159×10^{-9}	73.94	54.39
#2	4.8	2.159×10^{-9}	73.04	53.75
#3	4.5	2.220×10^{-9}	78.90	59.09
#4	4.5	2.100×10^{-9}	80.00	59.37
#5	4.4	2.189×10^{-9}	79.04	59.22
Average	4.6	2.165×10^{-9}	76.98	57.16
Std. Deviation	0.2	4.453×10^{-11}	3.24	2.83
± 95 %	0.1	3.903×10^{-11}	2.84	2.48
Using Raw Data Averages: Initial Mass Balance Error = +3.78% t_{CT} = 52.45 min (87.91% Diffusion)				

Table I-7. Results for 450 μm Capillary (Repeat), 3 min Air Saturation

Trial ID	*SSR*	D_{AB} (m^2/s)	t_M (min)	t_S (min)
#1	7.6	2.501×10^{-9}	38.92	26.17
#2	7.6	2.501×10^{-9}	39.40	26.48
#3	7.5	2.574×10^{-9}	39.53	26.75
#4	6.6	2.252×10^{-9}	49.47	33.92
#5	7.2	2.353×10^{-9}	44.83	30.30
Average	7.3	2.436×10^{-9}	42.43	28.73
Std. Deviation	0.4	1.304×10^{-10}	4.62	3.35
± 95 %	0.4	1.143×10^{-10}	4.05	2.94
Using Raw Data Averages: Initial Mass Balance Error = +10.74% t_{CT} = 18.56 min (80.21% Diffusion)				

Table I-8. Results for 450 μm Capillary (Repeat), 10 min Air Saturation

Trial ID	*SSR*	D_{AB} (m^2/s)	t_M (min)	t_S (min)
#1	19.7	2.754×10^{-9}	13.30	6.83
#2	18.1	2.389×10^{-9}	15.72	8.06
#3	19.0	2.425×10^{-9}	14.79	7.46
#4	18.5	2.501×10^{-9}	14.83	7.61
#5	18.0	2.574×10^{-9}	14.94	7.80
Average	18.7	2.528×10^{-9}	14.72	7.55
Std. Deviation	0.7	1.449×10^{-10}	0.88	0.46
± 95 %	0.6	1.270×10^{-10}	0.77	0.41
Using Raw Data Averages: Initial Mass Balance Error = +10.90% t_{CT} = 3.21 min (46.74% Diffusion)				

Table I-9. Results for 450 μm Capillary (Repeat), 25 min Air Saturation

Trial ID	*SSR*	D_{AB} (m^2/s)	t_M (min)	t_S (min)
#1	37.8	2.754×10^{-9}	6.77	2.64
#2	37.4	2.692×10^{-9}	6.97	2.71
#3	36.8	2.723×10^{-9}	7.06	2.78
#4	37.6	2.754×10^{-9}	6.81	2.66
#5	37.6	2.754×10^{-9}	6.81	2.67
Average	37.4	2.735×10^{-9}	6.89	2.69
Std. Deviation	0.4	2.803×10^{-11}	0.13	0.05
± 95 %	0.3	2.457×10^{-11}	0.11	0.05
Using Raw Data Averages: Initial Mass Balance Error = +16.27% t_{CT} = 0.55 min (10.64% Diffusion)				

Trial ID	*SSR*	D_{AB} (m^2/s)	t_M (min)	t_S (min)
#1	45.7	2.692×10^{-9}	5.90	2.07
#2	46.7	2.723×10^{-9}	5.61	1.96
#3	40.9	2.462×10^{-9}	6.65	2.41
#4	46.4	2.661×10^{-9}	5.55	1.93
#5	49.7	2.754×10^{-9}	5.24	1.78
Average	45.8	2.658×10^{-9}	5.79	2.03
Std. Deviation	3.2	1.149×10^{-10}	0.53	0.23
f95%	2.8	1.007×10^{-10}	0.47	0.21

Table I-11. Results for 200 μm Capillary, 2 min Air Saturation

Trial ID	*SSR*	D_{AB} (m^2/s)	t_M (min)	t_S (min)
#1	4.1	2.100×10^{-9}	62.26	45.82
#2	4.2	2.159×10^{-9}	61.45	45.20
#3	4.3	2.252×10^{-9}	58.90	43.32
#4	3.8	2.159×10^{-9}	67.66	50.74
#5	3.9	2.220×10^{-9}	66.74	50.05
Average	4.1	2.178×10^{-9}	63.40	47.02
Std. Deviation	0.2	5.940×10^{-11}	3.70	3.22
± 95 %	0.2	5.207×10^{-11}	3.24	2.82
Using Raw Data Averages: Initial Mass Balance Error = +6.48% t_{CT} = 39.82 min (89.03% Diffusion)				

Table I-12. Results for 200 μm Capillary, 3 min Air Saturation

Trial ID	*SSR*	D_{AB} (m^2/s)	t_M (min)	t_S (min)
#1	5.4	2.100×10^{-9}	45.38	31.47
#2	5.8	2.100×10^{-9}	40.71	27.81
#3	5.9	2.159×10^{-9}	39.60	27.05
#4	6.2	2.220×10^{-9}	36.55	24.78
#5	6.4	2.252×10^{-9}	35.76	24.06
Average	6.2	2.210×10^{-9}	39.60	27.04
Std. Deviation	0.3	4.752×10^{-11}	2.03	1.56
± 95 %	0.2	4.165×10^{-11}	1.78	1.37
Using Raw Data Averages: Initial Mass Balance Error = +8.27% t_{CT} = 18.25 min (82.43% Diffusion)				

Table I-13. Results for 200 μm Capillary, 10 min Air Saturation

Trial ID	*SSR*	D_{AB} (m^2/s)	t_M (min)	t_S (min)
#1	14.8	2.220×10^{-9}	13.11	6.93
#2	15.2	2.220×10^{-9}	13.53	7.08
#3	15.1	2.100×10^{-9}	14.13	7.33
#4	15.3	2.189×10^{-9}	13.15	6.86
#5	16.0	2.252×10^{-9}	12.84	6.60
Average	15.3	2.196×10^{-9}	13.35	6.96
Std. Deviation	0.4	5.829×10^{-11}	0.50	0.27
± 95 %	0.4	5.110×10^{-11}	0.44	0.24
Using Raw Data Averages: Initial Mass Balance Error = +12.62% t_{CT} = 3.37 min (51.72% Diffusion)				

Table I-14. Results for 200 μm Capillary, 25 min Air Saturation

Trial ID	*SSR*	D_{AB} (m^2/s)	t_M (min)	t_S (min)
#1	30.7	2.353×10^{-9}	6.43	2.57
#2	30.1	2.285×10^{-9}	6.53	2.61
#3	30.3	2.353×10^{-9}	6.52	2.62
#4	30.8	2.319×10^{-9}	6.35	2.53
#5	31.5	2.462×10^{-9}	6.15	2.46
Average	30.7	2.355×10^{-9}	6.39	2.56
Std. Deviation	0.5	6.664×10^{-11}	0.16	0.07
± 95 %	0.5	5.841×10^{-11}	0.14	0.06
Using Raw Data Averages: Initial Mass Balance Error = +15.85% t_{CT} = 0.70 min (16.60% Diffusion)				

Table I-15. Results for 200 μm Capillary, 40 min Air Saturation

Trial ID	*SSR*	D_{AB} (m^2/s)	t_M (min)	t_S (min)
#1	43.1	2.319×10^{-9}	4.45	1.50
#2	42.9	2.462×10^{-9}	4.40	1.51
#3	43.5	2.602×10^{-9}	4.13	1.43
#4	44.1	2.602×10^{-9}	4.19	1.44
#5	46.4	2.661×10^{-9}	3.91	1.32
Average	44.0	2.529×10^{-9}	4.22	1.44
Std. Deviation	1.4	1.387×10^{-10}	0.22	0.07
± 95 %	1.2	1.215×10^{-10}	0.19	0.07
Using Raw Data Averages: Initial Mass Balance Error = +15.30% t_{CT} = 0.28 min (9.59% Diffusion)				

Table 1-16. Results for 50 μm Capillary, 2 min Air Saturation

Trial ID	*SSR*	D_{AB} (m^2/s)	t_M (min)	t_S (min)
#1	4.3	2.100×10^{-9}	58.55	42.27
#2	4.1	2.072×10^{-9}	61.94	45.13
#3	4.0	2.100×10^{-9}	61.21	45.02
#4	4.0	2.100×10^{-9}	60.30	44.35
#5	4.1	2.220×10^{-9}	61.40	45.15
Average	4.1	2.118×10^{-9}	60.68	44.38
Std. Deviation	0.2	5.822×10^{-11}	1.33	1.23
± 95 %	0.1	5.103×10^{-11}	1.17	1.07
Using Raw Data Averages: Initial Mass Balance Error = +6.92% t_{CT} = 36.81 min (88.44% Diffusion)				

Table I-17. Results for 50 μm Capillary, 3 min Air Saturation

Trial ID	*SSR*	D_{AB} (m^2/s)	t_M (min)	t_S (min)
#1	6.6	2.100×10^{-9}	32.64	21.46
#2	6.1	2.072×10^{-9}	34.40	22.94
#3	6.4	2.100×10^{-9}	33.27	22.02
#4	7.2	2.425×10^{-9}	27.36	17.85
#5	7.3	2.285×10^{-9}	28.13	18.23
Average	6.7	2.196×10^{-9}	31.16	20.50
Std. Deviation	0.5	1.535×10^{-10}	3.19	2.31
± 95 %	0.4	1.345×10^{-10}	2.80	2.03
Using Raw Data Averages: Initial Mass Balance Error = +7.37% t_{CT} = 13.85 min (79.60% Diffusion)				

Table I-18. Results for 50 μm Capillary, 10 min Air Saturation

Trial ID	*SSR*	D_{AB} (m^2/s)	t_M (min)	t_S (min)
#1	14.7	2.353×10^{-9}	12.86	6.81
#2	15.3	2.285×10^{-9}	11.96	6.23
#3	16.1	2.389×10^{-9}	11.14	5.75
#4	16.2	2.425×10^{-9}	10.97	5.66
#5	16.2	2.425×10^{-9}	12.17	6.28
Average	15.7	2.375×10^{-9}	11.82	6.14
Std. Deviation	0.7	5.865×10^{-11}	0.77	0.46
± 95 %	0.6	5.141×10^{-11}	0.68	0.41
Using Raw Data Averages: Initial Mass Balance Error = +15.18% t_{CT} = 3.03 min (53.37% Diffusion)				

Table I-19. Results for 50 μm Capillary, 25 min Air Saturation

Trial ID	*SSR*	D_{AB} (m^2/s)	t_M (min)	t_S (min)
#1	30.8	2.220×10^{-9}	6.43	2.50
#2	32.7	2.353×10^{-9}	5.17	1.99
#3	31.3	2.285×10^{-9}	5.46	2.13
#4	32.3	2.353×10^{-9}	5.65	2.19
#5	33.3	2.389×10^{-9}	5.11	1.96
Average	32.1	2.320×10^{-9}	5.57	2.15
Std. Deviation	1.0	6.726×10^{-11}	0.53	0.22
± 95 %	0.9	5.895×10^{-11}	0.47	0.19
Using Raw Data Averages: Initial Mass Balance Error = +16.38% t_{CT} = 0.58 min (18.24% Diffusion)				

Table I-20. Results for 50 μm Capillary, 40 min Air Saturation

Trial ID	*SSR*	D_{AB} (m^2/s)	t_M (min)	t_S (min)
#1	43.6	2.389×10^{-9}	4.25	1.42
#2	45.5	2.540×10^{-9}	3.73	1.24
#3	43.6	2.319×10^{-9}	4.05	1.34
#4	44.2	2.425×10^{-9}	4.22	1.41
#5	44.4	2.425×10^{-9}	3.90	1.30
Average	44.3	2.420×10^{-9}	4.03	1.34
Std. Deviation	0.8	8.033×10^{-11}	0.22	0.08
± 95 %	0.7	7.041×10^{-11}	0.19	0.07
Using Raw Data Averages: Initial Mass Balance Error = +12.42% t_{CT} = 0.29 min (11.02% Diffusion)				

Table I-21. Results for Double Time/Half Pressure (450 μm), 4 min Air Saturation

Trial ID	*SSR*	D_{AB} (m^2/s)	t_M (min)	t_S (min)
#1	4.9	2.319×10^{-9}	68.00	50.02
#2	4.8	2.220×10^{-9}	71.89	52.88
#3	4.5	2.220×10^{-9}	77.94	58.39
#4	4.5	2.285×10^{-9}	76.67	57.40
#5	4.5	2.285×10^{-9}	77.61	58.08
Average	4.7	2.266×10^{-9}	74.42	55.35
Std. Deviation	0.2	4.383×10^{-11}	4.34	3.72
± 95 %	0.2	3.842×10^{-11}	3.80	3.26
Using Raw Data Averages: Initial Mass Balance Error = +4.59% t_{CT} = 52.12 min (88.13% Diffusion)				

Table I-22. Results for Double Time/Half Pressure (450 μm), 6 min Air Saturation

Trial ID	*SSR*	D_{AB} (m^2/s)	t_M (min)	t_S (min)
#1	7.5	2.319×10^{-9}	41.72	27.85
#2	7.6	2.353×10^{-9}	41.11	27.44
#3	7.8	2.389×10^{-9}	38.83	25.76
#4	7.3	2.425×10^{-9}	41.95	28.39
#5	7.2	2.389×10^{-9}	42.58	28.82
Average	7.5	2.375×10^{-9}	41.24	27.65
Std. Deviation	0.2	4.039×10^{-11}	1.45	1.18
± 95 %	0.2	3.540×10^{-11}	1.27	1.04
Using Raw Data Averages: Initial Mass Balance Error = +8.80% t_{CT} = 18.04 min (79.25% Diffusion)				

Table I-23. Results for Double Time/Half Pressure (450 μm), 20 min Air Saturation

Trial ID	*SSR*	D_{AB} (m^2/s)	t_M (min)	t_S (min)
#1	17.5	2.353×10^{-9}	16.54	8.55
#2	18.4	2.462×10^{-9}	15.44	7.91
#3	19.7	2.574×10^{-9}	13.94	7.03
#4	19.8	2.631×10^{-9}	13.95	7.07
#5	18.6	2.319×10^{-9}	15.47	7.81
Average	18.8	2.468×10^{-9}	15.07	7.67
Std. Deviation	0.9	1.354×10^{-10}	1.12	0.64
± 95 %	0.8	1.187×10^{-10}	0.98	0.56
Using Raw Data Averages: Initial Mass Balance Error = +13.46% t_{CT} = 3.15 min (45.57% Diffusion)				

Table I-24. Results for Double Time/Half Pressure (450 μm), 50 min Air Saturation

Trial ID	*SSR*	D_{AB} (m^2/s)	t_M (min)	t_S (min)
#1	30.0	2.602×10^{-9}	8.95	3.82
#2	29.4	2.692×10^{-9}	9.05	3.93
#3	30.3	2.786×10^{-9}	8.68	3.76
#4	30.5	2.819×10^{-9}	8.37	3.63
#5	30.3	2.786×10^{-9}	8.47	3.67
Average	30.1	2.737×10^{-9}	8.70	3.76
Std. Deviation	0.4	8.928×10^{-11}	0.30	0.12
± 95 %	0.4	7.826×10^{-11}	0.26	0.11
Using Raw Data Averages: Initial Mass Balance Error = +15.88% t_{CT} = 1.07 min (21.66% Diffusion)				

Table I-25. Results for Double Time/Half Pressure (450 μm), 80 min Air Saturation

Trial ID	*SSR*	D_{AB} (m^2/s)	t_M (min)	t_S (min)
#1	37.5	2.631×10^{-9}	7.01	2.70
#2	41.2	2.786×10^{-9}	6.33	2.38
#3	41.3	2.631×10^{-9}	6.42	2.36
#4	38.4	2.819×10^{-9}	6.70	2.61
#5	38.6	2.853×10^{-9}	6.62	2.58
Average	39.4	2.744×10^{-9}	6.61	2.53
Std. Deviation	1.7	1.057×10^{-10}	0.27	0.15
± 95 %	1.5	9.262×10^{-11}	0.23	0.13
Using Raw Data Averages: Initial Mass Balance Error = +15.85% t_{CT} = 0.49 min (8.80% Diffusion)				

Table I-26. Results for Partial Depressurization (50 μm), 10 min Air Saturation

Trial ID	*SSR*	D_{AB} (m^2/s)	t_M (min)	t_S (min)
#1	3.5	2.540×10^{-9}	69.40	53.01
#2	3.4	2.602×10^{-9}	72.37	55.75
#3	3.4	2.574×10^{-9}	72.31	55.73
#4	3.6	2.631×10^{-9}	64.53	49.24
#5	3.9	2.692×10^{-9}	55.56	41.68
Average	3.6	2.608×10^{-9}	66.83	51.08
Std. Deviation	0.2	5.773×10^{-11}	7.06	5.89
± 95 %	0.2	5.060×10^{-11}	6.19	5.17
Using Raw Data Averages: Initial Mass Balance Error = -1.59% t_{CT} = 53.91 min (91.54% Diffusion)				

Table I-27. Results for Partial Depressurization (50 μm), 25 min Air Saturation

Trial ID	*SSR*	D_{AB} (m^2/s)	t_M (min)	t_S (min)
#1	5.6	2.574×10^{-9}	37.14	25.93
#2	5.5	2.501×10^{-9}	38.07	26.63
#3	5.5	2.574×10^{-9}	38.59	27.05
#4	5.6	2.631×10^{-9}	37.07	25.98
#5	5.2	2.462×10^{-9}	41.51	29.25
Average	5.5	2.548×10^{-9}	38.47	26.97
Std. Deviation	0.1	6.671×10^{-11}	1.81	1.36
± 95 %	0.1	5.847×10^{-11}	1.59	1.19
Using Raw Data Averages: Initial Mass Balance Error = +5.82% t_{CT} = 20.16 min *(85.30%* Diffusion)				

Table 1-28. Results for Partial Depressurization (50 μm), 40 min Air Saturation

Trial ID	*SSR*	D_{AB} (m^2/s)	t_M (min)	t_S (min)
#1	8.6	2.887×10^{-9}	22.25	14.09
#2	7.5	2.353×10^{-9}	27.08	17.46
#3	7.9	2.540×10^{-9}	25.80	16.58
#4	8.3	2.692×10^{-9}	24.12	15.46
#5	8.2	2.723×10^{-9}	22.46	14.45
Average	8.1	2.639×10^{-9}	24.34	15.61
Std. Deviation	0.4	2.017×10^{-10}	2.10	1.42
± 95 %	0.4	1.768×10^{-10}	1.84	1.24
Using Raw Data Averages: Initial Mass Balance Error = +7.09% t_{CT} = 10.26 min (77.23% Diffusion)				

Table I-29. Results for CO_2 (450 μm), 5 min CO_2 Saturation

Trial ID	*SSR*	D_{AB} (m^2/s)	t_M (min)	t_S (min)
#1	1.8	2.272×10^{-9}	11.22	5.02
#2	1.5	2.063×10^{-9}	16.07	8.04
#3	1.6	2.146×10^{-9}	13.90	6.69
#4	1.5	2.146×10^{-9}	17.59	9.17
#5	1.6	2.195×10^{-9}	13.59	6.54
Average	1.6	2.164×10^{-9}	14.47	7.09
Std. Deviation	0.1	7.653×10^{-11}	2.45	1.58
± 95 %	0.1	6.708×10^{-11}	2.15	1.38
Using Raw Data Averages: Initial Mass Balance Error = +10.67% t_{CT} = 2.55 min (38.19% Diffusion)				

Table I-30. Results for CO_2 (450 μm), 10 min CO_2 Saturation

Trial ID	*SSR*	D_{AB} (m^2/s)	t_M (min)	t_S (min)
#1	2.2	2.220×10^{-9}	7.34	2.67
#2	2.3	2.272×10^{-9}	6.41	2.22
#3	2.4	2.325×10^{-9}	5.90	1.99
#4	2.4	2.325×10^{-9}	6.11	2.11
#5	2.4	2.325×10^{-9}	6.26	2.16
Average	2.3	2.293×10^{-9}	6.41	2.23
Std. Deviation	0.1	4.716×10^{-11}	0.56	0.26
± 95 %	0.1	4.134×10^{-11}	0.49	0.23
Using Raw Data Averages: Initial Mass Balance Error = +19.26% t_{CT} = 0.34 min (5.39% Diffusion)				

Table I-31. Results for CO_2 (450 μm), 15 min CO_2 Saturation

Trial ID	*SSR*	D_{AB} (m^2/s)	t_M (min)	t_S (min)
#1	3.2	2.501×10^{-9}	3.87	1.06
#2	2.9	2.245×10^{-9}	4.48	1.27
#3	3.0	2.325×10^{-9}	4.38	1.24
#4	3.0	2.325×10^{-9}	4.19	1.17
#5	3.2	2.325×10^{-9}	4.03	1.08
Average	3.1	2.344×10^{-9}	4.19	1.16
Std. Deviation	0.2	9.409×10^{-11}	0.25	0.10
± 95 %	0.1	8.247×10^{-11}	0.22	0.08
Using Raw Data Averages: Initial Mass Balance Error = +17.59% t_{CT} = 0.14 min (4.32% Diffusion)				

Trial ID	*SSR*	D_{AB} (m^2/s)	t_M (min)	t_S (min)
#1	3.7	2.439×10^{-9}	3.18	0.78
#2	3.8	2.500×10^{-9}	3.14	0.77
#3	3.8	2.564×10^{-9}	3.18	0.78
#4	3.5	2.272×10^{-9}	3.37	0.80
#5	3.6	2.381×10^{-9}	3.25	0.78
Average	3.7	2.431×10^{-9}	3.22	0.78
Std. Deviation	0.1	1.122×10^{-10}	0.09	0.01
± 95 %	0.1	9.835×10^{-11}	0.08	0.01
Using Raw Data Averages: Initial Mass Balance Error = -6.12% t_{CT} = 0.10 min (3.52% Diffusion)				

Table I-33. Results for He (450 μm), 1 min He Saturation

Trial ID	*SSR*	D_{AB} (m^2/s)	t_M (min)	t_S (min)
#1	8.8	5.750×10^{-9}	30.84	23.26
#2	7.9	5.917×10^{-9}	32.90	25.30
#3	8.8	5.917×10^{-9}	29.97	22.61
#4	8.4	6.005×10^{-9}	30.51	23.24
#5	8.8	6.094×10^{-9}	28.75	21.69
Average	8.5	5.937×10^{-9}	30.59	23.22
Std. Deviation	0.4	1.275×10^{-10}	1.51	1.33
± 95 %	0.3	1.118×10^{-10}	1.33	1.16
Using Raw Data Averages: Initial Mass Balance Error = +1.04% t_{CT} = 23.78 min (89.00% Diffusion)				

Table I-34. Results for He (450 μm), 2 min He Saturation

Trial ID	*SSR*	D_{AB} (m^2/s)	t_M (min)	t_S (min)
#1	12.2	5.590×10^{-9}	21.70	15.34
#2	11.8	5.750×10^{-9}	22.48	16.00
#3	12.2	5.750×10^{-9}	21.35	15.09
#4	11.8	5.917×10^{-9}	21.58	15.37
#5	12.3	6.005×10^{-9}	19.95	14.11
Average	12.0	5.802×10^{-9}	21.41	15.18
Std. Deviation	0.2	1.618×10^{-10}	0.92	0.69
± 95 %	0.2	1.418×10^{-10}	0.81	0.60
Using Raw Data Averages: Initial Mass Balance Error = +2.31% t_{CT} = 10.61 min (83.64% Diffusion)				

Table I-35. Results for He (450 μm), 3 min He Saturation

Trial ID	*SSR*	D_{AB} (m^2/s)	t_M (min)	t_S (min)
#1	18.9	6.280×10^{-9}	11.95	7.66
#2	14.6	6.377×10^{-9}	15.76	10.75
#3	17.2	6.377×10^{-9}	13.53	8.87
#4	14.6	6.477×10^{-9}	15.71	10.72
#5	18.4	6.186×10^{-9}	12.59	8.11
Average	16.7	6.339×10^{-9}	13.91	9.22
Std. Deviation	2.1	1.104×10^{-10}	1.76	1.45
± 95 %	1.8	9.678×10^{-11}	1.54	1.27
Using Raw Data Averages: Initial Mass Balance Error = +4.02% t_{CT} = 5.55 min (76.76% Diffusion)				

Table I-36. Results for He (450 μm), 5 min He Saturation (Natural Temperature)

Trial ID	*SSR*	D_{AB} (m^2/s)	t_M (min)	t_S (min)
#1	32.2	6.665×10^{-9}	6.58	3.62
#2	32.7	6.739×10^{-9}	6.58	3.60
#3	31.9	6.094×10^{-9}	7.20	3.96
#4	32.4	6.280×10^{-9}	6.97	3.82
#5	32.0	6.280×10^{-9}	7.07	3.89
Average	32.2	6.411×10^{-9}	6.88	3.78
Std. Deviation	0.3	2.769×10^{-10}	0.29	0.16
± 95 %	0.3	2.427×10^{-10}	0.25	0.14
Using Raw Data Averages: Initial Mass Balance Error = +4.45% t_{CT} = 1.76 min (54.81% Diffusion) With Uncorrected D_{AB}: Initial Mass Balance Error = +3.21% t_{CT} = 1.80 min (54.81% Diffusion)				

Table I-37. Results for He (450 μm), 7 min He Saturation

Trial ID	*SSR*	D_{AB} (m^2/s)	t_M (min)	t_S (min)
#1	40.6	5.750×10^{-9}	6.03	3.04
#2	36.5	5.917×10^{-9}	6.18	3.25
#3	41.1	6.186×10^{-9}	5.54	2.79
#4	41.1	6.280×10^{-9}	5.59	2.81
#5	41.3	6.477×10^{-9}	5.42	2.73
Average	40.1	6.122×10^{-9}	5.75	2.92
Std. Deviation	2.1	2.895×10^{-10}	0.33	0.22
± 95 %	1.8	2.537×10^{-10}	0.29	0.19
Using Raw Data Averages: Initial Mass Balance Error = +9.84% t_{CT} = 1.19 min (43.94% Diffusion)				

Table 1-38. Results for He (450 pm), 10 min He Saturation

Trial ID	*SSR*	D_{AB} (m^2/s)	t_M (min)	t_S (min)
#1	51.6	6.280×10^{-9}	4.28	1.97
#2	51.8	6.477×10^{-9}	4.20	1.94
#3	48.5	6.665×10^{-9}	4.33	2.05
#4	48.2	6.815×10^{-9}	4.22	2.01
#5	48.2	6.815×10^{-9}	4.22	2.01
Average	49.7	6.610×10^{-9}	4.25	2.00
Std. Deviation	1.9	2.309×10^{-10}	0.05	0.04
± 95 %	1.6	2.024×10^{-10}	0.05	0.04
t_{CT} = 0.68 min (32.78% Diffusion)				

Trial ID	*SSR*	D_{AB} (m^2/s)	t_M (min)	t_S (min)
#1	25.9	4.732×10^{-9}	11.24	6.50
#2	24.7	4.381×10^{-9}	12.26	7.16
#3	24.9	4.551×10^{-9}	12.24	7.15
#4	24.2	4.640×10^{-9}	12.29	7.25
#5	24.1	4.551×10^{-9}	12.22	7.22
Average	24.8	4.571×10^{-9}	12.05	7.05
Std. Deviation	0.7	1.300×10^{-10}	0.45	0.31
± 95 %	0.6	1.140×10^{-10}	0.40	0.27

Table I-40. Results for He (450 μm), 5 min He Saturation (High Temperature)

Trial ID	*SSR*	D_{AB} (m^2/s)	t_M (min)	t_S (min)
#1	43.0	9.132×10^{-9}	3.62	1.82
#2	45.0	9.369×10^{-9}	3.34	1.66
#3	46.0	9.450×10^{-9}	3.24	1.60
#4	45.0	9.369×10^{-9}	3.29	1.64
#5	44.1	9.369×10^{-9}	3.41	1.71
Average	44.6	9.338×10^{-9}	3.38	1.68
Std. Deviation	1.1	1.203×10^{-10}	0.15	0.09
± 95 %	1.0	1.055×10^{-10}	0.13	0.08
Using Raw Data Averages: Initial Mass Balance Error = +4.81% t_{CT} = 0.64 min (41.07% Diffusion) With Uncorrected D_{AB}: Initial Mass Balance Error = -14.17% t_{CT} = 0.97 min (41.07% Diffusion)				

Table I-41. Results for He (450 μm), 7.5 min He Saturation (Low Temperature)

Trial ID	*SSR*	D_{AB} (m^2/s)	t_M (min)	t_S (min)
#1	34.5	4.959×10^{-9}	8.05	4.25
#2	33.2	4.640×10^{-9}	8.71	4.64
#3	31.6	4.640×10^{-9}	9.30	5.04
#4	32.5	4.732×10^{-9}	8.55	4.60
#5	31.5	4.551×10^{-9}	9.36	5.08
Average	32.7	4.704×10^{-9}	8.79	4.72
Std. Deviation	1.2	1.563×10^{-10}	0.55	0.34
± 95 %	1.1	1.370×10^{-10}	0.48	0.30
Using Raw Data Averages: Initial Mass Balance Error = +3.90% t_{CT} = 2.18 min (51.89% Diffusion) With Uncorrected D_{AB}: Initial Mass Balance Error = +22.51% t_{CT} = 1.59 min (51.89% Diffusion)				

Table I-42. Results for He (450 μm), 3 min He Saturation (High Temperature)

Trial ID	*SSR*	D_{AB} (m^2/s)	t_M (min)	t_S (min)
#1	31.1	9.055×10^{-9}	5.15	2.90
#2	32.1	9.210×10^{-9}	4.85	2.71
#3	32.1	9.132×10^{-9}	4.83	2.70
#4	32.1	9.132×10^{-9}	4.95	2.76
#5	32.2	9.450×10^{-9}	4.67	2.61
Average	31.9	9.196×10^{-9}	4.89	2.73
Std. Deviation	0.4	1.524×10^{-10}	0.18	0.11
± 95 %	0.4	1.336×10^{-10}	0.15	0.09
Using Raw Data Averages: Initial Mass Balance Error = +4.41% t_{CT} = 1.33 min (57.55% Diffusion) With Uncorrected D_{AB}: Initial Mass Balance Error = -16.12% t_{CT} = 1.94 min (57.55% Diffusion)				

Appendix J: Required Physical Property Data

Table J-1. Densities as **a** Function of Temperature for Water, **Air,** Carbon Dioxide, and Helium at 1 Atmosphere of Pressure

T (°C)	H_2O (l) [kg/m^3]	Air (g) [kg/m^3]	CO_2 (g) [kg/m^3]	He (g) [kg/m^3]
12.0	998.37	1.2382	1.8938	0.1710
12.5	998.32	1.2362	1.8905	0.1707
13.0	998.27	1.2342	1.8872	0.1704
13.5	998.22	1.2323	1.8839	0.1701
14.0	998.16	1.2303	1.8806	0.1698
14.5	998.11	1.2284	1.8773	0.1695
15.0	998.06	1.2264	1.8741	0.1692
15.5	998.01	1.2244	1.8708	0.1689
16.0	997.94	1.2225	1.8676	0.1686
16.5	997.87	1.2205	1.8644	0.1683
17.0	997.80	1.2186	1.8612	0.1680
17.5	997.73	1.2166	1.8580	0.1678
18.0	997.65	1.2146	1.8548	0.1675
18.5	997.58	1.2127	1.8516	0.1672
19.0	997.51	1.2107	1.8484	0.1669
19.5	997.44	1.2088	1.8453	0.1666
20.0	997.37	1.2068	1.8421	0.1663
20.5	997.29	1.2048	1.8390	0.1660
21.0	997.22	1.2029	1.8359	0.1658
21.5	997.15	1.2009	1.8327	0.1655
22.0	997.08	1.1989	1.8296	0.1652
22.5	997.01	1.1970	1.8265	0.1649
23.0	996.93	1.1950	1.8235	0.1646
23.5	996.86	1.1931	1.8204	0.1644
24.0	996.79	1.1911	1.8173	0.1641
24.5	996.72	1.1891	1.8143	0.1638
25.0	996.65	1.1872	1.8112	0.1635
25.5	996.57	1.1852	1.8082	0.1633
26.0	996.50	1.1833	1.8052	0.1630
26.5	996.43	1.1813	1.8022	0.1627
27.0	996.35	1.1793	1.7992	0.1624
27.5	996.28	1.1774	1.7962	0.1622
28.0	996.20	1.1754	1.7932	0.1619
28.5	996.12	1.1735	1.7902	0.1616
29.0	996.05	1.1715	1.7872	0.1614
29.5	995.97	1.1695	1.7843	0.1611
30.0	995.89	1.1676	1.7814	0.1608
30.5	995.82	1.1656	1.7784	0.1606
31.0	995.74	1.1637	1.7755	0.1603

T (°C)	H_2O (l) [kg/m^3]	Air (g) [kg/m^3]	CO_2 (g) [kg/m^3]	He (g) [kg/m^3]
31.5	995.66	1.1617	1.7726	0.1600
32.0	995.59	1.1597	1.7697	0.1598
32.5	995.51	1.1578	1.7668	0.1595
33.0	995.44	1.1558	1.7639	0.1593
33.5	995.36	1.1539	1.7610	0.1590
34.0	995.28	1.1519	1.7582	0.1587
34.5	995.21	1.1499	1.7553	0.1585
35.0	995.13	1.1480	1.7525	0.1582
35.5	995.05	1.1460	1.7496	0.1580
36.0	994.98	1.1441	1.7468	0.1577
36.5	994.90	1.1421	1.7440	0.1575
37.0	994.82	1.1401	1.7411	0.1572
37.5	994.75	1.1382	1.7383	0.1570
38.0	994.61	1.1363	1.7356	0.1567
38.5	994.38	1.1346	1.7328	0.1564
39.0	994.15	1.1329	1.7300	0.1562
39.5	993.92	1.1313	1.7272	0.1559
40.0	993.69	1.1296	1.7245	0.1557
40.5	993.46	1.1279	1.7217	0.1555
41.0	993.23	1.1262	1.7190	0.1552
41.5	993.00	1.1245	1.7162	0.1550
42.0	992.77	1.1228	1.7135	0.1547
42.5	992.54	1.1211	1.7108	0.1545
43.0	992.31	1.1194	1.7081	0.1542
43.5	992.08	1.1177	1.7054	0.1540
44.0	991.85	1.1160	1.7027	0.1537

Table J-2. Equilibrium Solubility Data for Air, Carbon Dioxide, and Helium in Water

T (°C)	Air in Water (kg/m^3)	CO_2 in Water (kg/m^3)	He in Water (kg/m^3)
12.0	0.02742	2.13641	0.001475
12.5	0.02710	2.09337	0.001467
13.0	0.02679	2.05104	0.001459
13.5	0.02648	2.00941	0.001452
14.0	0.02618	1.96848	0.001445
14.5	0.02588	1.92824	0.001438
15.0	0.02559	1.88870	0.001431
15.5	0.02530	1.84985	0.001424
16.0	0.02501	1.81168	0.001417
16.5	0.02473	1.77419	0.001410
17.0	0.02445	1.73739	0.001404
17.5	0.02417	1.70125	0.001397
18.0	0.02390	1.66579	0.001391
18.5	0.02364	1.63099	0.001385
19.0	0.02338	1.59686	0.001379
19.5	0.02312	1.56339	0.001373
20.0	0.02286	1.53058	0.001367
20.5	0.02261	1.49842	0.001361
21.0	0.02237	1.46691	0.001356
21.5	0.02212	1.43605	0.001350
22.0	0.02189	1.40584	0.001344
22.5	0.02165	1.37626	0.001339
23.0	0.02142	1.34732	0.001334
23.5	0.02119	1.31902	0.001329
24.0	0.02097	1.29135	0.001324
24.5	0.02075	1.26430	0.001319
25.0	0.02054	1.23788	0.001314
25.5	0.02032	1.21209	0.001309
26.0	0.02012	1.18691	0.001304
26.5	0.01991	1.16234	0.001299
27.0	0.01971	1.13839	0.001295
27.5	0.01952	1.11505	0.001290
28.0	0.01932	1.09231	0.001286
28.5	0.01913	1.07018	0.001282
29.0	0.01895	1.04865	0.001277
29.5	0.01877	1.02771	0.001273
30.0	0.01859	1.00737	0.001269
30.5	0.01841	0.98762	0.001265
31.0	0.01824	0.96846	0.001261
31.5	0.01808	0.94989	0.001257
32.0	0.01791	0.93190	0.001253
32.5	0.01775	0.91449	0.001249

Table J-2 (Continued).

T (°C)	Air in Water (kg/m^3)	CO_2 in Water (kg/m^3)	He in Water (kg/m^3)
33.0	0.01760	0.89765	0.001245
33.5	0.01744	0.88139	0.001242
34.0	0.01729	0.86570	0.001238
34.5	0.01715	0.85058	0.001234
35.0	0.01701	0.83602	0.001231
35.5	0.01687	0.82203	0.001227
36.0	0.01673	0.80860	0.001224
36.5	0.01660	0.79573	0.001220
37.0	0.01647	0.78341	0.001217
37.5	0.01635	0.77164	0.001213
38.0	0.01623	0.76042	0.001210
38.5	0.01611	0.74975	0.001207
39.0	0.01600	0.73963	0.001204
39.5	0.01589	0.73005	0.001200
40.0	0.01579	0.72100	0.001197
40.5	0.01569	0.71249	0.001194
41.0	0.01559	0.70452	0.001191
41.5	0.01549	0.69708	0.001188
42.0	0.01540	0.69016	0.001185
42.5	0.01531	0.68377	0.001182
43.0	0.01523	0.67791	0.001179
43.5	0.01512	0.67257	0.001176
44.0	0.01507	0.66775	0.001173

Table J-3. Diffusion Coefficient Data for Air, Carbon Dioxide, and Helium in Water With Temperature Correction based on the Wilke and Chang (1955) Model

T (°C)	μ_W (kg/m•s)	Air in Water (m^2/s)	CO_2 in Water (m^2/s)	He in Water (m^2/s)
12.0	1.282×10^{-3}	1.631×10^{-9}	1.345×10^{-9}	4.223×10^{-9}
12.5	1.261×10^{-3}	1.661×10^{-9}	1.370×10^{-9}	4.301×10^{-9}
13.0	1.240×10^{-3}	1.692×10^{-9}	1.395×10^{-9}	4.381×10^{-9}
13.5	1.219×10^{-3}	1.724×10^{-9}	1.422×10^{-9}	4.465×10^{-9}
14.0	1.198×10^{-3}	1.757×10^{-9}	1.449×10^{-9}	4.551×10^{-9}
14.5	1.177×10^{-3}	1.792×10^{-9}	1.478×10^{-9}	4.640×10^{-9}
15.0	1.156×10^{-3}	1.827×10^{-9}	1.507×10^{-9}	4.732×10^{-9}
15.5	1.135×10^{-3}	1.864×10^{-9}	1.538×10^{-9}	4.828×10^{-9}
16.0	1.121×10^{-3}	1.891×10^{-9}	1.560×10^{-9}	4.897×10^{-9}
16.5	1.109×10^{-3}	1.915×10^{-9}	1.579×10^{-9}	4.959×10^{-9}
17.0	1.097×10^{-3}	1.940×10^{-9}	1.600×10^{-9}	5.023×10^{-9}
17.5	1.085×10^{-3}	1.965×10^{-9}	1.621×10^{-9}	5.089×10^{-9}
18.0	1.072×10^{-3}	1.991×10^{-9}	1.642×10^{-9}	5.155×10^{-9}
18.5	1.060×10^{-3}	2.017×10^{-9}	1.664×10^{-9}	5.224×10^{-9}
19.0	1.048×10^{-3}	2.044×10^{-9}	1.686×10^{-9}	5.294×10^{-9}
19.5	1.036×10^{-3}	2.072×10^{-9}	1.709×10^{-9}	5.365×10^{-9}
20.0	1.024×10^{-3}	2.100×10^{-9}	1.732×10^{-9}	5.438×10^{-9}
20.5	1.011×10^{-3}	2.129×10^{-9}	1.756×10^{-9}	5.513×10^{-9}
21.0	9.992×10^{-4}	2.159×10^{-9}	1.780×10^{-9}	5.590×10^{-9}
21.5	9.870×10^{-4}	2.189×10^{-9}	1.805×10^{-9}	5.669×10^{-9}
22.0	9.748×10^{-4}	2.220×10^{-9}	1.831×10^{-9}	5.750×10^{-9}
22.5	9.625×10^{-4}	2.252×10^{-9}	1.858×10^{-9}	5.833×10^{-9}
23.0	9.503×10^{-4}	2.285×10^{-9}	1.885×10^{-9}	5.917×10^{-9}
23.5	9.381×10^{-4}	2.319×10^{-9}	1.912×10^{-9}	6.005×10^{-9}
24.0	9.259×10^{-4}	2.353×10^{-9}	1.941×10^{-9}	6.094×10^{-9}
24.5	9.137×10^{-4}	2.389×10^{-9}	1.970×10^{-9}	6.186×10^{-9}
25.0	9.015×10^{-4}	2.425×10^{-9}	2.000×10^{-9}	6.280×10^{-9}
25.5	8.893×10^{-4}	2.462×10^{-9}	2.031×10^{-9}	6.377×10^{-9}
26.0	8.771×10^{-4}	2.501×10^{-9}	2.063×10^{-9}	6.477×10^{-9}
26.5	8.649×10^{-4}	2.540×10^{-9}	2.095×10^{-9}	6.579×10^{-9}
27.0	8.552×10^{-4}	2.574×10^{-9}	2.123×10^{-9}	6.665×10^{-9}
27.5	8.472×10^{-3}	2.602×10^{-9}	2.146×10^{-9}	6.739×10^{-9}
28.0	8.392×10^{-4}	2.631×10^{-9}	2.170×10^{-9}	6.815×10^{-9}
28.5	8.311×10^{-4}	2.661×10^{-9}	2.195×10^{-9}	6.892×10^{-9}
29.0	8.231×10^{-4}	2.692×10^{-9}	2.220×10^{-9}	6.970×10^{-9}
29.5	8.151×10^{-4}	2.723×10^{-9}	2.245×10^{-9}	7.051×10^{-9}
30.0	8.071×10^{-4}	2.754×10^{-9}	2.272×10^{-9}	7.132×10^{-9}
30.5	7.991×10^{-4}	2.786×10^{-9}	2.298×10^{-9}	7.216×10^{-9}
31.0	7.911×10^{-4}	2.819×10^{-9}	2.325×10^{-9}	7.301×10^{-9}
31.5	7.830×10^{-4}	2.853×10^{-9}	2.353×10^{-9}	7.388×10^{-9}
32.0	7.750×10^{-4}	2.887×10^{-9}	2.381×10^{-9}	7.477×10^{-9}

T (°C)	μ_W (kg/m•s)	Air in Water (m^2/s)	C02 in Water (m^2/s)	He in Water (m^2/s)
32.5	7.670×10^{-4}	2.922×10^{-9}	2.410×10^{-9}	7.567×10^{-9}
33.0	7.590×10^{-4}	2.958×10^{-9}	2.439×10^{-9}	7.660×10^{-9}
33.5	7.510×10^{-4}	2.994×10^{-9}	2.469×10^{-9}	7.754×10^{-9}
34.0	7.429×10^{-4}	3.031×10^{-9}	2.500×10^{-9}	7.850×10^{-9}
34.5	7.349×10^{-4}	3.070×10^{-9}	2.532×10^{-9}	7.949×10^{-9}
35.0	7.269×10^{-4}	3.108×10^{-9}	2.564×10^{-9}	8.050×10^{-9}
35.5	7.189×10^{-4}	3.148×10^{-9}	2.596×10^{-9}	8.153×10^{-9}
36.0	7.109×10^{-4}	3.189×10^{-9}	2.630×10^{-9}	8.258×10^{-9}
36.5	7.029×10^{-4}	3.230×10^{-9}	2.664×10^{-9}	8.366×10^{-9}
37.0	6.948×10^{-4}	3.273×10^{-9}	2.699×10^{-9}	8.476×10^{-9}
37.5	6.868×10^{-4}	3.317×10^{-9}	2.735×10^{-9}	8.589×10^{-9}
38.0	6.802×10^{-4}	3.354×10^{-9}	2.766×10^{-9}	8.686×10^{-9}
38.5	6.757×10^{-4}	3.382×10^{-9}	2.789×10^{-9}	8.758×10^{-9}
39.0	6.712×10^{-4}	3.410×10^{-9}	2.812×10^{-9}	8.831×10^{-9}
39.5	6.667×10^{-4}	3.439×10^{-9}	2.836×10^{-9}	8.905×10^{-9}
40.0	6.622×10^{-4}	3.467×10^{-9}	2.860×10^{-9}	8.979×10^{-9}
40.5	6.577×10^{-4}	3.497×10^{-9}	2.884×10^{-9}	9.055×10^{-9}
41.0	6.532×10^{-4}	3.526×10^{-9}	2.908×10^{-9}	9.132×10^{-9}
41.5	6.487×10^{-4}	3.556×10^{-9}	2.933×10^{-9}	9.210×10^{-9}
42.0	6.442×10^{-4}	3.587×10^{-9}	2.958×10^{-9}	9.289×10^{-9}
42.5	6.397×10^{-4}	3.618×10^{-9}	2.984×10^{-9}	9.369×10^{-9}
43.0	6.352×10^{-4}	3.649×10^{-9}	3.010×10^{-9}	9.450×10^{-9}
43.5	6.307×10^{-4}	3.681×10^{-9}	3.036×10^{-9}	9.533×10^{-9}
44.0	6.262×10^{-4}	3.713×10^{-9}	3.063×10^{-9}	9.616×10^{-9}

Biography of the Author

David Robert Cyr was born in Caribou, Maine on February 19, 1971 to Irvin and Rachel Cyr. He was raised in Caribou and attended Caribou High School, graduating in 1989. He then attended The University of Maine and received a Bachelor of Science degree in Chemical Engineering in May of 1993. For the following two and a half years he was employed as an Applications Engineer and District Sales Representative for Nalco Chemical Company's Pulp and Paper Group in Northern Maine.

In January of 1996 he began graduate study in Chemical Engineering at his alma mater as a Teaching/Research Assistant. He earned a Master's degree in May of 1998 and continued in the program as a Ph.D. candidate. Upon completion of this degree, he plans to return to industry as a Research Scientist for SAPPI Fine Paper North America. David is a candidate for the Doctor of Philosophy degree in Chemical Engineering from The University of Maine in May, 2001.